Developments for studies of the extremes of nuclear matter

Gry M. Tveten

Thesis submitted in partial fulfilment
of the requirements for the degree of
philosophiae doctor

Department of Physics
Faculty of Mathematics and Natural Sciences
University of Oslo

May 2013

Series of dissertations submitted to the
Faculty of Mathematics and Natural Sciences, University of Oslo
No. 1375

ISSN 1501-7710

Cover: Inger Sandved Anfinsen.
Printed in Norway: AIT Oslo AS.

Produced in co-operation with Akademika Publishing.
The thesis is produced by Akademika Publishing merely in connection with the thesis defence. Kindly direct all inquiries regarding the thesis to the copyright holder or the unit which grants the doctorate.

Acknowledgments

I would like to express my deep gratitude to Professor Siem, my main supervisors, for her enthusiastic encouragement and guidance. I would also like to express my very great appreciation to Professor Siem for motivating me to apply for a PhD position in the first place. I would like to offer my special thanks to Joakim Cederkäll for providing me the possibility to work at ISOLDE, and for suggesting an interesting topic for my thesis. His willingness to give his time to supervise during my stay at CERN has been very much appreciated. Professor Guttormsen provided me with very valuable insight in experimental nuclear physics and understanding of the Oslo method.

I am deeply grateful to everyone in th ISOLDE physics grout at CERN for a warm welcoming and for readily sharing their experience with me. The environment at CERN opened up for many interesting discussions, and I will remember coffee at CERN as an inspiring ritual.

My gratitude goes towards the nuclear physics group at the Oslo Cyclotron Laboratory for creating a supportive and social working environment. It has been a pleasure to be a part of the SAFE center, both from an academic and a social point of view. I am most thankful to the excellent engineers of the Cyclotron Laboratory for their outstanding work keeping the cyclotron and the lab computers in good shape and for providing great experimental conditions during the campaigns.

Finally, I wish to thank my family and husband for their support and encouragement throughout my PhD.

Contents

Chapter 1

Introduction

The atomic nucleus is a unique mesoscopic quantum mechanical system, where the interaction of the nucleons still requires further investigation. Only a few, very light isotopes are well described by models derived from first principles. To model most isotopes one must depend upon calculations that are more or less phenomenological. Improving nuclear models is a collaborative effort that requires substantial experimental contributions. One important advance in experimental nuclear physics in later years has been the development of radioactive ion beams making experiments with nuclei not available in nature possible. Reaction studies with radioactive ion beams offer the possibility of testing nuclear models in new regions of the nuclear chart. An important application of our understanding of nuclear physics is to astrophysical questions, for instance how elements heavier than iron are synthesized in stellar environments. The measured solar abundances are not reproduced in calculations with todayś models and nuclear data inputs. Some important nuclear data inputs are level density, radiative strength function and deformation. The work in this dissertation is contributing to increased knowledge of nuclear properties of some important isotopes.

The ^{167,168,169}Ho isotopes are interesting because there has only been scarce experimental information available for the neutron-rich Ho-isotopes. The deformation of rare-earth isotopes in the mass region $160 \leq A \leq 180$ is believed to be of importance to the stellar abundance peak seen around $A \approx 160$. For very neutron-rich isotopes in this region, the theoretical deformation calculations deviate depending on the model of choice. It is interesting to investigate new means to derive the deformation of mid-shell nuclei. The results for ^{167,168,169}Ho using in-beam γ-ray spectroscopy following a deep inelastic multi-nucleon transfer reactions from ^{82}Se beam on ^{170}Er target, carried out at Laboratori Nationali di Legnaro (LNL) in Padova, Italy, are presented.

The density of energy levels increases rapidly with excitation energy, and

it becomes challenging to discern energy levels experimentally. Atomic nuclei excited into the quasi-continuum region are appropriately described by statistical concepts. The nuclear physics group at the Oslo Cyclotron Laboratory (OCL) has developed a method to extract level density and radiative strength function from first-generation γ-ray spectra for excitation energies between the ground state and the neutron (proton) binding energy. The level density and radiative strength function are significant inputs to nuclear reaction rate calculations. Moreover, the level density of atomic nuclei provides insight into the disorder of the nucleus as a quantum mechanical system and the radiative strength function is instrumental in understanding collective resonances. The radiative strength function and level density of the isotope ^{44}Ti, which is important for astrophysical reaction rate calculations, has been extracted and discussed. An enhancement of the radiative strength function, compared to experimental expectations, has been observed for isotopes ranging from ^{56}Fe to ^{98}Mo. This enhancement has not been observed for the Sn-isotopes. To gain an increased understanding of this enhancement it is interesting to investigate the radiative strength functions of Cd-isotopes in the mass region between the Mo-isotopes and the Sn-isotopes. New, unexpected results for the radiative strength functions of the Cd-isotopes are presented.

Exploring unstable isotopes or nuclei at high excitation energies requires development in instrumentation and separator technique. A spectrometer for the study of transfer reactions at the upgrade of the radioactive ion-beam facility at CERN, HIE-ISOLDE [1], has been proposed. A large portion of the work for this dissertation has been focused on simulations and calculations to explore the scientific possibilities and limitations that arise from the choice of a particular ion-optical[1] design for such a device.

The structure of the dissertation is organized as follows: Chapter 2 gives an overview of the physics cases that are important for this work and the relevant theory. Chapter 3 gives a general overview of relevant spectrometer technology and the tools used in this work to simulate ion-optical performances. Chapter 4 addresses the experimental setup and data analysis of the experiment from LNL, as well as the experimental results. Chapter 5 presents and discusses the experimental results for the Ti- and Cd-experiments at OCL. Chapter 6 presents the simulations performed for spectrometers with realistic beam parameters for HIE-ISOLDE. The papers included in the dissertation are presented and discussed in chapter 7. The results are discussed and the future outlook is given, and finally the conclusions are presented in chapter 8.

[1] Ion-optics involves the focusing of plasma and ion streams.

Chapter 2

Nuclear structure and reactions

Through groundbreaking experiments the behaviour of the atomic nucleus has been gradually uncovered. Atomic nuclei will exhibit both features best described as single particle and collective states. It was eventually realized that the protons and neutrons are held together by an effective nuclear force originating from the strong force within the nucleons. An outstanding theoretical effort resulted in a good understanding of the most important features of nuclear structure. Although atomic nuclear matter has been intensively studied the last fifty years, our theoretical understanding of nuclear matter is still far from flawless. There is no a priori theory that fully describes all aspects of nuclear properties simultaneously, and the quality of theoretical calculations tends to decline with the increasing excitation energy of nuclei. Calculations from first principles are limited to ≈ 12 nucleons using Monte Carlo Techniques [2] and cases where scattering is also considered to ≈ 5. One of the reasons for this is that the strong force is not well enough understood and non-perturbative in the case of low energy processes such as nuclear reactions and the many-body quantum mechanical problem is too involved to be solved exactly for most cases. Consequently, large variety of nuclear models exists, each fine tuned to certain mass regions or certain aspects of the nuclear structure. For these reasons, experimental work is still essential to nuclear physics. In the optimistic spirit of reductionism [3] nuclei are described as a many-body wave function of its constituent nucleons. From this point of view further experimental knowledge of unstable isotopes is an important benchmark for testing basic assumptions in theoretical calculations. Increased experimental knowledge also improves the possibilities for improving semi-empirical models.

2.1 Nuclear structure

Models of nuclear structure have developed from two main approaches to understanding and modeling atomic nuclei. In the macroscopic approach atomic nuclei are described by bulk properties such as shape, radius and density and are inspired by the liquid-drop model [4]. In the microscopic approach one considers atomic nuclei as collections of nucleons and describe nuclei using many-body wave functions and their properties. This type of model describes nuclear properties by wave-functions of single particles considered more or less as independent particles. The difference between the two approaches is illustrated by figure 2.1.

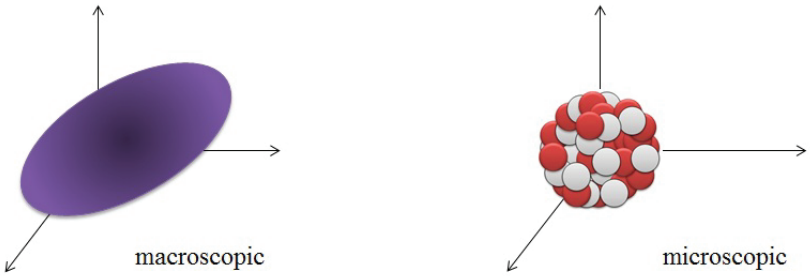

Figure 2.1: Macroscopic vs Microscopic descriptions of atomic nuclei.

2.1.1 Open shell nuclei and collective models

The excited states that exist below the excitation energy needed to break a neutron or proton pair in even-even nuclei should be mainly collective by nature. This assumption has been supported by the reduced transition probabilities for the excitation of such states being many times higher than expected for single particle states. Most isotopes will exhibit ground state deformation. However, a certain number of nuclei have been shown to exhibit evidence of coexisting different shapes at similar excitation energies. It is currently believed that shape coexistence might occur in all nuclei except for in the lightest [5].

2.1.2 Closed shell nuclei and microscopic models

As discussed not only the energy of assumed single particle energy levels in nuclei are important to shell model calculations, but one would also want to know to what extent observed energy levels are pure single states and how they are best

described quantum mechanically. The spectroscopic factors give a measure of how well energy levels are described by theory, and thus also information on to what extent they can be considered single particle states. Recently, new methods to determine spectroscopic factors from direct reactions have been developed, as for example the work discussed in reference [6]. The importance of the choice of optical model parameters to the extraction of spectroscopic factors and why it is probably important to use a set of elastic scattering data at different beam energies are discussed in reference [7].

2.1.3 The quasi-continuum region and statistical properties

The discrete energy region of the nucleus is where nuclear states have well-defined quantum numbers, while the continuum energy region is where the level spacing becomes smaller than the inherent width of the states. As the excitation energy of the nucleus increases beyond the discrete region, the number of levels increases exponentially. As the level spacing decreases, the mixing that occurs due to small, residual interactions dilutes the quantum mechanical purity of states. The nucleus in the quasi-continuum region is therefore well described by statistical properties.

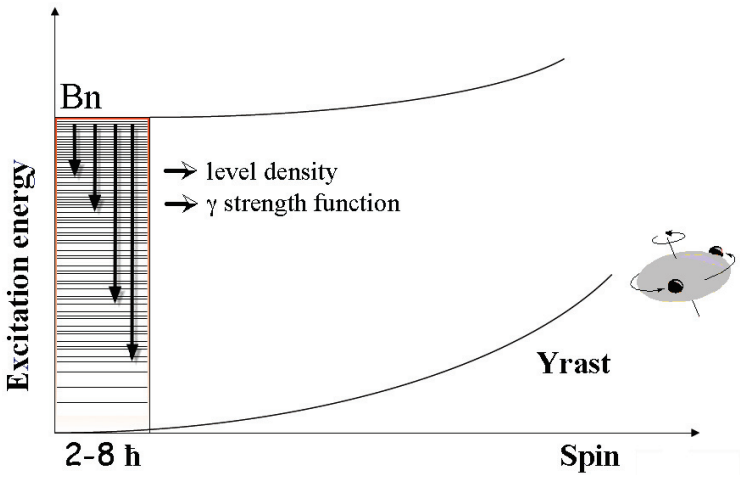

Figure 2.2: Excitation energy-spin diagram illustrating the quasi-continuum region that has been studied with the Oslo method in this thesis.

The level density is defined as the number of quantum energy levels accessible at a specific excitation energy, within a given energy bin. The radiative strength

functions provides information on the probability for transitions between different excitation energies, thereby describing the average electromagnetic properties of excited nuclei.The level density and gamma strength functions are important properties of the nucleus, that are needed to describe decay by γ-rays in the quasi-continuum region. In this thesis warm nuclei at low spin have been investigated, see the region of interest in the Energy-Spin diagram of figure 2.2.

For a range of applications the knowledge of the average properties of isotopes, such as the level density and γ strength functions, are important. One example is Hauser-Feshbach calculations of nuclear reaction cross-sections needed to model how elements are formed in stellar environment [8]. Statistical properties of nuclei reveal details of nuclear structure that are hard to access by studies of discrete levels, such as thermodynamical properties. The statistical properties of ^{44}Ti and ^{105,106,111,112}Cd are discussed in chapter 5.

2.2 Experimental probes for studying the properties of atomic nuclei

Learning about the inner structure of atomic nuclei requires reactions with probes that can access the nucleus. To study the nuclear properties of isotopes one may chose from a variety of available techniques and reactions the method best suited for the studies of interest. Different reactions can give information on different aspects of atomic nuclei. This chapter will present a short overview of the reactions that are relevant for the simulations or the experimental work of this dissertation.

2.2.1 Coulomb excitation

In coulomb excitation experiments a heavy ion beam typically impinges on a heavy ion target, at beam energies below the threshold for reactions involving the strong force. Excitation is caused by the time-dependent electromagnetic field between the target and beam nuclei. When γ-ray spectroscopy is combined with particle identification of the scattered particles from Coulomb excitation experiments, transition probabilities can be found. Reduced transition rates for the transitions from the first $2^+ \rightarrow 0^+$ ($B(E2)_{20}$) and $4^+ \rightarrow 2^+$ ($B(E2)_{42}$)) in even-even nuclei are sensitive to the deformation as well as the degree of the collectivity of the isotope [9]. Figure 2.3 gives an overview of the isotopes where reduced transition probabilities are experimentally studied. This type of reaction is well suited for studying the collective properties of atomic nuclei. In the case that sufficient beam energy is provided one may reach higher excitation energies

through multi-step excitation.

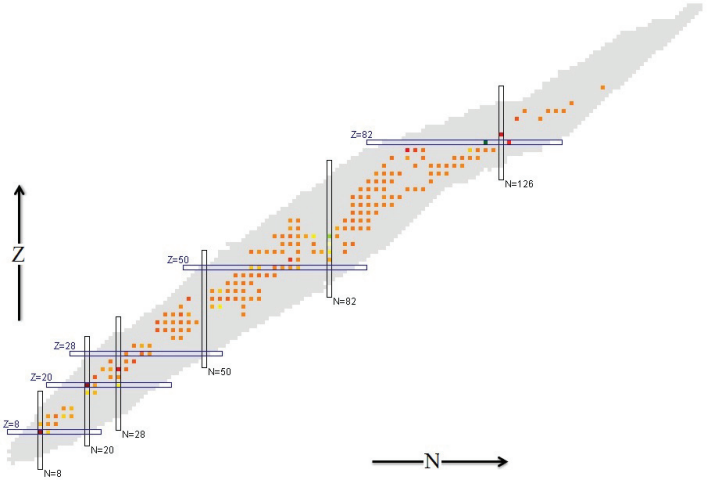

Figure 2.3: An overview of the current knowledge of the ratios of the transition probabilities $\frac{B(E2)_{42}}{B(E2)_{20}}$ [10].

2.2.2 Direct transfer reactions

Transfer reactions are nuclear reactions where one or more nucleons are transferred between the nuclei involved. Nucleon transfer reaction is an important source of information on nuclear structure. Single-nucleon pickup and stripping information are of great importance as they provide information on the occupational probabilities of single-nucleon states. Pickup reaction probe hole states in the nucleus of interest while the knock out and stripping reaction gives information on particle states. Data from such reactions are simplest to interpret in cases where the target nucleus has spin zero and when the reaction to high accuracy can be considered to happen in one step. This happens when the interaction between the projectile and target nucleus is weak [9].

The beam energies that are going to be available at HIE-ISOLDE make a large variety of reactions above the coulomb barrier accessible. One would typically have a light particle, such as deuteron, transferring a neutron or proton to a heavier nucleus. In such single nucleon transfer the Q-value (energetic balance) of the reaction gives information on the position of the states, the angular distribution is related to the spin and parity of the state and the total cross section gives a

measure of the overlap of the structures of the original and recoil nucleus. Using two nucleon transfer reactions can reveal the paring properties of nucleons.

In single particle transfer reactions a radioactive beam will impinge on e.g. a target containing deuteron. The transfer of a neutron or proton to the ions of the beam will result in the heavy products being forward focused. Typically there is a considerable overlap of the beam ions and recoils of interest. For this type of reaction a recoil separator must be placed at 0°.

2.2.3 Fusion-evaporation reactions

In cases where one is interested in learning about excited states of nuclei one would often opt for studying nuclei through reactions. In fusion-evaporation reactions two nuclei fuse and evaporate neutrons and γ-rays. Fusion-evaporation reactions is another class of reactions that results in forward focused recoils although the distribution is isotropic in the center of mass. As the cross sections often are lower than for direct transfer, this type of reaction requires quite high beam intensities in the context of RIB, but might be achievable in the future at HIE-ISOLDE. This type of reaction is well suited to produce proton-rich nuclei with high excitation energy and large angular momentums. Nuclear super-deformation has been studied in fusion-evaporation experiments and this reaction type is also well suited for building completing level schemes.

2.2.4 Deep inelastic reactions

In deep inelastic transfer reactions a fixed target of a heavy element is also used. The cross section for few particle transfer is peaked close to the grazing angle of the reaction and varies depending on the chosen beam and target. At large angles the production of low energy products is favored. To be able to chose the channels of interest in deep inelastic reactions it is thus necessary to rotate the recoil spectrometer to the angle of interest [11]. In deep inelastic reactions one or several nucleons may be transferred between the beam and target. The energies are such that also nucleons deep within the nuclei are involved in the reaction, hence the name. As for fusion-evaporation one may attain relatively high excitation energies and angular momenta, however the cross section for neutron evaporation is lower, thus the reaction mode may be well suited for studying neutron-rich nuclei. The maximum cross section for deep inelastic transfer reactions occurs at the grazing angle given by

$$\theta_{gr}(lab) = \frac{2.88 Z_t Z_p [931.5 + (T_{lab}/A_p)]}{A_p[(T_{lab}/A_p)^2 + 1863(T_{lab}/A_p)]} \times \frac{1}{R_{int}}[rad] \tag{2.1}$$

where T_{lab} is the projectile energy in laboratory coordinates in MeV, Z_t the atomic charge of the target nucleus, Z_p the atomic charge of the projectile nucleus, A_p is the mass of the projectile nucleus in atomic units and R_{int} is the interaction radius that can be calculated by the equations given in Ref. [12]

$$R_{int} = C_1 + C_2 + 4.49 - \frac{C_1 + C_2}{6.35}[fm] \tag{2.2}$$

where C_i is given by $C_i = R_i(1 - R_i{}^{-2})$[fm] and $R_i = 1.28A_i{}^{1/3} - 0.76 + 0.8A_i{}^{-1/3}$ [fm].

2.3 Radioactive ion beam facilities

Accelerated beams has since the work of Cockcroft and Walton [13] been a much used tool to study nuclei. The reactions mentioned above all require an accelerated beam. One way to further expand our current knowledge is by doing experiments with radioactive ion beams. Experimental information on radioactive isotopes is an important benchmark for testing nuclear models.

As illustrated by the Segre chart shown in figure 2.4 a large number of isotopes remain undiscovered. Theoretical calculations estimate that about 30% of all possible isotopes have been produced and studied in laboratories, making studies of the remaining 70% an interesting challenge for experimentalists.

Today, several dedicated radioactive ion beam (RIB) facilities have been in operation for years. Currently, upgrades are carried out to facilitate beams with even shorter lived nuclei and with higher beam energies and new facilities are being constructed (e.g. FRIB at Michigan State University). There are two main production methods used in RIB production. One method is to have a primary beam produce a cocktail of radioactive isotopes by impinging on a thin target and further select the isotope of interest by separators in-flight. The in-flight method works satisfactorily for proton-rich nuclei as neutrons tend to be knocked out in the reactions at the primary target. Furthermore even very short lived isotopes can be produced and studied using this production method. Examples of RIB facilities where the in-flight method is used is RIPS at RIKEN [14] and the FRS facility at GSI [15]. The other method of production is the Isotope Separation On-Line (ISOL) method [16]. The ISOL technique was invented at the Niels Bohr Institute in 1951 by Otto Kofoed-Hansen and Karl Ove Nielsen who had the idea of coupling a Uranium target to the ion source of an electromagnetic recoil separator [17]. The principles of the ISOL-method is shown in figure 2.5. The ISOL technique has the benefit of rather pure beams with well defined beam emittance. The main drawback of the method is that the ISOL technique has many stages that are rather time consuming, in this context, the variety of beams

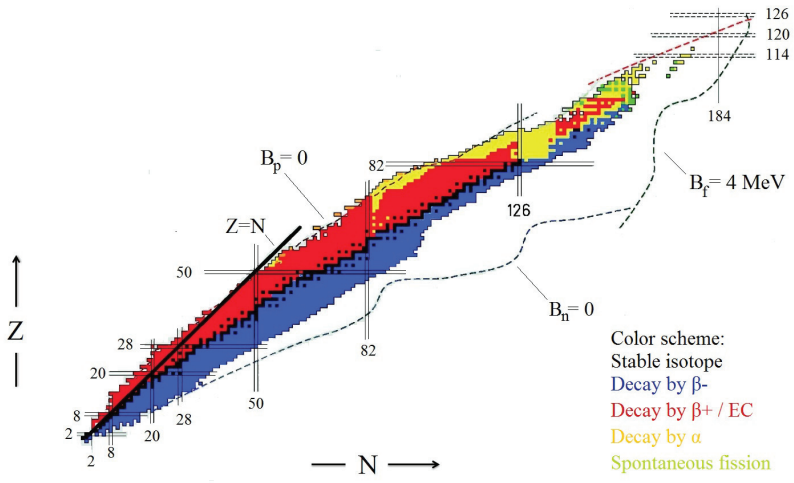

Figure 2.4: Within the borderlines defined by the proton, B_p, and neutron, B_n, drip-lines and the fission barrier B_f it is believed that 6000 nuclei can be formed of which the stable nuclei are the best studied (black squares). Unstable isotopes that have been observed are shown in colors depending on the mode of decay. It is clear that the majority of the unobserved isotopes lie on the neutron rich side of the valley of stability. Also given on the figure as vertical (horizontal) lines are the magic numbers for neutrons(protons) as established for stable isotopes.

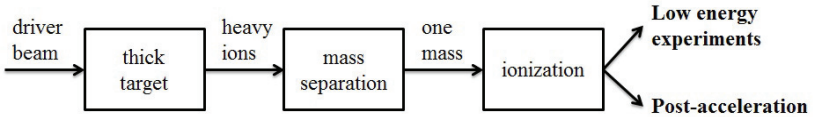

Figure 2.5: A schematic presentation of the principles of the ISOL technique.

available is limited to life times above a few ms of the isotopes of interest. Furthermore, only elements with chemical properties allowing diffusion out of the primary targets can be produced. Examples of ISOL facilities are SPIRAL at GANIL in Caen, France and ISOLDE at CERN. The RIB facility ISOLDE has been in operation at CERN since 1967 and is the longest serving experimental facility at CERN [18]. The present ISOLDE facility has been in operation since 1992 [19, 20, 21] and has been expanded several times. In the early history of

ISOLDE mass measurements was the dominating experimental activity. Over the history of ISOLDE more than 800 radioactive isotopes have been successfully produced and delivered for experiments. An overview of the elements that RIBs have been delivered for is shown in figure 2.6.

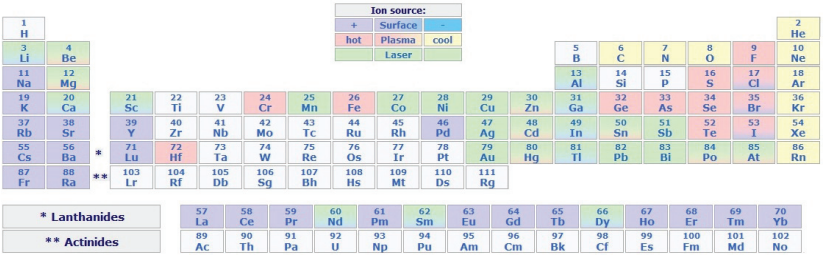

Figure 2.6: The elements that have been delivered as beams at ISOLDE so far are shown in colors, figure adopted from ref. [22].

The latest addition was REX-ISOLDE, a post accelerator for the secondary radioactive beams [23, 24], made spectroscopy experiments requiring higher energy a possibility. Currently beam energies of $\approx$ 3 MeV/u is available at ISOLDE [25]. The accelerated beams available at ISOLDE in combination with the γ-ray spectrometer MINIBALL [26, 27] has proven to be particularly well suited for coulomb excitation experiments [28].

2.4 HIE-ISOLDE

The ongoing High Intensity and Energy (HIE) upgrade of ISOLDE (HIE-ISOLDE) [1] aims at substantially increasing the energy range, the intensity and the quality of the secondary radioactive beams produced at the ISOLDE facility [29]. The planned layout of the experimental area of HIE-ISOLDE is shown in figure 2.7. The aim of the upgrade is to provide experimenters with smaller beam emittance, higher energy of the post-accelerated beam and higher intensities. In order to achieve higher energies for the post-accelerated secondary beam an upgrade of REX-ISOLDE is being commissioned.

The energy upgrade will take place in stages. When the upgrade is finalized, the existing linac will be replaced by a superconducting linac. When the final stage of the upgrade is completed, post-accelerated radioactive beams with kinetic energy of $\approx$ 10 MeV/u will be a possibility, but already in 2015 beams of $\approx$ 6 MeV/u will be available. This will open the door to nuclear reaction studies and expanding the available scientific program compared to the

existing REX-ISOLDE. This, in combination with better quality of the beam and higher intensities will open the door to examining several scientific questions of fundamental interest [30]. For many physics cases one is interested in reactions where one or a few nucleons are transferred to the beam. In inverse kinematics, few-nucleon transfer results in the reaction products (recoils) being forward focused. In deep inelastic transfer reactions, where one or several nucleons are transferred from a heavy target to the beam or vice versa, the preferred angle is often close the grazing angle and the angular spread of the products is large. In these cases a recoil separator is often well suited or even needed to tell recoils and beam apart, to select the exit channel and to do spectroscopic studies. When the HIE-ISOLDE energy upgrade is completed, multi-step Coulomb excitation will also be feasible. For several physics cases a spectrometer may be useful for event tagging.

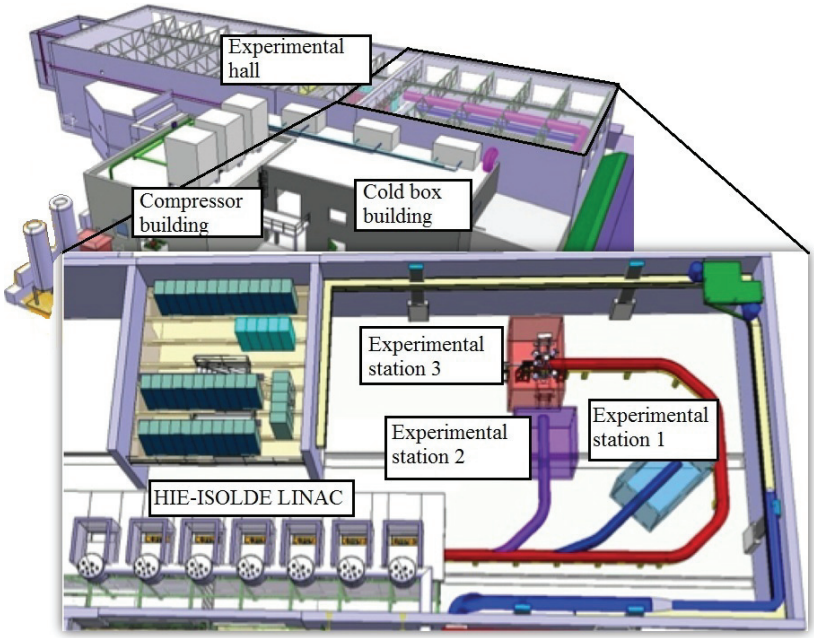

Figure 2.7: A view of the current layout of the ISOLDE facility at CERN. The enlarged portion of the figure shows the area of the experimental hall where the superconducting linac is situated and a possible arrangement of the new experimental stations.

As mentioned, more than 800 different radioactive isotopes have been

produced at ISOLDE. Ions as light as ^{8}Li and as heavy as ^{224}Ra [31] have been successfully accelerated. An even larger diversity of beams is expected to be available at HIE-ISOLDE. Given the many experimental possibilities it is interesting to see what different types of spectrometers and separators can achieve. The simulations and calculations carried out for a future spectrometer for secondary reactions at HIE-ISOLDE are presented in chapter 6.

Chapter 3

Mass spectrometers and ion-optics

In this chapter the essential theory behind the ion-optical calculations and simulations described in chapter 6 and Paper 4 is described and discussed here.

3.1 Spectrometers and recoil separators

The term mass spectrometer would be used to describe any device capable of producing spectra that enables the experimenter to tell apart reaction products with different masses. A recoil separator is a device that physically separates the reaction products (recoils) from the unreacted beam components [32]. Traditionally in nuclear physics, the separation of recoils from beam has been achieved by dispersing the particles according to their mass-to-charge ratio (A/q) using a combination of electrostatic and magnetic elements. In this case the particles are detected at the focal plane using position sensitive detectors. The position information gives the A/q of the detected particle. Mass identification must rely on a pure beam or be carried out using auxiliary detectors.

In particle physics, particle tracking has been an essential tool in the experimental tool box for decades. Recently, ray-tracing spectrometers have also been designed for nuclear reaction studies. This type of spectrometer relies on tracking detectors and off-line reconstruction of ion characteristics to identify the transported products. In principle, any spectrometer or recoil separator could be improved by tracking to correct for aberrations or to identify the products. In nuclear physics, so far, magnetic spectrometers have been used in combination with tracking. Ray-tracing results in a more intricate off-line data analysis, but facilitates higher order aberration corrections than is possible by hardware alone [33, 34]. As aberrations are corrected for in analysis, ray-tracing devices allow large acceptances. Measuring the momentum of ions can also be achieved using a large acceptance magnetic spectrometer.

3.2 Ion-optics and transfer maps

When we speak of an ion beam we usually refer to either a continuous or bunched collection of ions with motion somehow bounded within a suitable volume of phase-space. Ion-optics is the field of focusing beams and plasma-streams. Mostly dipole and quadrupole electromagnetic fields play a similar role to glass lenses in optics. In addition higher order fields are applied for correction purposes. The trajectory of charged particles through ion-optical elements depends on the particle's rigidity against electromagnetic deflection as well as the field distribution of the ion-optical elements. The most straight forward way to decide the motion of charged particles through ion-optical elements would be by computing their path by solving the equations of motion for the electromagnetic fields of the elements. This type of calculations are computationally demanding, especially for more complicated ion-optical elements. Therefore it is commonplace to use transfer matrices for the principle design and analysis of ion-optical systems, including spectrometers and recoil separators. Calculations should still always be compared to a full electromagnetic model with realistic field simulations before an instrument is ordered.

3.2.1 Emittance and Liouville's theorem

The concepts of statistical physics are commonly applied to beam physics, as the interactions among the ions of the beam bunches often can be neglected. Beam emittance is a statistical concept used to describe the spread of the coordinates of particles in the position-momentum phase-space occupied by a beam bunch. Liouville's theorem applies in any system that can be described by matrixes with trace $= 0$, such as conservative Hamiltonian systems [35]. Electrically charged particles moving in static magnetic and or electric fields are examples of such systems where the equation is valid. Liouville's equation describes the time evolution of a phase-space distribution:

$$\frac{d\rho}{dt} = \frac{\delta\rho}{\delta t} + \sum_{i=1}^{n}\left(\frac{\delta\rho}{\delta q_i}\dot{q}_i + \frac{\delta\rho}{\delta p_i}\dot{p}_i\right) = 0, \tag{3.1}$$

where q_i are the canonical coordinates and p_i the conjugate momenta. In the case of the six-dimensional phase-space of the beam bunch the equation is called the Liouville's theorem. If the motion in each Cartesian plane is decoupled from that in the other planes, then the emittance remains constant. One may define the phase-space density of many non-interacting particles by considering systems, each of which has slightly different initial conditions. The theorem states that phase-space density of the beam bunch is preserved as one follows the motion of

the particles. The theorem is valid for any assembly of particles where the particle density allows the assembly to be described as an assembly of non-interacting particles. For the specific cases considered in Chapters 4 and 6 this is reasonable assumption, as the beam intensities is too low for interaction between the beam particles to take place. Different definitions of emittance are in use, as discussed in appendix A.

Emittance is reduced when a beam is accelerated. This is the reason why the emittance of a machine usually is quoted as normalized emittance (ε_n). The user may then calculate the expected emittance at any given energy. The resulting emittance is often referred to as geometric emittance. The geometric root mean square emittance, ε_{rms}, is given as

$$\varepsilon_{rms} = pq = \sqrt{\langle x^2 \rangle \langle x'^2 \rangle - \langle xx' \rangle^2}, \tag{3.2}$$

where x is the deviation of the particles from the optical axis and x' is the inclination of the path of the particle in the x-z-plane.

3.2.2 Transfer maps

The development of the optical coordinates $\mathbf{r}$ of the ion-optical system is given by the differential equation $\mathbf{r}' = \mathfrak{f}(\mathbf{r}, s)$, where s is an independent variable usually chosen as the path along the reference trajectory and the function $\mathfrak{f}$ is found by the Cartesian equations of motion through the electromagnetic fields [36]. The details of the function $\mathfrak{f}$ is given in chapters 3, 4 and 7 of reference [37]. The final coordinates, $\mathbf{r}_f$ are given by the map $\mathscr{M}$ mapping the initial coordinates $\mathbf{r}_i$ at s_i to the final coordinates $\mathbf{r}_f$ at s_f as in equation 3.3.

$$\mathbf{r}_f = \mathscr{M}(\mathbf{r}_i, s_i, s_f) \tag{3.3}$$

This allows the final coordinates, $\mathbf{X}_f$, of particles to be decided as a function of their initial coordinates, $\mathbf{X}_i$ as in equation 3.4

$$\mathbf{X}_f = \mathscr{M}\mathbf{X}_i \tag{3.4}$$

The $\mathbf{Y}$ coordinates are correspondingly treated. The position vectors $\mathbf{X}$ and $\mathbf{Y}$ must correspond to the order of M. For example second order calculations where the energy and position deviates from the central particle at s_i requires the coordinates given in equation 3.5 and 3.6

$$\mathbf{X}_i = \{x_i, a_i, t_i, \delta_i, x_i a_i, a_i^2, y_i^2, y_i b_i, b_i^2, x_i \delta_i, a_i \delta_i, \delta_i^2\}, \tag{3.5}$$

$$\mathbf{Y}_i = \{y_i, b_i, y_i x_i, b_i x_i, y_i a_i, b_i a_i, y_i \delta_i, b_i \delta_i\} \tag{3.6}$$

revealing that even for second order calculations the position of particles at the exit of an ion-optical system can depend upon many factors, thus making the calculation of image aberrations complicated for systems where higher order calculations must be carried out.

Only for a few, simple systems may the above equations of transport be solved exactly. Usually one must find approximate solutions and often the dependence of $\mathbf{r}_f$ on s is expanded in Taylor series using propagator of the dynamical system $\mathbf{r}_f = exp(\Delta s \cdot L_f)\mathbf{r}_i$ where L_f is the directional derivative $L_f = \dot{\mathbf{r}} \cdot \nabla \delta_s$. The transfer map's accuracy then depends on the nature of the system and the number of expansion terms calculated.

3.2.3 Ion optical codes

Ion-optical codes can be divided into two families; codes that calculate the trajectories in electro-magnetic fields and codes that calculate the transfer matrix of an ion optical system for given fields. Simion and Comsol are examples of commercial software operating by the first mentioned principle. On the other hand, GIOS and COSY infinity [38, 39, 40] are examples of transfer matrix based codes. Calculating the trajectories by solving the equations of motion for detailed field calculations give the most accurate results. However, setting up and configuring such calculations are time consuming and must be redone for every time one wants to change the geometry or such of the ion optical system in question. Furthermore, the simulations tend to be computationally challenging in the sense that each ion being traced takes much processor time and memory. The transfer map approach is well suited for simulations that require a high number of simulated events or calculations where one wants to experiment with several different ion optical layouts.

COSY infinity employs differential algebraic approach to ion beam optics [41]. This approach allows transfer matrices to be calculated up to arbitrary order, only limited by the available computer capacity [42]. COSY infinity has been selected for the simulations presented in chapter 6. Calculations in COSY infinity is performed with scaled coordinates, as shown in figure 3.1.

3.2.4 Sources of image aberrations

Geometric aberrations are an inherent property of any ion-optical system and relates to the positional and angular extension of the beam entering the system. These aberrations cannot be corrected using higher order fields. Chromatic aberrations are observed when one studies the trajectories of particles with kinetic energy that deviates from the energy of the particle moving along the central path, in other words when $\delta_K \neq 0$ [37]. For experiments where a RIB induces

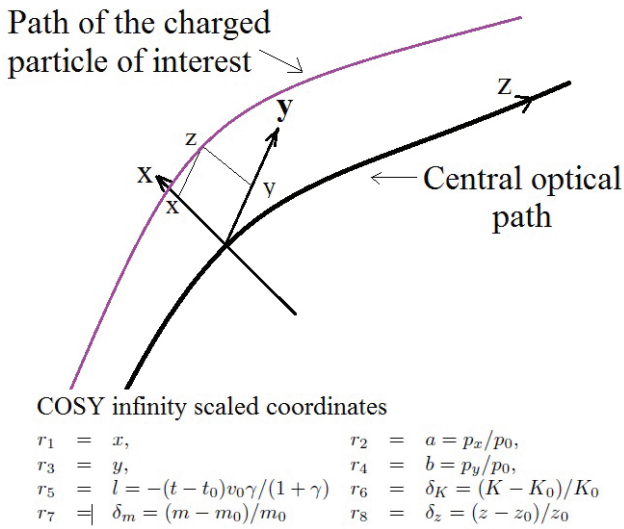

Figure 3.1: The scaled coordinates used in COSY infinity for all calculation.

the reaction, it is of great importance to be able to utilize as much of the available beam as possible, also when that results in relatively large beam spot sizes at the target. For this reason, aberrations that depend upon the product of geometric quantities and energy deviation, for instance, are crucial to the overall performance of spectrometers and recoil separators for RIB experiments.

Higher order elements such as sextupoles can remove lower order aberrations such as third order, but they will introduce higher order aberrations. With the advance of fast and position sensitive detectors, reconstruction correction [43] is achievable.

3.3 Separator and spectrometer design

When considering different separator or spectrometer designs different criteria can be considered depending upon the purpose of the device [37]. For an angle and energy focusing device, also called recoil separator, the design requirement is that the dispersion due to angular and energy spread is negligible or written with transfer matrix elements:

$$(x|a) = (x|\delta_K) = 0. \tag{3.7}$$

where $(x|a)$ is the angular dispersion and $(x|\delta_K)$ the energy dispersion. This implies that higher order elements that may contribute to the angular or energy dispersion must be kept small by the design of the system [32].

The smallest rigidity difference that can be solved, Δ_{min}, is given by

$$R_\Delta = -\frac{1}{\Delta_{min}} = -\frac{(x|\Delta)}{(x|x)2x_{10}}, \tag{3.8}$$

where x_{10} is the maximum deviation in the x-direction of the beam, $(x|x)$ is the image, $(x|\Delta)$ is the dispersion due to the rigidity Δ. For the physics cases considered in this dissertation rigidity resolving power is often an important criteria. The dispersion of interest is sought maximized by the ion-optical design. The FWHM resolution is also commonly given.

When studying reactions with low cross sections or when using radioactive ion beams the acceptance and transmission of a spectrometer or recoil separator is of particular importance. A device is also described by its angular and energy acceptance.

3.4 Spectrometers

In the case of recoil separators the x-position at the focal plane is expressed in the case of first order calculations as

$$x = (x|x)x_0 + (x|a)a + (x|\delta_K)\delta_K + (x|\delta_M)\delta_M \tag{3.9}$$

where x_0 is the relative x-deviation of the ion at the target, δ_K the relative energy deviation and δ_M the relative mass deviation. To obtain mass focus one must design the recoil separator to have $(x|\delta_E) = (x|a)a = 0$, thus providing angular and energy focus. The Fragment Mass Analyzer (FMA) at Argonne National Laboratory [44] is an angle and energy focusing recoil separator. FMA has inspired the design of several similar machines including EMMA under construction at TRIUMF [45]. Due to the symmetric design shown in figure 3.2, the energy dispersion is canceled, and as the quadrupoles provide angular focus, the only remaining dispersion at the focal plane is due to the A/q-ratio. This type of separator is often referred to as a recoil separator. In this case ion-optical aberrations must be corrected with hardware and thus there is a practical limit to the maximum achievable acceptance as the geometrical aberrations grow with the deviation of the rays from the optical axis.

There is also the option of combining a momentum separator with a traditional A/q separator. This is done, for example, at the Holifield Radioactive Ion Beam facility. The Recoil Mass Spectrometer (RMS) consists of two separation stages.

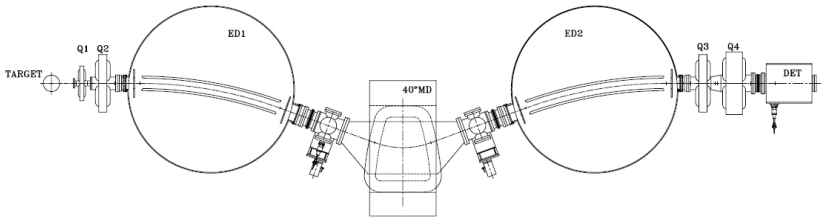

Figure 3.2: A schematic overview of EMMA taken from ref. [45].

The first part disperses products according to their momentum and the second stage according to A/q. This gives the possibility of physically blocking the beam in the first separation stage even in cases where the beam and recoils of interest have similar kinematic characteristics. The focal plane after the momentum separator alone can be used if mass identification is not needed. Otherwise one must make use of the whole 25 meter long separator in order to have mass identification [46, 47].

A new vacuum-mode recoil separator MARA at JYFL [48] is being constructed and commissioned at JYFL. It will be constructed out of a quadrupole triplet, an electrostatic dipole and a magnetic dipole. The device has been designed to have $\approx \frac{1}{250}$ resolving power and 10 msr angular acceptance, assuming a beam spot sized $\pm 1.0 \times \pm 1.5$ mm^2. MARA is currently under construction.

As mentioned earlier, ray-tracing spectrometers offer the possibility of correcting aberrations in the off-line analysis and thus improving the overall resolution of the device. Examples of this type of separator are VAMOS at GANIL [49] and PRISMA at LNL [50].

Chapter 4

Deep inelastic transfer reactions studied with PRISMA+CLARA at LNL

In this thesis the neutron-rich ^{167,168,169}Ho isotopes have been investigated. The motivation was two-fold. First, and most importantly, the deformation of rare-earth nuclei is believed to be important to understanding the stellar abundance peak seen at $A \simeq 160$. Therefore, it is interesting to investigate new methods to derive information on deformation for unstable rare-earth isotopes. Only scarce experimental information for ^{167,169}Ho existed prior to this work. Secondly, PRISMA represents one of the spectrometer types considered for HIE-ISOLDE. One focus of this thesis is simulations and calculations to compare various spectrometer types, see chapter 6.

4.1 Experimental setup

The neutron-rich nuclei studied in this work were populated using multi-nucleon transfer reactions at Laboratori Nationali di Legnaro (LNL) in Padova, Italy. A primary beam of ^{82}Se impinged on a 500-μg/cm^2 thick self-supporting ^{170}Er target. The beam was delivered by the Tandem XTU-ALPI accelerator complex at LNL [51] and had an energy of 460 MeV and an intensity of $\sim$2 pnA. Beam-like fragments were identified event-by-event using the PRISMA magnetic spectrometer placed at the grazing angle of 52°. The energies of the γ-rays emitted by beam-like as well as target-like fragments were measured using the CLARA germanium detector array [52]. A Micro-channel Plate (MCP) detector [53] placed at the entrance of the spectrometer provides a start time as well as entrance position and angle. The ions subsequently pass through a magnetic quadrupole

that focuses the ions in the vertical direction, a magnetic dipole that bends the ions $\sim 60^{\circ}$ clockwise in the horizontal plane, and a ~ 3 m flightpath to a focal plane detector [54], as shown in figure 4.1. The final detector consists of a Multi Wire Parallel-Plate Counter (MWPPAC) that provides a second time signal and position for the ions and a padded IC placed 70 cm away from the MWPPAC that provides ΔE and total energy for the ions.

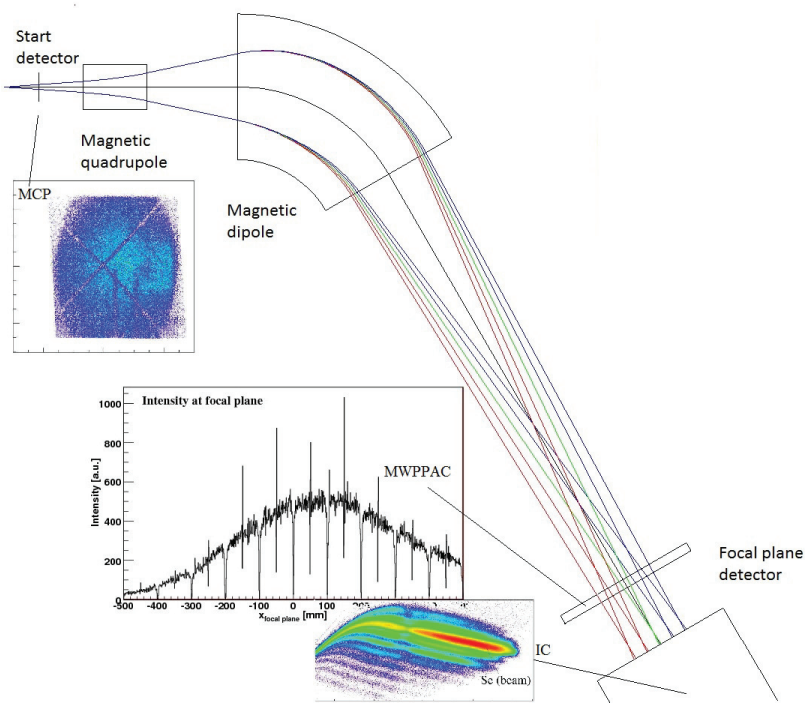

Figure 4.1: Layout of PRISMA spectrometer at LNL.

4.2 Calibration and tracking

PRISMA is a magnetic spectrometer where the identification of the ions passing through the spectrometer relies on tracking. In order to identify the detected ions the path of every single ion has to be reconstructed. This requires proper calibration of the three detectors of the setup, namely the MCP start detector at the entrance of the spectrometer, the MWPPAC at the focal plane and the IC-chamber. Reconstructing the path of the ions includes finding the total path length traveled by the ion from the target to the focal plane (l_{ion}) and the bending radius through the magnetic dipole magnet (ρ_{ion}). Details of the data acquisition system at LNL at the time of the experiment is described in [55].

4.2.1 The start detector of PRISMA

The start detector of PRISMA is a MCP detector that provides both 2D spatial coordinates and time signal. The MCP is mounted 250 mm from the target in a steel box with transparent entrance and exit windows with a 45° tilt relative to the beam axis. It is a 80x100 mm^2 rectangle mounted in a V-shape configuration as shown in figure 4.2. At the exit window of the steel box there is a $20\mu g$ carbon foil biased at $\simeq -2300$ V, while the rest of the box is biased at $\simeq -2000$ V. Electrons produced in the carbon foil as the ions transverse it are accelerated towards the MCP. The position resolution has been measured to $\simeq$ 500-600 μm and the time signal $\simeq$ 350 ps [53].

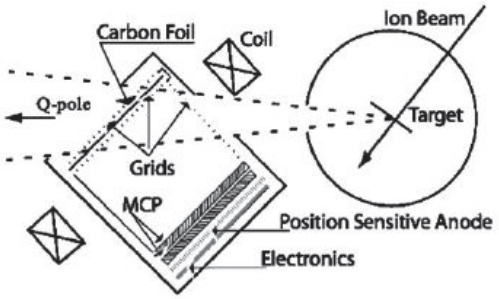

Figure 4.2: Configuration of the MCP start detector at the entrance of PRISMA, figure taken from referance [53].

A proper calibration of the space coordinates measured by the MCP detector placed at the entrance of PRISMA is very important for the overall accuracy of the track reconstruction. Errors in this calibration will propagate throughout the analysis and result in poorer mass resolution in the final step of the analysis, as

well as making it more difficult to distinguish charge states and fine tune the offset of the Time-of-flight. The detector can be calibrated both by the four points on the calibration mask placed underneath the carbon foil (see figure 4.3) and by knowledge of the size of the detector and the center of the calibration crossing. Minor distortions of the electron's path from the carbon foil to the MCP can take place because the detector is rotated 1-2° with respect to the horizontal axis. Therefore the (x, y) coordinates can be calibrated as in equations 4.1-4.2.

$$x_{cal} = a_x + b_x x + c_x y \tag{4.1}$$

$$y_{cal} = a_y + b_y y + c_y x \tag{4.2}$$

where x and y are the measured coordinates of the ions before calibration and x_{cal} and y_{cal} after calibration.

The MCP was calibrated using the coordinates for the reference points given in the PRISMA-CLARA manual on the LNL document server, and the result is shown in figure 4.3.

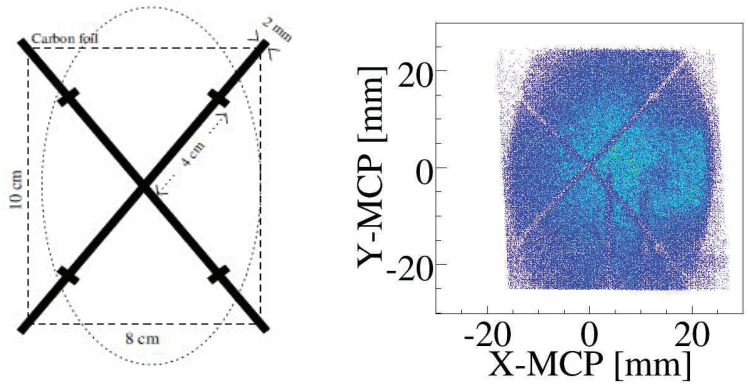

Figure 4.3: Left panel: Placement of the calibration mask, figure taken from reference [55]. The right panel shows the position distribution in the MCP detector after calibration

4.2.2 The focal plane detector of PRISMA

The focal plane detector of PRISMA [54] consists of a MWPPAC, that provides a time signal and a measurement of the spatial coordinates, and a ionization chamber providing $\Delta E - E$ measurements. The MWPPAC has a surface area of

100 x 13 cm^2 perpendicular to the optical axis and is placed at about 330 cm from the magnetic dipole. The entrance and exit windows are covered with 1.5 μm mylar foils and the detector is filled with C_6H_{10} gas at 6.5 mbar pressure (in this experiment). The detector has a central cathode and two wire planes for the x- and y-direction orthogonally oriented with respect to each others. The electrode is divided into ten independent sections each sized 100 x 130 mm^2 thus providing an x_{left} and x_{right} signal for each section, as well as a time signal and the amplitude of the cathode signal. The spatial resolution is given by the step distance of the wires; 1 mm steps for the x-direction and 2 mm steps for the y-direction.

The MWPPAC is followed by an multi-section, transverse field ionization chamber that is mounted $\approx$ 60 cm further away from the dipole. This detectors read-out is divided into 40 sections; ten divisions in the x-direction, corresponding to the ten sections of the MWPPAC, distributed over four rows in the z-direction. The divided read-out allows for creating $\Delta E - E$ plots for Z identification of the ions. The active volume of the chamber is 110·20·120cm^3 and it is filled with CH_4-gas. The maximum pressure of the chamber is 100 mbar.

The MWPPAC detector is calibrated using the width and placement of each section together. The span of the $x_{left} - x_{right}$ must equal the width of the section. This allows calibrating the X_{MWPPAC} in mm. The ionization chamber detector's 40 signals are aligned by using a pulse generator prior to the running period.

4.2.3 Track reconstruction

Once the position output of both the MCP and MWPPAC detectors are calibrated and the ionization chamber has been aligned, the tracks of the ions can be reconstructed. The tracking procedure is only applied to events where there are hits in both the MCP, the MWPPAC and a signal from the ionization chamber detector where the side pads have not fired. The tracking of the ions was carried out in accordance with the fast tracking procedure developed and used at LNL [55]. Starting with the measured position of the ion in the MCP detector (x_i, y_i), the ion's position at the MWPPAC detector can be calculated once you have made a guess for the bending radius, ρ_{guess}, through the dipole magnet. The calculated position at the MWPPAC (x_f) is compared to the measured position (X_{MWPPAC}) and the hits in the ionization chamber. The ρ_{guess} is increased or decreased depending on the difference between calculated and measured position at the MWPPAC detector. The trials end when the calculated and measured position differ $<$ 1 mm. This fast procedure assumes that the y-coordinate remains constant after the ion enters the magnetic dipole. The calculations are of first order.

The tracking procedure reconstructs the bending radius of the ion through the magnetic diple, ρ_{ion}, the total flight path, l_{ion}, the speed, v_{ion}, and the range in

the ionization chamber. This, in combination with ΔE and E as measured in the ionization chamber, both the charge state, q, and mass, A, of the ions are decided.

4.2.4 Calibration of the time-of-flight

The Time-of-Flight (τ) is found by taking the difference between the time signal from the MCP detector and from the MWPPAC. The τ-signal has random offsets that varies for the ten sections of the MWPPAC. The first step in calibrating τ is to plot τ against X_{MWPPAC}. Due to drift this has to be repeated for each run file. Then the ten sections are aligned with respect to each others. Next, τ is plotted against l_{ion}/ρ_{ion} and the offset needed to make the straight line intercept the origin of the coordinate system. Eventually, fine adjustments must be made to the offset of τ by looking at the position and FWHM of γ-ray lines after Doppler correction (see below) from known isotopes. In this experiment lines from ^{82}Se were used as this was the most strongly populated isotope and thus easy to identify.

The ratio of the mass of the detected ions to the charge state, A/q, is proportional to the product of the radius of the ions through the magnetic dipole, ρ_{ion}, and the velocity of the ions $v/c = \beta$, as expressed in equation 4.3

$$A/q \propto \rho_{ion}\beta. \tag{4.3}$$

The $\rho_{ion}\beta$ relation should remain constant for all positions in the focal plane, X_{fp}. Consequently, when all the detectors are correctly calibrated $\rho_{ion}\beta$ plotted as a function of X_{fp} should result in a series of straight lines corresponding to the different A/q states produced and detected in the experiment, as shown in figure 4.4.

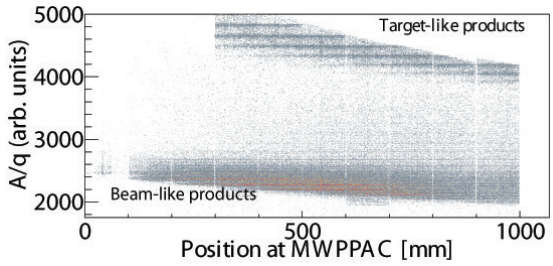

Figure 4.4: The A/q vs X_{fp} for this experiment.

4.2.5 Doppler correction

As the γ-rays are emitted by the ions in-flight, the frequency of the detected γ-ray is shifted according to the velocity of the ion and the angle between the path of the detected γ-ray and the flight path of the ion. The γ-ray energy at rest($E_{\gamma,rest}$) is given by

$$E_{\gamma,rest} = E_{\gamma,lab}\gamma(1 - \beta\cos(\theta_{p\gamma,lab})), \tag{4.4}$$

where $E_{\gamma,lab}$ is the detected γ-ray energy, $\theta_{p\gamma,lab}$ is the angle between the detected γ-ray and the ion flight-path defined as shown in figure 4.5, β is the ratio of the speed of the ion to the speed of light and $\gamma = 1/\sqrt{(1-\beta^2)}$. For the experimental set-up at CLARA-PRISMA the angular position of the HPGe-crystals are given in appendix B. The fine-correction of the Time-of-flight is done by looking at the FWHM of known peaks in the γ-ray spectra from the target-like isotopes. In this experiment the 654.75 keV $2^+ \rightarrow 0^+$ transition in ^{82}Se was used for the general fine-correction and for checking that the Time-of-flight for each of the ten sections of the MWPPAC detector were well aligned, as this transition was generously populated. A FWHM energy resolution of about 0.9% was achieved for Doppler corrected γ-ray peaks from target-like products.

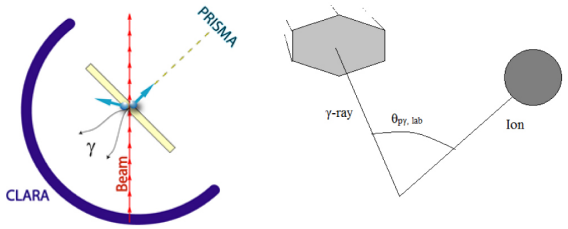

Figure 4.5: Left panel: The geometry of typical CLARA-PRISMA experiments. Right panel: Illustration displaying the angle used for Doppler correction.

In the case of the target-like ions the angle of the ion must be calculated from kinematics by assuming a binary reaction. This introduces an extra source of error explaining the difference in FWHM for Doppler corrected γ-ray lines belonging to beam- and target-like products. This introduces additional uncertainty in both the velocity and angle needed in equation 4.4 and the FWHM energy resolution for γ-ray peaks from the target-like ions was $\approx 1.1\%$ [56].

4.2.6 Ion identification

The energy signals from the ionization chamber are used to identify the element of the detected ions either by plotting $\Delta E - E$ or by reconstructing the range of

the ions and plotting this against the total energy deposited in the detector. The experimental elemental separation in this experiment is shown in figure 4.6. The charge state of the ion must be decided since $A/q \propto B\rho_{ion}/v$. The charge state, q, of the detected ion is found by plotting $\rho_{ion}v$ against the total energy deposited in the ionization chamber detector, E . The experimental charge state separation is shown in figure 4.7.

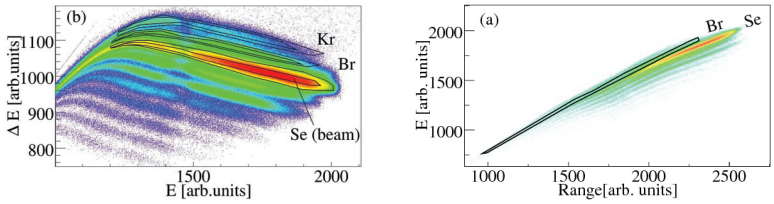

Figure 4.6: Left panel: Experimental element separation (Z-value) separation, here shown using $\Delta E - E$ from the ionization chamber detector where the signals from the first two rows of pads where summed to produce ΔE. Right panel: The resulting element separation when using the reconstructed range of the ions in the ionization chamber.

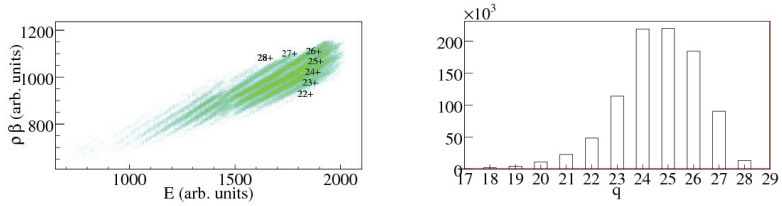

Figure 4.7: Left panel: Experimental charge state (q-value) separation, here shown for only Br-isotopes. Right panel: The resulting charge state distribution for Br-isotopes.

When q is known, the mass, A, of the detected ion is found from the experimental A/q-values. The mass spectrum for the Br-isotopes produced in the experiment is shown in figure 4.8.

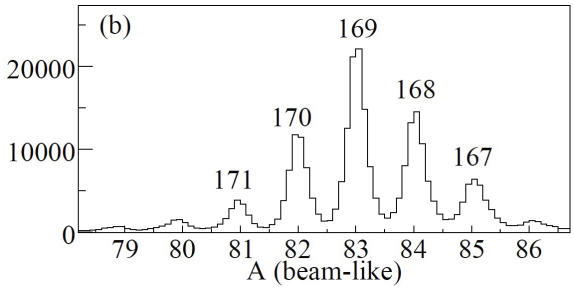

Figure 4.8: The mass spectrum for the Br-isotopes, with the corresponding Ho-channel labels shown above the mass peaks.

4.3 Experimental results for target-like reaction products

In the deep inelastic ^{170}Er+^{82}Se-reaction ≈ 50 reaction channels were open. The pressure of the focal plane detector of PRISMA was optimized with respect to the beam-like products in this experiment. The target-like events were therefore reconstructed from the kinematics by assuming a binary reaction, and the γ-rays of the events were Doppler corrected with the reconstructed velocity. The region of the nuclear chart of the beam-like isotopes accessible through the reaction is shown in figure 4.9.

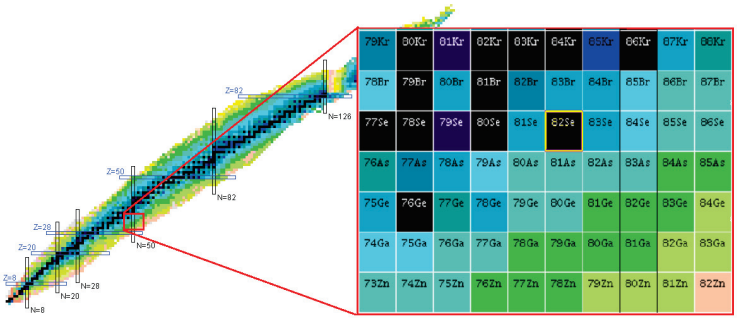

Figure 4.9: The region of the nuclear map where the products of the deep inelastic transfer reaction ^{170}Er+^{82}Se are situated.

4.3.1 Results for Ho-Isotopes

There has only been scarce experimental information available for the neutron-rich Ho-isotope. In particular, the isotopes ^{167,168,169}Ho were previously studied only in β-decay and particle spectroscopy experiments where the interpretation of data has relied on Nilsson model descriptions [57, 58, 59, 60]. The use of the CLARA [52] and PRISMA [50, 61, 62] set-ups at the Legnaro National Laboratories (LNL), employed in this study, has been demonstrated for a number of cases and is discussed in a recent investigation of neutron-rich Dy-nuclei [56]. Nuclear deformation plays an important role in nuclear synthesis, where the deformation of rare-earth nuclei has played a role in explaining stellar abundances [63]. Experimental measurements of the nuclear deformation are lacking in many cases and the parameters are chosen according to systematics or calculated theoretically. It is therefore interesting to explore ways to extract this information in cases where direct measurements are not feasible.

The level schemes of the yrast-transitions of isotopes ^{167,169}Ho are extended to higher spins. The energy level information is used to extract the deformation parameters for the isotopes ^{167,169}Ho. The experimental and calculated level scheme is shown in figure 4.10.

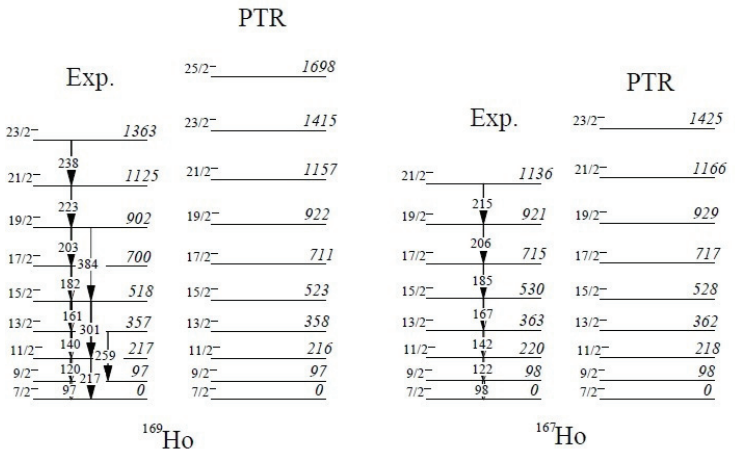

Figure 4.10: The experimental and calculated level schemes in this thesis.

Particle + Triaxial Rotor (PTR) calculations were carried out for ^{163,165,167,169}Ho using the codes GAMPN, ASYRMO and PROBAMO [64]. These codes use a modified oscillator potential and diagonalize the particle +

triaxial rotor Hamiltonian in the strong-coupling basis. The single-particle matrix elements are expressed in the deformed scheme as described in reference [65]. The standard values for the κ and μ strength parameters were used [66]. The most important input to the model is the deformation parameters ε_2, ε_4 and γ. In addition, the code also takes as input the Coriolis attenuation parameter, ζ. The rigid-body moment of inertia was normalized using the experimental energy of the first 2^+ state for the even-even nucleus considered as the core in the calculations (^{162,164,166,168}Dy). Pairing correlations were included, via a BCS approximation, using the values $G_0 = 19.2$ MeV and $G_1 = 7.4$ MeV for protons and neutrons [67].

Deformation parameters as obtained from fitting PTR calculations to experimental data and from the TRS discussed in Paper 1 included in this thesis. Deformation parameters calculated with the finite-range droplet model (FRDM) from reference [68] are also given. Rather than applying the PTR-calculations to produce level schemes, the PTR-input parameters were fitted to give the closest fit to the experimental level scheme. The deformation parameters were thus inferred from the experimental data using a χ^2-minimization procedure. Starting from the experimental level energies, E_i^{exp}, and the level energies predicted by the PTR model, E_i^{PTR}, a penalty-function was defined as:

$$\chi^2 = \frac{1}{n_{levels}} \sum_{i=7/2}^{i=I_{\max}} \frac{(E_i^{\mathrm{exp}} - E_i^{\mathrm{PTR}})^2}{\sigma^2}, \tag{4.5}$$

where the sum was taken from the ground state to the $17/2^-$ and $19/2^-$-states in ^{167}Ho and ^{169}Ho respectively. The weight, σ, is estimated with the experimental uncertainty of the excited levels included in the fit. The uncertainty of the fitted deformation parameter values was estimated by randomly varying the energy placement of the excited levels included in the fit according to the experimental uncertainty, and fitting the parameters. The results from the fit are compared to theoretical predictions for the deformation parameters in table 4.1. The fitted deformation parameter ε_2-values have reasonable uncertainties, while the sensitivity to the γ-parameter is low. This method of extracting information on the deformation shows promise for isotopes that are not experimentally available for direct measurements of quadrupole deformation. This is important for future work on isotopes with short lifetimes that can only be studied through secondary reactions in RIB-facilities. This is the first time that the deformation parameters for ^{167,169}Ho has been extracted from experimental information.

The γ-ray transitions from excited states in ^{168}Ho were identified by gating on ^{84}Br. Here one can distinguish a γ-ray transition at 143 keV. The isotope ^{168}Ho has been studied in β-decay from ^{168}Dy in previous work. The level scheme of ^{168}Ho can e.g. be found in reference [60]. In that study the 143 keV transition was assigned as a $(1)^- \rightarrow 3^+$ isomer, with a half life longer than 4 μs. A life

Table 4.1: Deformation parameters as obtained from fitting PTR calculations to experimental data and from the TRS-calculations discussed in Paper1 included in this thesis. Deformation parameters calculated with the finite-range droplet model (FRDM) from reference [68] are also given.

Isotope	Method	ε_2	γ	ε_4	ζ
	χ^2+PTR	0.24±0.0020	-0.2±0.72	-0.097±0.03	0.5±0.005
^{163}Ho	TRS ($\hbar\omega$= 0.0)	0.255	3.678	-0.041	
	TRS ($\hbar\omega$= 0.1)	0.254	-3.590	-0.039	
	TRS ($\hbar\omega$= 0.2)	0.253	-5.732	-0.041	
	FRDM	0.258		0.007	
	χ^2+PTR	0.246±0.0023	0.55±0.74	0.039±0.027	0.5±0.006
^{165}Ho	TRS ($\hbar\omega$= 0.0)	0.261	3.398	-0.036	
	TRS ($\hbar\omega$= 0.1)	0.260	0.209	-0.033	
	TRS ($\hbar\omega$= 0.2)	0.260	-4.644	-0.035	
	FRDM	0.267		0.020	
	χ^2+PTR	0.263±0.0022	1.0±0.4		0.500±0.001
^{167}Ho	TRS ($\hbar\omega$= 0.0)	0.266	0.439	-0.027	
	TRS ($\hbar\omega$= 0.1)	0.264	0.231	-0.026	
	TRS ($\hbar\omega$= 0.2)	0.263	-0.646	-0.025	
	FRDM	0.267		0.033	
	χ^2+PTR	0.261±0.0038	0.27±0.33	0.097±0.026	0.500±0.003
^{169}Ho	TRS ($\hbar\omega$= 0.0)	0.264	0.135	-0.018	
	TRS ($\hbar\omega$= 0.1)	0.264	0.152	-0.017	
	TRS ($\hbar\omega$= 0.2)	0.264	-0.312	-0.034	
	FRDM	0.275		0.040	

time of this magnitude is not compatible with this work, as only prompt γ-ray transitions are analyzed. The γ-ray gated spectra for the previously observed 488 keV transition is observed together with a close lying transition at 483 keV. Both of these transitions are unique to ^{168}Ho. When gating on the 488 keV-line, which according to Ref. [60], decays to the 143 keV level in ^{168}Ho, the 143 keV γ-ray line is not seen. However, gating on the 483 keV γ-ray line, that also is unique for ^{168}Ho in this experiment, the 143 keV γ-ray line is seen. This is an indication that the ordering of levels is likely different than previously suggested. A new ordering of levels is suggested, as shown in figure 4.11.

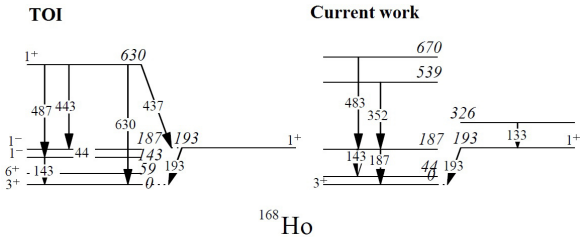

Figure 4.11: The suggested ordering of levels in this work and the ordering given in reference [69].

In conclusion, the present results prove the suitability of multi-nucleon transfer reactions as a means to study the nuclear properties of neutron-rich rotational nuclei. A new method to extract deformation parameters for well deformed nuclei.

Chapter 5

Statistical properties of warm nuclei

The nuclear physics group in Oslo has developed a method for simultaneous extraction of the level density and radiative strength function. The application of the Oslo method to nuclear reaction data has provided several interesting results, such as experimental evidence for the sequential breaking of nucleon Cooper pairs [70, 71], pygmy resonances [72, 73] and a so far unexplained enhancement of the radiative strength function for low γ-ray energies [74, 75]. The level density of atomic nuclei provides information on the degree of disorder. Thermodynamical quantities such as entropy, temperature and heat capacity can be derived within the microcanonical ensemble from the level density. This has provided interesting insight in the statistical properties of atomic nuclei [76, 77, 78, 79, 80]. The possible systematic errors of the Oslo method are discussed in reference [81].

Theoretical models tend to deviate from experimental results in the quasi-continuum excitation energy region [82]. In addition, large enhancements, compared to theoretical predictions, of the radiative strength function for low γ-ray transition energies has been observed in several isotopes in the $50-100$ mass region [74, 75, 83, 84, 85], including the radiative strength function of ^{46}Ti. The effect has been seen in experiments applying other techniques than the Oslo method, see e.g. [86]. Figure 5.1 shows how the experimentally extracted radiative strength function shows an enhancement ≈ 10 times compared to the GDR-tail for low energies. The enhancement of the radiative strength function has not been observed in the mass region of the Sn-isotopes or rare-earths. The Cd-isotopes are intermediate to the region of the nuclear chart where an enhancement of the radiative strength function has been observed and the region where there is no evidence of any enhancement. It is therefore interesting to study the radiative strength function for Cd-isotopes.

Level densities and radiative strength functions are, together with optical potentials, a key ingredient of Hauser-Feshbach models when accurate

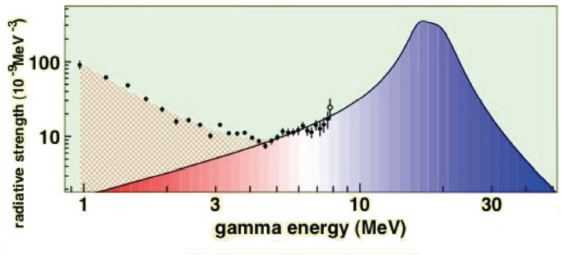

Figure 5.1: The points indicate radiative strength function of ^{57}Fe extracted as compared to the GDR-tail, see reference [83].

calculations are needed for all excitation energies [87, 88]. Most cross-section calculations for astrophysical applications depend of Hauser-Feshbach model to some extent. For very short-lived isotopes that need to be included in network calculations, it is not possible to experimentally study the level density and thus theoretica l models are needed. The accuracy of network calculations depend substantially on the accuracy of the level density input [89, 90, 91]. The proton-rich Ti-isotopes are of great importance to nuclear astrophysics. For this reason a series of experiments to study the radiative strength function and level densities of Ti-isotopes was conducted at OCL. In particular the level density and radiative strength function of ^{44}Ti are important to understand the observed abundance of this isotope in the youngest known galactic supernova remnant; Cassiopeia A (Cas A). The calculations for the ^{40}Ca$(\alpha,\gamma)^{44}$Ti reaction, mainly responsible for the presence of ^{44}Ti, can be improved with an increased knowledge of its level density and radiative strength function.

5.1 Experimental details

The Oslo Cyclotron Laboratory (OCL) has a Scanditronic MC-35 cyclotron that delivers beam for nuclear physics experiments. The layout of the cyclotron and experimental hall is shown in figure 5.2. The analyzing magnet, a magnetic dipole with adjustable slit and poles shaped to focus both in the horizontal and vertical direction, provides sharp beam energy with typical energy spread of $\approx$ 0.1-0.2%.

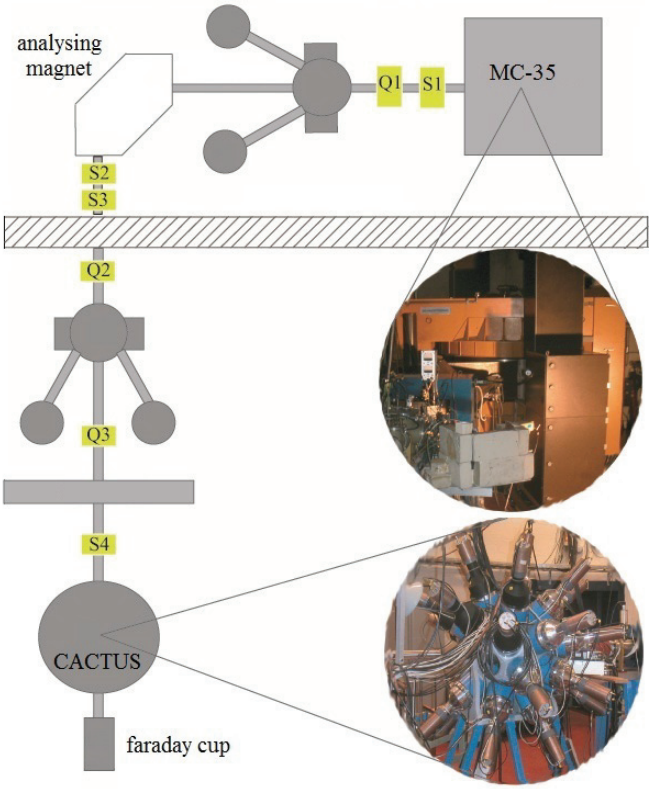

Figure 5.2: Layout of the cyclotron and experimental hall at OCL.

5.1.1 Experimental setup for the Ti-experiments

Details for the reaction and target used in the experiment described in this section is given in table 5.1. The experiment lasted for ten days and the average beam intensity was ≈ 0.5 nA of 32 MeV protons. In this experiment eight collimated $\Delta E - E$ Si detectors were used to detect the charged particles emitted from reactions in the target in coincidence with γ-rays from the reactions. The front detectors were ≈ 140 μm thick and the back detectors were 1500 μm. The emitted γ-rays were detected with the collimated NaI(Tl) scintillator detectors of the multidetector setup CACTUS [92]. The scintillator signal is read out with a photo multiplicator tube (PMT). A schematic illustration of both types of detectors is shown in figure 5.3. CACTUS covers 17.7% of 4π and the total efficiency

has been measured to be 15.2 % for 1.3 MeV γ-rays, while the relative energy resolution is $\approx$ 6% for 1.3 MeV γ-rays. The NaI(Tl)-crystals are 5"$\times$5". In addition an HPGe detector was mounted as a monitor detector. The eight particle telescopes cover $\approx$0.2% of 4π sr. In this experiment brass collimators sized 6×10 mm^2 where mounted. The energy resolution is broadened by the large solid angle covered by each particle telescope and the average energy resolution was $\approx$ 270-330 keV FWHM[1] for the experiment discussed here. The beam intensity is measured with a Faraday cup after the target chamber and CACTUS setup.

Table 5.1: Target composition and reaction details.

Target Composition	Isotope enrichment	Thickness [mg/cm^2]	Reaction of interest	Beam energy
^{46}Ti	86.0%	3.0	^{46}Ti(p,tγ)^{44}Ti	32 MeV
^{47}Ti	1.6%			
^{48}Ti	10.6%			
^{49}Ti	0.8%			
^{50}Ti	1.0%			

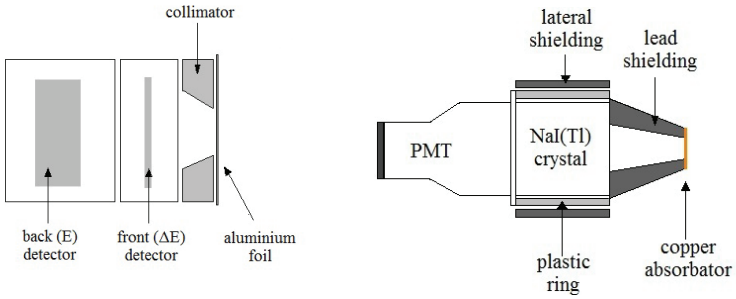

Figure 5.3: Left panel: A schematic drawing of the $\Delta E - E$ particle detectors used in the experiment. Right panel: A schematic drawing of the NaI scintillator detectors used to detect γ-rays.

The master gate is opened and events accepted and stored in this experiment satisfied the following conditions:

1. One and only one front detector gave a signal

[1]This experiment took place in November 2006 prior to the upgrade to the SIRI particle detectors

2. The signal from this front detector $>$ 1.0 MeV (corresponding to protons)

3. No other front detectors gave a signal $>$ 1.0 MeV within $\pm$ 4 μsec

4. When a front detector gives a signal there must be a signal from a back detector within 50 ns

Events are created event-by-event and the stored data have the following structure $\{E, \Delta E, E_{\gamma_1}, T_{\gamma_1}, E_{\gamma_2}, T_{\gamma_2}, \ldots, E_{\gamma_n}, T_{\gamma_n}\}$. Details of the data acquisition at the time this experiment was conducted can be found in ref. [93].

5.1.2 Experimental setup for the Cd-experiments

The Cd-experiments were carried out after the SiRi particle detector [94] was installed. SiRi consists of eight trapeziums modules mounted at a fixed angle with respect to the beam axis. The distance to the target is 5 cm. The spacial distribution of the trapeziums is illustrated by the photo of the detector setup in figure 5.4. The front (ΔE) detector of each trapezoid are assigned to individual

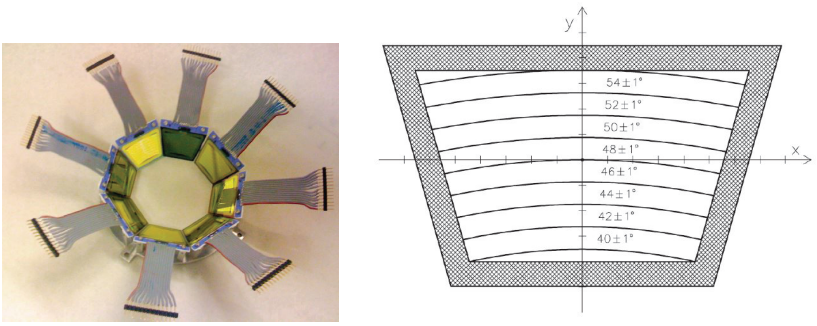

Figure 5.4: Left panel: The eight trapeziums of SIRI distributed on a ring. Right panel:The front of one of the SiRi trapeziums, which has eight arch-shaped ΔE detectors. The angular assignments of each of the ΔE detectors are indicated in the figure. One tick on the axes corresponds to 2 mm in reality.

angles of $40-54^\circ$, as illustrated in the right panel of figure 5.4. Each trapezium consists of eight independent ΔE pads and one common E detector on the back. In total, SiRi has 64 $\Delta E - E$ detectors. The detector thicknesses are 130 μm (ΔE) and 1550 μm (E). A conic Al absorber with a mass thickness of 2.8 mg/cm^2 covers the front of the trapeziums in order to stop δ electrons. As each tick on the axes in figure 5.4 corresponds to 2 mm in reality, each detector is less than 2

mm wide in the y-direction. As the old Si detector system had a 6 mm opening in this direction, SiRi gives an improvement in the energy resolution from less spread in the scattering angle. In addition, there is an improvement in the detection efficiency from a larger total solid-angle coverage $\approx 6\%$.

5.2 Data analysis

5.2.1 Selecting reaction of interest

The front and back Si-detectors were calibrated using the elastic peak and known levels in ^{46}Ti. The reaction of interest was selected by selecting the data corresponding to the tritium ions in the $\Delta E - E$ plot. The $\Delta E - E$ plot is shown in figure 5.5, where the energy deposited by particles in the front detectors is plotted against the energy deposited in the back detectors.

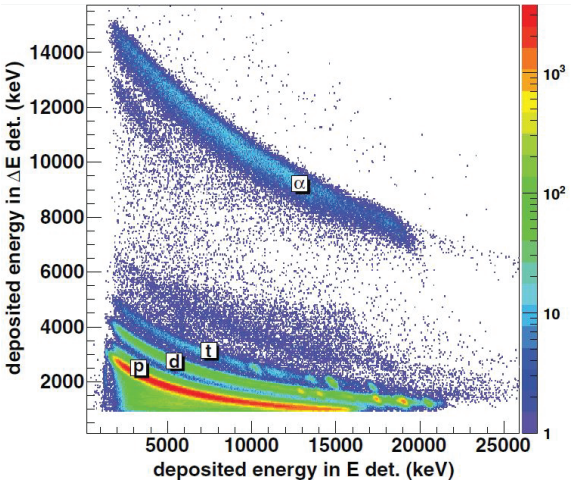

Figure 5.5: $\Delta E - E$-plot for the ^{46}Ti+p experiment, showing the reaction channels populated in the experiment.

The Cd-experiments were carried out with self-supporting ^{106}Cd (96.7 %) and ^{112}Cd (99.5 %) targets and 38 MeV ^{3}He beam. Gates were set on ^{3}He and α particles, corresponding to the ^{105,106,111,112}Cd-isotopes.

5.2.2 Time-spectra gating

The γ-ray spectra were energy calibrated using known peaks from the surroundings. The background from natural radioactive sources in the laboratory is reduced by gating on the prompt time peak and subtracting the background by gating on the smaller peak in the region next to the prompt peak as shown in figure 5.6.

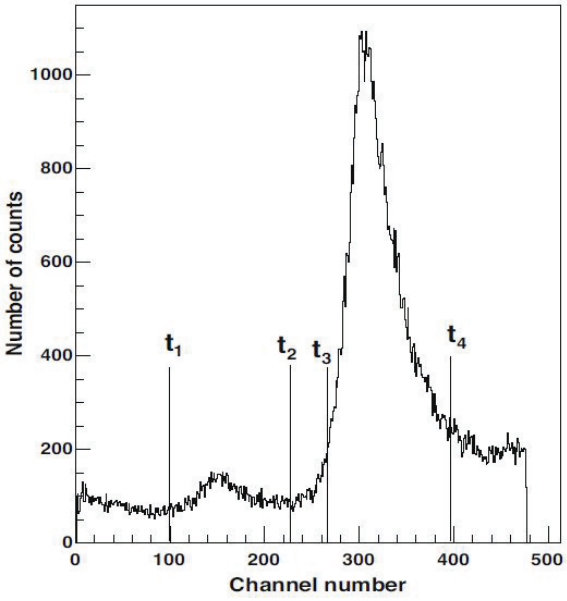

Figure 5.6: The time difference between the particle time signals and the NaI time signals, after the alignment of the time signals from CACTUS. The events with signals arriving in the interval (t_1, t_2) are used for the background spectrum and the events arriving in the interval (t_3, t_4) are the prompt events.

5.2.3 Particle energy-γ-ray energy matrix

Once the reaction of interest has been selected and the background has been subtracted one can construct a matrix where the excitation energy of the isotope of interest, E_x, is plotted against the γ-rays seen in coincidence with particles corresponding to this excitation energy. This matrix is the starting point for the Oslo method.

5.3 The Oslo method

The Oslo method is a procedure that allows the simultaneous extraction of level density and radiative strength function from particle-γ-ray coincidences. The Brink-Axel hypothesis [95, 96] is believed to valid for the quasi-continuum in the isotopes studied. This assumption can mathematically be formulated as

$$P(E_x, E_\gamma) \propto \tau(E_\gamma) \cdot \rho(E_x - E_\gamma) \tag{5.1}$$

Where $\tau(E_\gamma)$ is the transmission coefficient, $\rho(E_x - E_\gamma)$ the level density and $P(E_x, E_\gamma)$ the first generation matrix. Given that the γ-ray decay taking place in the quasi-continuum is of multipole L, then the radiative strength function can be calculated from the normalized transmission coefficient by the following relation

$$f(E_\gamma) = \frac{1}{\pi} \frac{\tau(E_\gamma)}{E_\gamma^{2L+1}} \tag{5.2}$$

where $f(E_\gamma)$ is the radiative strength function (RSF).

5.3.1 Unfolding the γ-ray spectra

The first-generation method requires full-energy γ-ray spectra for each excitation energy bin of the atomic nuclei studied. The γ-ray spectra are unfolded using the response function for the CACTUS array. Thus the γ-ray spectra are corrected for each bin of excitation energy are corrected for the escape peaks, annihilation peak, Compton scattering events and the detector efficiency [97]. The matrix elements, R_{ij}, of the response matrix $\mathbf{R}$ relate the response in energy channel i when the detector is hit by γ-rays with an energy corresponding to energy channel j. For the incident γ-ray energy channel j, the response function is normalized so that $\sum_i R_{ij} = 1$. The folding can then be expressed as

$$f = \mathbf{R}u \tag{5.3}$$

where f is the folded γ-ray spectrum and u is the unfolded.

1. As the first trial function u_0 for the unfolded spectrum, the observed (raw) spectrum r is used, setting
$$u_0 = r. \tag{5.4}$$

2. The first folded spectrum f_0 is then calculated as
$$f_0 = \mathbf{R}u_0. \tag{5.5}$$

3. The next trial function u_1 is obtained by adding the difference spectrum rf_0 as a correction to the original trial function u_0 giving

$$u_1 = u_0 + (rf_0). \tag{5.6}$$

4. The new trial function u_1 is folded again to get the next f_1, which again is used to generate the next trial function

$$u_2 = u_1 + (rf_1) \tag{5.7}$$

5. Steps 2-4 is repeated until convergence is attained, $f_i \approx r$

5.3.2 First generation γ-rays

Spectra with the first γ-rays emitted in cascades from the populated excitation energies are extracted using an iterative subtraction procedure called the "first generation method" [98]. See figure 5.7 for an illustration of the principle of the first generation method.

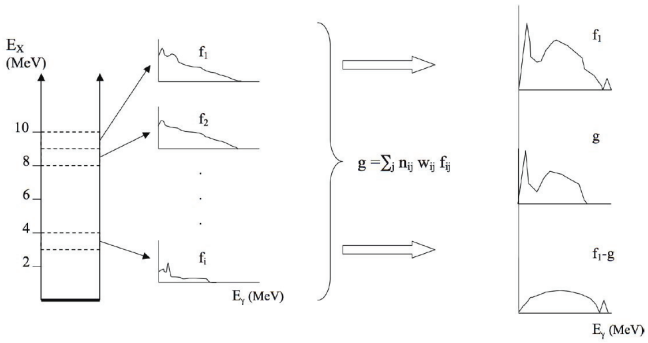

Figure 5.7: Illustration of the principle of the first generation method, the figure is adopted from reference [92].

5.3.3 Extraction of level density and radiative strength function for ^{44}Ti

Given a matrix of first generation γ-ray spectra, the experimental level density, $\rho(E_x)$, and average γ-ray transition probability, $\tau(E_\gamma)$, can be extracted. This

is achieved through a global χ^2-minimization of $\rho(E_x)$ and $\tau(E_\gamma)$ to the experimental first generation matrix [99].

$$\chi^2 = \frac{1}{n_{df}} \sum_{E=E^{min}}^{E^{max}} \sum_{E_\gamma=E_\gamma^{min}}^{E_\gamma^{max}} \left(\frac{P_{th}(E,E_\gamma) - P(E,E_\gamma)}{\Delta P(E,E_\gamma)}\right) \tag{5.8}$$

$$P_{th}(E,E_\gamma) = \frac{\rho(E-E_\gamma)\tau(E_\gamma)}{\sum_{E_\gamma-E_{\gamma min}}^{E} \rho(E-E_\gamma)\tau(E_\gamma)} \tag{5.9}$$

As the factorization of the first generation matrix into $\rho(E_x)$ and $\tau(E_\gamma)$ has an infinite number of possible solutions, as shown by equations 5.10 and 5.11, the functions must be normalised by using boundary conditions to fix the free parameters A, B and α of the following equations:

$$\tilde{\rho}(E-E_\gamma) = A\exp[\alpha(E-E_\gamma)]\rho(E-E_\gamma) \tag{5.10}$$

$$\tilde{\tau}(E_\gamma) = B\exp(\alpha E_\gamma)\tau(E_\gamma) \tag{5.11}$$

The parameter A is fixed by fitting the function to known, discrete levels at low excitation energies. The values used to decide A were chosen as the values extending upwards in excitation energy to where the number of levels seen in the experiment exceeds the number of known levels, as illustrated in figure 5.8.

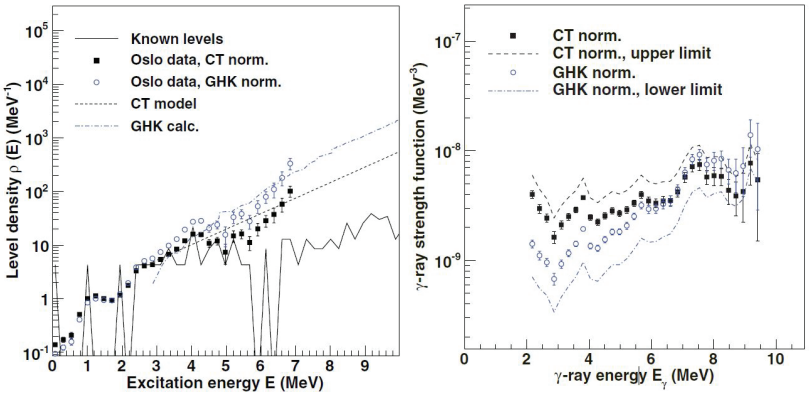

Figure 5.8: The two normalizations of the level density (left panel) and the radiative strength function (right panel) for ^{44}Ti.

As there are no measurements of the resonances at the neutron binding energy, since ^{44}Ti is an unstable isotope, the level density was extrapolated using a

theoretical description of the level density and the slope of the function was chosen so that the function intercepted the level density at the binding energy. Two alternative approaches were used, a microscopic and a closed-form formula. The calculations of Goriely, Hilaire ann Koning (GHK) was chosen as the microscopic approach and the constant-temperature (CT) formula as the closed form formula. The two level density functions resulting from the different choices of normalization are shown in figure 5.8.

The lack of experimental data on the level spacing D_0 and also the average radiative width of the s-wave resonances $\langle\Gamma_{\gamma 0}\rangle$ made assuming a value based upon the systematics of the Ti-isotopes necessary. To account for the uncertainty of such an assumption a large error for the adopted $\langle\Gamma_{\gamma 0}\rangle$-value was assumed. Given the interconnection between the level density and the radiative strength function, the two level density options result in combination with the upper and lower limit assumed for $\langle\Gamma_{\gamma 0}\rangle$ gives rise to four functions as shown in figure 5.8. Several combinations of models and model parameters were found to provide reasonable fits. The various level density and radiative strength function models were thus tested directly on the experimental primary γ-ray spectra. The model combinations taken into consideration are listed in table 5.2 and described in detail in Paper 2. The GDR parameters applied to the radiative strength function

Table 5.2: Input combinations, for the Level density function (LD) and Radiative Strength Function (RSF), utilized in this work.

Combination	LD model	RSF model	References
Input 1	CT	Fitted General Lorentzian with CT	[100, 101]
Input 2	GHK	Fitted General Lorentzian with CT	[102, 101]
Input 3	CT	Averaged Generalized Lorentzian	[100]
Input 4	GHK	Averaged Generalized Lorentzian	[102]
Input 5	CT	Standard Lorentzian	[100]
Input 6	GHK	Standard Lorentzian	

models are estimated from the values in RIPL-2 [103], as experimental values are not available. For the lower excitation energy region, any of the six input combinations result in reasonable reproduction of the data. For the high-energy region (7.4 MeV$\leq E_x \leq$ 9.8 MeV), input combinations input 2 and input 3 give the best reproduction of the experimental spectra out of the six model combinations, as seen from figure 5.9. The standard Lorentzian model in combination with the GHK level density reproduces the overall shape of the distributions rather well, while the values in absolute terms are overestimated.

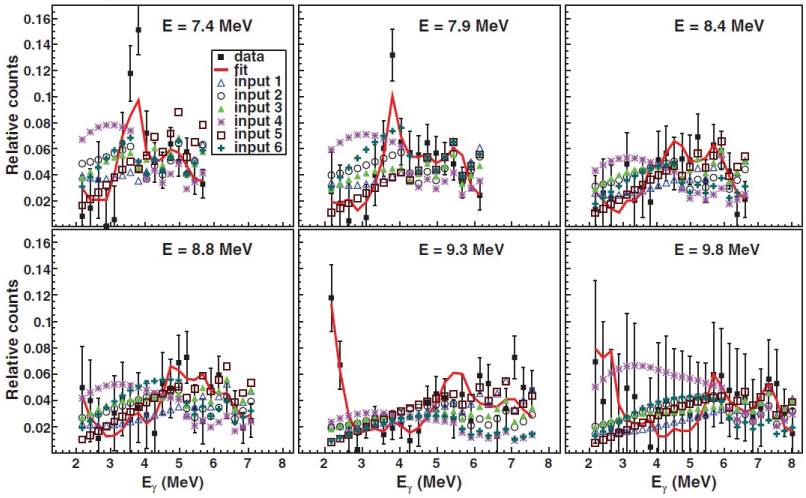

Figure 5.9: Experimental primary γ-ray spectra (solid squares) and those obtained from multiplying the extracted level density, ρ, and radiative strength, τ, functions (red line) for $7.4 \leq E \leq 9.8$ MeV. These are compared with calculated spectra using the six inputs as described in the text. The experimental and calculated spectra are given for excitation-energy bins of 0.47 MeV.

5.3.4 Extraction of level density and radiative strength function for ^{105,106,111,112}Cd.

For the isotopes ^{105,106}Cd the level density at the neutron separation energy, $\rho(S_n)$, was estimated from the systematics for the Cd-isotopes. The level density at the neutron separation energy was calculated for all Cd-isotopes where the neutron resonance spacing D_0 is known. The uncertainty of $\rho(S_n)$ for ^{105,106}Cd was set to 50 %. Two different approaches were used for interpolating between the experimental values and $\rho(S_n)$. In the upper panel of figure 5.10 the resulting level densities when applying a Fermi-gas (FG) approach is shown. As a second approach, the combinatorial and Hartree-Fock-Bogoliubov approach of reference [102] was applied. The resulting level density for this approach is shown in the lower panel of figure 5.10. The reactions studied are expected to polulate a narrow spin range. Thereofre, a reduced spin-cutoff parameter, $\tilde{\sigma} \approx 4.5$, has also been taken into account. In the case of ^{112}Cd, both the level spacing of the neutron resonance, D_0, and the average radiative width of the s-wave resonances $\langle \Gamma_{\gamma 0} \rangle$ are experimentally known [103]. Four normalizations for the level density of ^{112}Cd

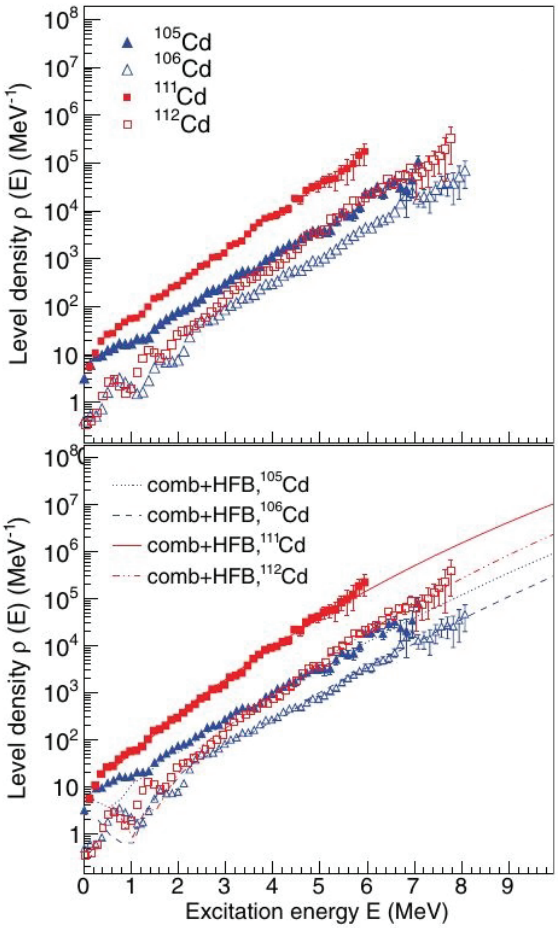

Figure 5.10: Upper panel: Normalized level densities with a Fermi-gas approach. Lower panel: Normalized level densities with a combinatorial plus Hartree-Fock-Bogoliubov approach.

is shown in figure 5.11. The effect of the reduced spin range is not large at low excitation energies, but is of importance for higher excitation energies. The effect can be as much as a factor of 2, for example at $E = 7.9$ MeV. For ^{105,106}Cd $\langle\Gamma_{\gamma 0}\rangle$ is estimated from the systematics of the Cd-isotopes.

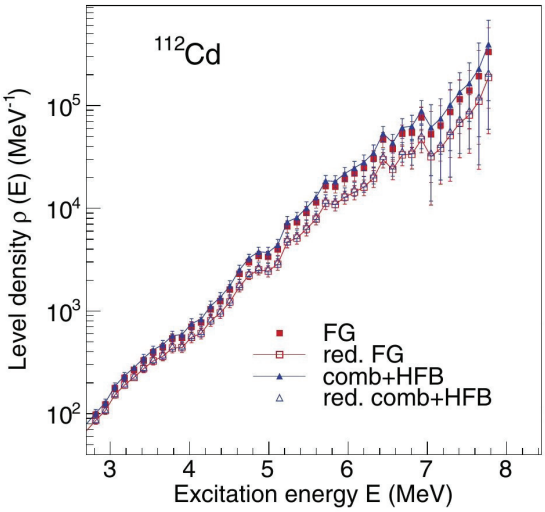

Figure 5.11: Four normalizations of ^{112}Cd: the Fermi-gas approach (FG, red squares), FG approach with a reduced spin-cutoff parameter (red, open squares), the combinatorial plus HFB approach (blue triangles), and with a reduced spin range (open, blue triangles).

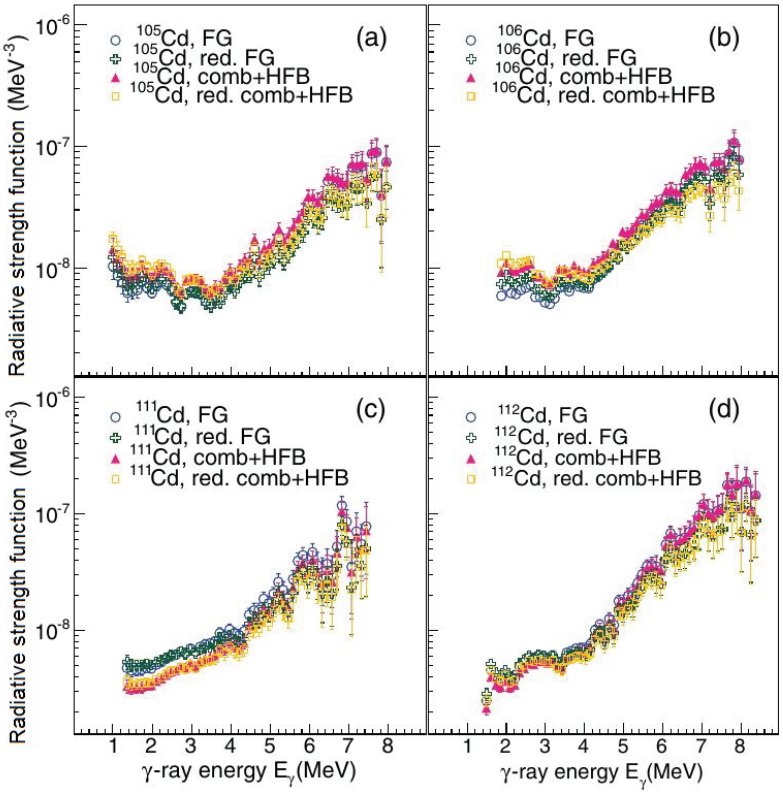

Figure 5.12: The radiative strength function of (a) ^{105}Cd, (b) ^{106}Cd, (c) ^{111}Cd, and (d) ^{112}Cd for the four normalization approaches on the level densities discussed in the text.

5.4 Results for ^{44}Ti

The results for the RSF are consistent with the RSF being independent of temperature, as illustrated by figure 5.9, in accordance with the Brink hypothesis. In spite of that, the averaged generalized Lorentzian model with a variable temperature averaged over the excitation-energy region, also gives a rather good description of the overall shape of the RSF data when normalized to the CT level density.

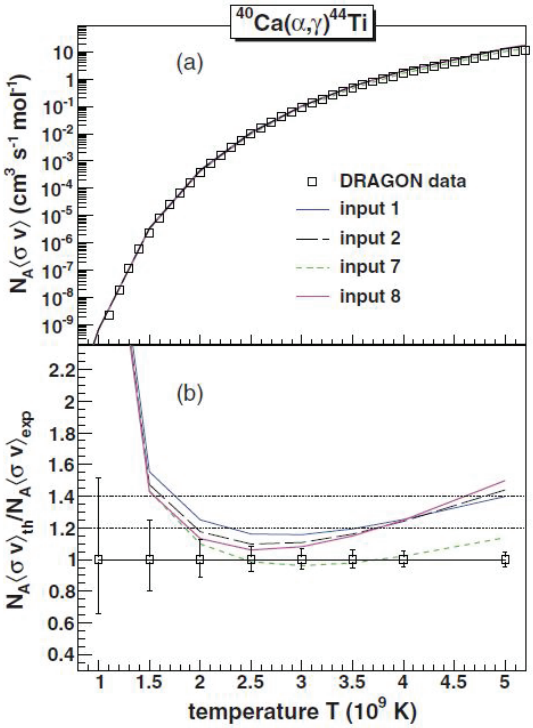

Figure 5.13: Data on the Maxwellian-averaged reaction rate for the ^{40}Ca$(\alpha,\gamma)^{44}$Ti reaction from reference [104] are compared to calculations with varying inputs described in Paper 2 included in this thesis. (b) Ratio of the calculated of the reaction rates to the experimental data. The upper dotted line indicates a 40% deviation from the experimental data and the lower dotted line indicates a 20% deviation.

The Maxwellian averaged reaction rate for ^{40}Ca$(\alpha,\gamma)^{44}$Ti is calculated with

the most consistent inputs. The data of reference [105] is the result of an integral measurement on the ^{40}Ca$(\alpha,\gamma)^{44}$T cross section corresponding to an energy window of $E_\alpha = 2.1 - 4.2$ MeV for the incoming α particles. Inputs utilizing both CT and GHK normalizations for the level density provide calculated integral cross sections that are compatible with the experimental result $\sigma_{exp}^{ave} \simeq 7.0(10)\mu b$. The calculations result in $\sigma_{ave} = 7.1$ and $6.9\mu b$ for the CT and GHK normalization respectively. The cross section calculations are also compared to the DRAGON data, as shown in figure 5.13. Input 1 and 2 are the model and parameter combinations that provided best consistency with the integral measurement, while input 7 gives the best consistency to the DRAGON data. There is a discrepancy between the cross section measurement results of references [105] and [104], making simultaneous optimization for the results of both experiments not possible.

One aim was to establish whether a significant enhancement of the RSF at low γ-ray energies is present in ^{44}Ti and what importance such an enhancement would have for the production of the isotope in stellar environment. The data are compatible with an low energy enhancement of the RSF, but the presence of such an enhancement is not necessary to produce a consistent set of LD function and RSF. The enhancement of the RSF does not have a significant impact on the neutron capture cross section. This is consistent with previous results that indicate that the low energy enhancement of the RSF has greatest importance for the neutron capture cross section of reactions involving neutron rich nuclei, as discussed in reference [106].

5.5 Results for the Cd-isotopes

The results for ^{105,112}Cd are compared to results for other isotopes that have been investigated in this mass region, see figure 5.14. The radiative strength functions of ^{111,112}Cd show no strong enhancement for the low γ-ray energies. All the Cd-isotopes investigated have strong similarities to ^{117}Sn at higher γ-ray energies. ^{105,106}Cd show a moderate low energy enhancement of the radiative strength function, compared to ^{117}Sn. The radiative strength function of ^{105}Cd carries in this sense a resemblance to both that of ^{95}Mo and ^{117}Sn. To further investigate the nature of the radiative strength function of ^{105}Cd calculations were carried out. The GLO model was adopted and the extra strength of the Sn isotope was modeled as a Gaussian function (pygmy resonance). Such a Gaussian resonance must also be included for the $E_\gamma \sim 5 - 8$ MeV region for ^{105}Cd. The results of the calculations are shown in figure 5.15, together with available photo-nuclear data. Previous studies of nuclei with fewer protons than Cd have all shown a low energy enhancement of the radiative strength function. Nuclei with more protons

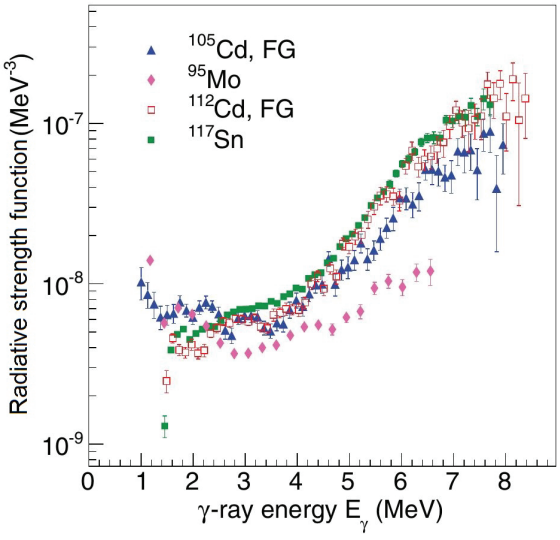

Figure 5.14: Comparison of the radiative strength functions of ^{95}Mo, ^{105,112}Cd, and ^{117}Sn.

than Cd all lack the low energy enhancement. Furthermore, the radiative strength functions of an isotopic chain have all displayed similar shape. This is the first time that a drastic change of the radiative strength function has been observed as a function of neutron number.

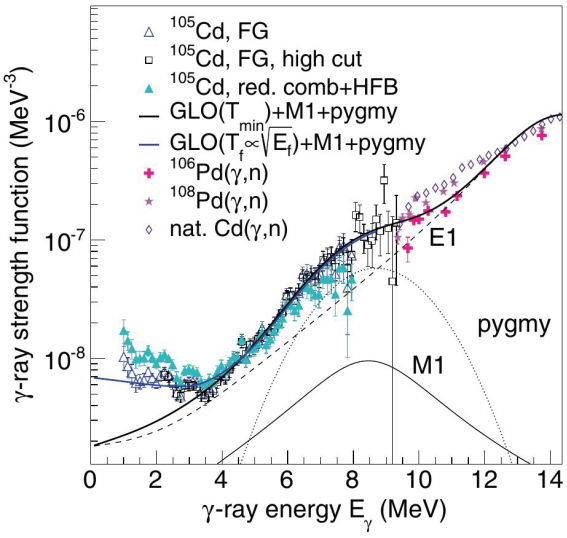

Figure 5.15: Calculations using the GLO model with a constant temperature (Tmin) and a variable temperature ($T_f \approx \sqrt{E_f}$) compared to data of ^{105}Cd for the normalization giving the lowest possible low-energy strength (FG) and the highest (combinatorial plus-HFB, reduced spin window). The black triangles show the extracted strength function for a higher cut on E_γ and E in the first-generation matrix of ^{105}Cd . Photonuclear data from references [107, 108] are also shown.

Chapter 6

Ion-optical calculations and simulations

In this dissertation two examples of separators of have been studied in simulations having the HIE-ISOLDE upgrade in mind. A set of nuclear direct transfer reactions have been simulated using the expected beam parameters for HIE-ISOLDE. An ion-optical layout based upon the design of EMMA (recoil separator layout), currently being built at TRIUMF in Canada [45], see figure 6.1, and a second layout based upon the design of PRISMA (ray-tracing layout) at LNL in Italy (see figure 6.2) have been used. The main characteristics of the two layouts are given in table 6.1.

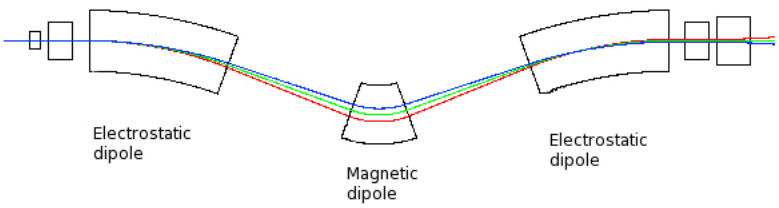

Figure 6.1: Ion-optial layout of mass-separator (not to scale).

One of the main areas of study at HIE-ISOLDE is expected to be direct reactions in inverse kinematics. The cone of the heavy recoils exiting the target will have a rather narrow angular distribution where the maximum angle of deflection, θ, mainly depends upon the mass difference between the light and heavy recoil, as illustrated by figure 6.3.

Light beams can achieve full stripping when interacting with the fixed target for the beam energies available at HIE-ISOLDE. For heavier beams, such as

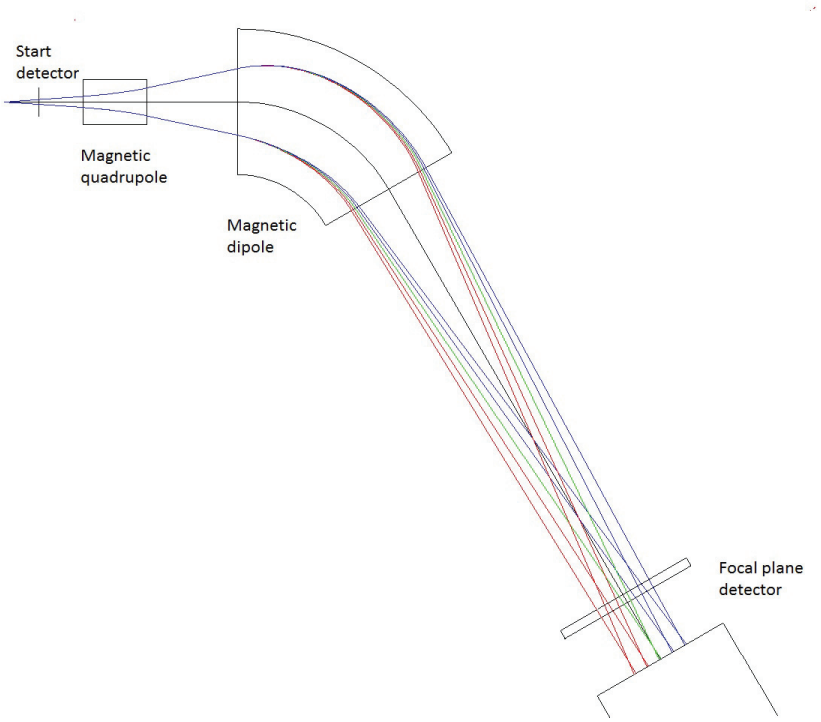

Figure 6.2: Ion-optical layout of ray-tracing spectrometer (not to scale)

Sn-isotopes, the ions interacting with the target will have a broad distribution of charge states and the maximum angle of deflection will be very small as illustrated in figure 6.4 for the case of ^{133}Sn. In other words, the recoils' deflections is comparable to the deviation of the beam. A spectrometer for reaction products

Table 6.1: Comparison between the recoil separator layout and ray-tracing layout.

Property	Recoil sep.	Ray-tracing
Solid angle	16 msr	80 msr
Horizontal angular acceptance	3.6°	10.0°
Vertical angular acceptance	3.6°	12.0°
Total flight path	9.5	5.8 m
Max. magnetic rigidity	1.0 Tm	1.32 Tm
Max. electrostatic rigidity	25 MV	-

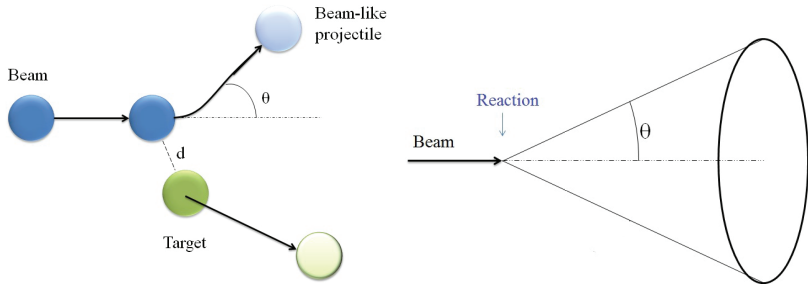

Figure 6.3: The cone of outgoing, beam-like reaction products in a two body fixed target experiment.

at HIE-ISOLDE must therefore handle high workloads (either by high beam rejection or fast readout) and cover a large solid angle.

6.1 Ray-tracing spectrometers for nuclear physics

In order to become acquainted with detectors and measurement methods utilizing ray-tracing, a data set from the PRISMA spectrometer was studied, as discussed in chapter 4. The primary code used in the simulations is the ion-optics code COSY infinity. The layout of PRISMA is shown in figure 6.2. The target chamber in PRISMA is surrounded by the CLARA gamma detector array for the detection of prompt gamma rays. At HIE-ISOLDE the MINIBALL would be used for the same purpose. Between the target chamber and the y-focusing quadrupole a Multi Channel Plate (MCP) detector [53] is placed. This gives an x-y signal with a resolution of about 1 mm for exit angle determination and a time resolution of about 400 ps for time-of-flight measurement. A focal plane detector [54] gives position, a second time signal from the Multi-Wire Parallel Plate Avalanche Counter (MWPPAC) and multiple ΔE signals from an ionization chamber. The position information from the start and focal plane detectors is used to track the particles through the spectrometer and to extract angle information in order to Doppler correct gamma spectra taken at the target position. The difference between the time signal from the focal plane and the start detector gives the time-of-flight with a resolution below 1 ns. Plotting one or two ΔE-signal versus the sum of ΔE-signals from the ionization chamber allows for the identification of the atomic number of the tracked particle.

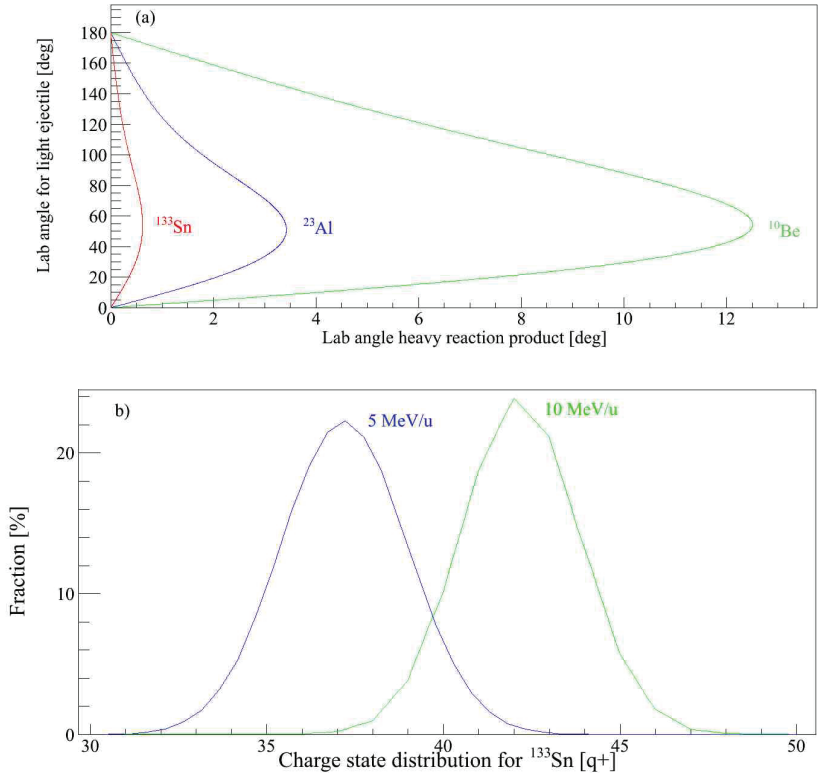

Figure 6.4: Panel a) The angular distributions of reaction products of three reactions in direct reactions in inverse kinematics at 10MeV/u beam energy. Panel b) The charge state distribution of ^{133}Sn after a 0.1 mg/cm thick deuterated polyethylene target.

6.2 Simulations

A magnetic spectrometer layout based upon PRISMA shown in figure 6.2 as well as on the EMMA design shown in figure 3.2 have been chosen for initial simulations. Table 6.1 summarizes the main characteristics of the two designs. The primary aim was to simulate a set of reactions for three different beam energies; 3 MeV/u, 5 MeV/u and 10 MeV/u with both a recoil separator and ray-tracer designs using beam parameters for HIE-ISOLDE. The focus is on the higher energies as these are most interesting for future experiments. The reactions are also simulated with different beam characteristics at the target.

The kinematics of the simulated reactions is calculated with a script written in the ROOT environment [109, 110]. The atomic masses were taken from the AME2003 evaluation [111, 112]. The studied transfer reactions have maximum scattering angles ranging from 0.3° to 7.0° relative to the optical axis. The beam transport was simulated using COSY infinity 9.0 [113] and the interaction of the particles with matter was simulated using SRIM 2008 [114] and GEANT4 [115, 116]. As input to the simulations a normalized emittance of 0.3π·mm·mrad was assumed for both the *x*-*a* and *y*-*b* planes. The beam energy is assumed to have an energy spread of 0.5 % FWHM. This corresponds to the expected yet somewhat optimistic emittance and beam energy distribution for HIE-ISOLDE. A beam waist was assumed at the target position. Figure 6.5 shows the simulated particle distribution at the target position prior to taking any interaction between target and beam particles into account.

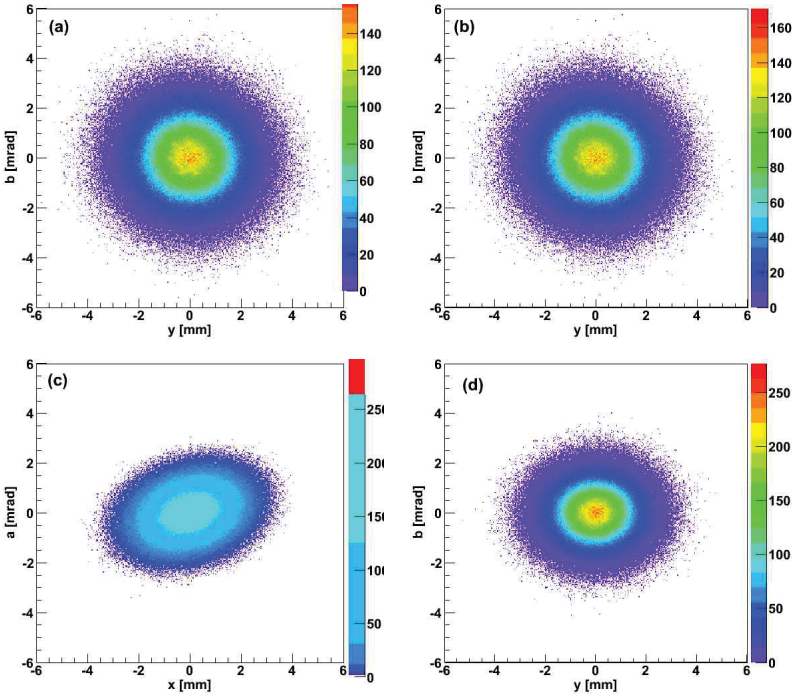

Figure 6.5: The geometric emittance distributions at the exit of the superconducting linac. The upper panels (a) and (b) show the 5.6 MeV/u stage, while panels (c) and (d) show the distributions for 10.2 MeV/u.

Nuclear reactions with secondary beams available at ISOLDE are simulated using a Monte Carlo approach. Direct transfer reactions are simulated in inverse kinematics assuming a uniform distribution with respect to the center-of-mass angle. The beam interaction with matter in detectors was simulated with the Monte Carlo simulation package, GEANT4 [115, 116] and the charge state distributions where calculated with Lise++ [117] using the model of Schiwietz and Grande [118]. The ion-optical maps used in the simulations included here were calculated using COSY infinity 9.1 [113].

COSY infinity is utilized for calculating transfer maps used in the simulations discussed here. The field settings used to calculate the transfer maps are found by fitting to obtain the relevant focus.

6.2.1 Beam parameters for HIE-ISOLDE

An example of the expected, geometric beam parameters at the exit of the HIE-ISOLDE linac for are given in table 6.2 and displayed graphically in figure 6.5. A Gaussian beam profile providing a 90% RMS geometric emittance distribution at the secondary target is assumed.

Table 6.2: The Twiss parameters (see appendix A) of the Courant-Snyder invariant for the beam profile expected at the exit of the linac at HIE-ISOLDE for $A/q \approx 4.0$ [119].

Energy [MeV/u]	$\varepsilon_{90\%rms}$ $x-x'$	α	β	γ	$\varepsilon_{90\%rms}$ $y-y'$	α	β	γ
5.9	4.34	0.27	1.00	1.07	4.05	-0.04	1.07	0.97
10.2	3.13	0.292	1.54	0.71	3.20	0.002	1.21	0.83

0 However, the emittance will depend upon the charge-to-mass ratio (A/q) of the accelerated beam. For the $A/q = 4.5$, the largest value accepted by the linac, the normalized transverse emittance, $\varepsilon_{n,90\%rms} = 0.3$ mm mrad [120]. This value is consequently used in the simulations discussed in this dissertation. It has also been assumed that the beam can be delivered at the secondary target position with any set of Courant-Snyder parameters calculated from the geometric emittance. The emittance growth from the linac exit to the secondary target position is assumed to be negligible in the simulations.

If one for example assumes a beam-spot of 1 mm diameter at the secondary target, then the conservation of the emittance results in a angular extension of the beam of about ≈ 5 mrad, as illustrated by figure 6.6. If a larger diameter of the beam-spot is acceptable, a smaller angular deviation is achieved, as shown in the graph of figure 6.6.

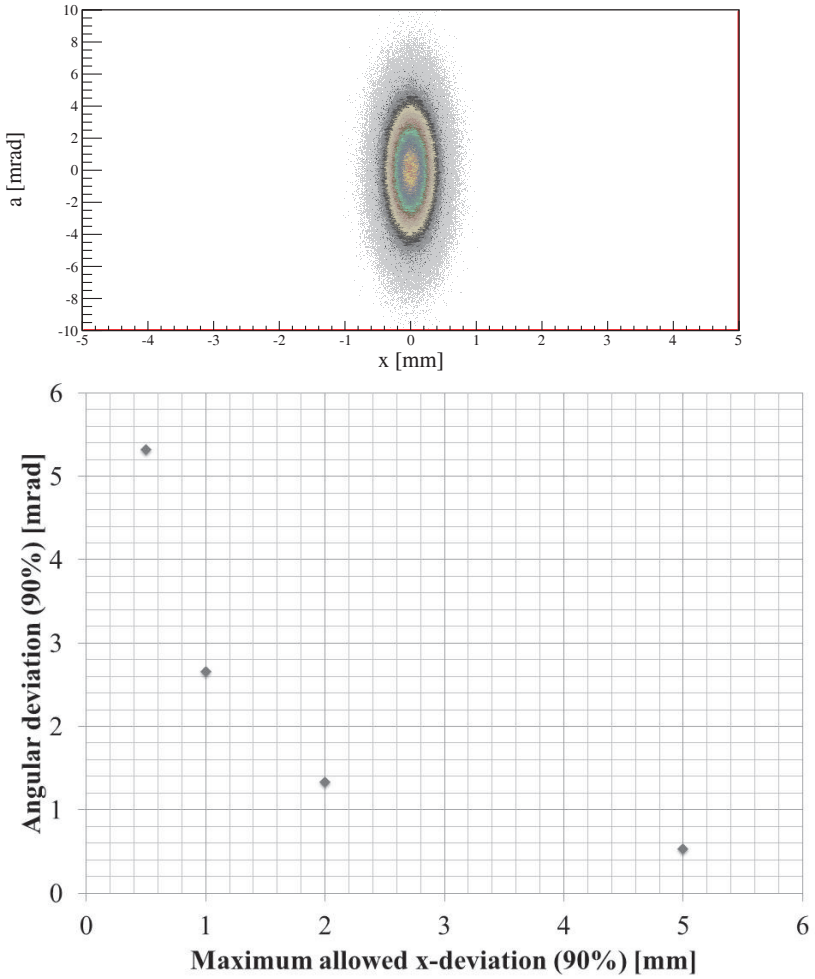

Figure 6.6: Upper panel: The emittance assuming 1 mm diameter beam-spot at the secondary target. Lower panel: How the maximum angular deviation of the beam varies with the maximum x-deviation (for $\varepsilon_{n,90\%}$ at 5 Mev/u) at the target position.

6.2.2 Reaction kinematics and charge state distributions

As previously mentioned, the heavy products of direct transfer reactions are distributed within a narrow cone with respect to the beam axis. Figure 6.7 shows the angular distribution of both a light and a heavy reaction product, for the case where a 0.1 mg/cm^2 deuterated poly-ethylen target is simulated. In the transfer reaction d(^{132}Sn,^{133}Sn)p the ion of interest, ^{133}Sn, has a maximum angular deviation from the beam axis of $\approx 0.62^\circ$. In comparison, the angular deviation of the beam is $\approx 0.3^\circ$ or $\approx$ 5 mrad when a 1 mm diameter 90% beam-spot is required. As the reaction cross section can be expected to peak at forward angle, an overlap $\geq 50\%$ between beam and reaction product must be taken into account. This implies that beam rejection or high workload is essential for physics cases similarto d(^{132}Sn,^{133}Sn)p. For the case of reactions with relatively light beams, such as d(^{9}Li,^{10}Be)n, the maximum angle of the kinematic distribution is $\approx 12-16^\circ$, making acceptance a crucial parameter.

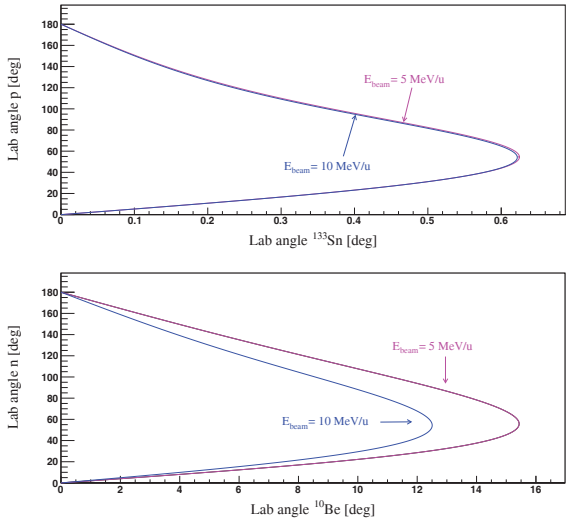

Figure 6.7: Upper panel: The angular distribution given by the kinematics of the transfer reaction d(^{132}Sn,^{133}Sn)p from ground state to ground state. Lower panel: The angular distribution of the recoil and ejectile from the transfer reaction d(^{9}Li,^{10}Be)n assuming a ground state to ground state transition.

As the HIE-ISOLDE linac accepts $A/q \approx$ 2.5-4.5 the ions have to be charge bred and lower A/q-ratio implies long breeding time for heavier ions, thus

resulting in decreased beam intensity due to decay and loss. In this dissertation the conservative value $A/q = 4.5$ has been assumed in all simulations. For a beam energy of 3 MeV/u ^{9}Li the 3^{+} charge state would comprise 92% of the intensity after passing through a 0.1 mg/cm^2 deuterated poly-ethylen target. For beam energies above 4.5 MeV/u more than 99% of the ions are fully stripped after the target. For the case of a Sn-beam passing through the same target, a large number of charge states are produced, as previously shown in figure 6.4.

6.3 Spectrometer simulation results

The impact of beam structure on the performance of a future MINIBALL+spectrometer setup at HIE-ISOLDE is an important aspect. The instantaneous ion rates per area are important parameters. Figure 6.9 illustrates the time-of-arrival distribution for beam and recoils at the focal plane for the ray-tracing layout. As there is virtually no beam rejection for $A \gtrsim 20$ as compared to the recoils for at 0°, the detector performance and the release profile from EBIS will limit the possible beam intensity that is technically feasible. For the mass separator layout it is important to set up the separator for high beam rejection.

The results from the simulated transfer reactions, with respect to yield and mass resolution, are summarized in table 6.3. The yield is defined as the fraction of the ions entering the separator and being transmitted to the focal plane detector, or in other words this figure is a combination of the geometric acceptance and the actual transmission. The detector efficiencies are not taken into account in table 6.3. The mass resolution of the ray-tracing layout is quoted for the For

Table 6.3: Simulation results for the ray-tracing layout (Alt.1) and the recoil separator(Alt.2). In $\Delta A/A$ A is the mass of interest and ΔA the FWHM of the mass peak of interest.

Reaction	Beam energy	Yield Alt.1	$\Delta A/A$	Yield Alt.2	$\Delta A/A$	Beam rej.
^{9}Li(d,n)^{10}Be	5.0 MeV/u	100%	236	54%	983	100%
^{22}Mg(d,n)^{23}Al	5.0 MeV/u	55%	256	54%	806	100%
^{68}Ni(d, n)^{69}Cu	5.0 MeV/u	99 %	327	22 %	330	88.1%
^{68}Ni(d, n)^{69}Cu	10 .0 MeV/u	97 %	319	22 %	331	87.7%
^{132}Sn(d,p)^{133}Sn	5.0 MeV/u	98 %	318	38 %	368	93 %
^{132}Sn(d,p)^{133}Sn	10.0 MeV/u	96 %	298	36 %	354	95 %
^{191}Pb(^{d}d,p)^{192}Pb	5.0 MeV/u	97 %	274	14.6 %	398	90 %
^{191}Pb(^{d}d,p)^{192}Pb	10.0 MeV/u	96 %	271	6.6 %	363	96 %

recoils heavier than ^{69}Cu, there is a decrease in yield for the case of the mass separator layout. As the mass of the recoil increases, the $\Delta A/q$ of two adjacent peaks decreases, making the mass resolution of greater importance. Due to aberrations related to the initial a and b coordinates of the recoils, the angular acceptance must be reduced.

6.4 The time structure of beams at HIE-ISOLDE

The beams at REX-ISOLDE have both a macro- and micro time structure. The macro-time structure is determined by the charge breeder realease profile (EBIS pulse) and the release from the primary target. A general overview of the time structure of HIE-ISOLDE beams is provided in figure 6.8. This again is

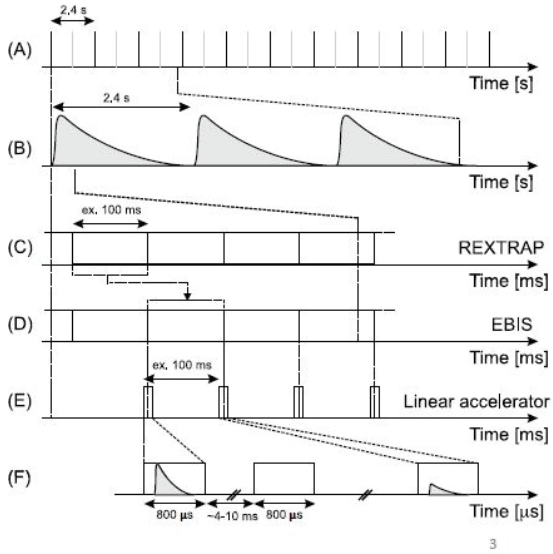

Figure 6.8: The time structure of beams at HIE-ISOLDE. (A) Protons from PSB (B) RIBs released from the ISOL target (C) Accumulation/cooling/macro-bunching (up to 100 Hz) (D) Charge breeding in EBIS (E) Duty cycle of linac matched to EBIS (F) Micro bunching of EBIS beam pulse by the RFQ at 101.28 MHz [120].

convoluted by the RF acceleration window of the accelerator. The micro structure is determined by the accelerating RF field and will be operated at 101.28 MHz.

Self-extraction gives FWHM ≈50 μs distribution while slow extraction provides a shape with FWHM optimally peaked around 300-500 μs. The trap tubes inside the EBIS limit the possibility to shape the pulse to an approximately uniform release profile. The simulations show that the maximum particle rate at the focal

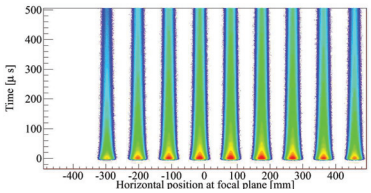

Figure 6.9: Time of arrival of ions at focal plane plotted against the horizontal position for the beam and reaction products of ^{68}Ni(d, n)^{69}Cu at the focal plane of the ray-tracing layout.The distribution for 5 MeV/u and an integrated beam intensity $I = 10^7$ particles/second is shown.

plane is $\approx 10^6$ particles per cm^2 per second if the beam rate is $\sim 10^7$ pps.

6.5 Response function for $LaBr_3$:Ce scintillator detectors at OCL

Upgrading the γ-ray detection system CACTUS with $LaBr_3$:Ce in place of NaI(Tl) would result in higher efficiency, better energy resolution and faster time signals [121]. The research group has already received two new, large volume $LaBr_3$:Ce detectors. Higher efficiency will allow for the study of reaction channels with low cross sections or to study reactions induced by low intensity beams. The improved energy resolution will allow setting gates on γ-ray lines corresponding to different spins. This in turn would allow, given high enough statistics, to study the reactions also above the particle binding energies or to study the angular dependence of the level density and radiative strength function.

As described in section 5.3.1 the unfolding procedure for the γ-ray spectra is crucial for the Oslo Method. As $LaBr_3$:Ce will respond differently to γ-rays, a new response function had to be extracted. This has been achieved through a studies of a combination of experimental data from an experimental campaign made possible by borrowing detectors and data from GEANT4 simulations, as described in details below.

6.5.1 The response function

The response function of a γ-ray detector, such as $LaBr_3$:Ce scintillator detectors, depends on the interactions with matter that the photons can undertake at the relevant energy. This includes photoelectric absorption, pair production and Compton scattering. Because Compton-scattered photons and one or both of the annihilation photons can escape from the detector and thus deposit only part of the full energy, one must correct the observed γ-ray spectra for such incompletely detected photons. Additional background from backscattered annihilation and Compton γ-rays in the experimental setup give rise to peak structures at 511 and $\approx$ 200 keV, respectively. In addition one must take into account the internal activity of the scintillator material ($\approx$ 1000 counts/second).

The energy transferred to the electron, $E_{electron}$, by the γ-ray that is scattered at an angle θ is given by equation 6.1.

$$E_{electron} = E_\gamma - \frac{E_\gamma}{1 + \frac{E_\gamma}{m_e c^2}(1 - \cos(\theta)} \tag{6.1}$$

Experimental spectra from mono-energetic γ-ray lines at 1770, 2834, 4963, 9634, 14586 and 17619 keV were used to verify the energy resolution function and to ensure the quality of the simulated data by allowing comparison. The GEANT4 simulations were in addition carried out for steps of energy of 500 keV,

starting at 500 keV and ending at 20 MeV. Between these values the response is interpolated using three point interpolation for the photon production peaks and the full energy-peak. Compton events were interpolate between channels corresponding to the same scattering angle, θ, as illustrated in figure 6.11. The scintillator material $LaBr_3$:Ce has self activity [122] that also has been accounted for.

Table 6.4: Target compositions and reaction details.

Target Composition	Enrichment/ composition	Thickness [mg/cm^2]	Reaction of interest	Beam energy
Natural Si		3.5		
^{28}Si	92.2%		^{28}Si(p,pγ)^{28}Si	16 MeV
^{29}Si	4.7%			
^{30}Si	3.1%			
Natural C		1.0		
^{12}C	98.9%		^{12}C(p,pγ)^{12}C	16 MeV
^{13}C	1.1%			

Table 6.5: Important parameters used for the $LaBr_3$:Ce material in the simulations [123].

Light yield	Y_{ph}	63 $\frac{photons}{keV} E_{dep}$
Primary decay time	$\tau_{primary}$	0.016 μsec

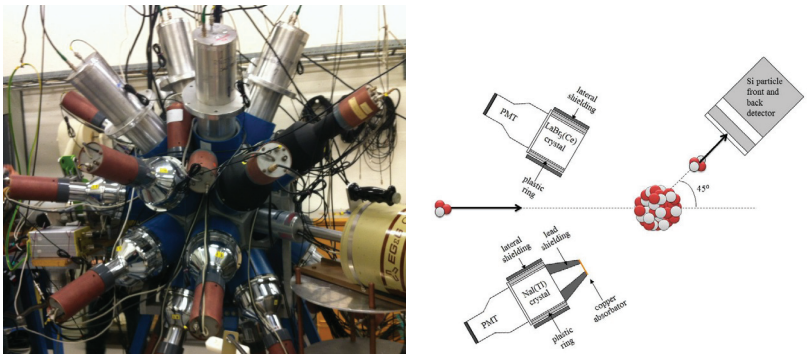

Figure 6.10: Left panel: A picture showing CACTUS with six $LaBr_3$:Ce scintillator detectors inserted. Right panel:A picture of one of the $LaBr_3$:Ce scintillator detectors with PMT.

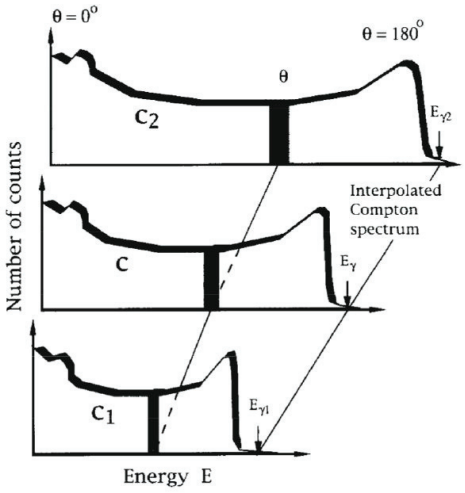

Figure 6.11: The interpolation of the Compton part of the simulated or measured response functions c1 and c2, illustrating the increase of $\Delta\theta$ with the full γ-ray energy E_γ, the figure is taken from reference [93].

6.5.2 Simulation results

A simulation that, from first principles, simulates the energy resolution of a scintillator read out by PMT must include the atomic decay of the crystal and the electron cascade the collected light produces in the PMT. Simulating with such detail is complicated and computationally demanding. Therefore, the resolution of the $LaBr_3$ detectors is simulated by adding a Gaussian spread on to the energy deposited by electrons in the crystal. The resolution of the $LaBr_3$ crystals is quoted to be 2.9% FWHM at 1.3 MeV γ-ray energy, while the photon yield is said to be 63 photons/keV deposited energy. This implies that the energy resolution due to the spread in photon numbers and the variation in the number of electrons read out of the PMT is estimated by a variance $\sigma \approx \sqrt{E_{dep}} \times 78/2.35$ as discussed in reference [124].

Chapter 7

Brief introduction to papers

7.1 Paper 1:The neutron rich isotopes ^{167,168,169}Ho studied in multi-nucleon transfer reactions

The aim of this paper was primarily to shed new light upon the nuclear structure and the macroscopic properties of the moderately neutron-rich Holmium-isotopes. The isotopes ^{167,168,169}Ho had been studied using the PRISMA and CLARA setups at INFN-LNL. The experiment was a thin-target experiment with ^{170}Er as the target and ^{82}Se as the beam. The mentioned isotopes were the target-like products that corresponded to the beam-like ^{85,84,83}Br resulting from the deep inelastic transfer reaction. Deep inelastic transfer reactions are well suited for experimental studies of the collective properties. The level schemes are extended to higher spins and revised. Particle + triaxial rotor and Total Routhian Surface calculations have been carried out for the two odd-*A* Ho isotopes. Using a minimization procedure the deformation parameters for ^{167,169}Ho are extracted and compared to theoretical calculations. The placement of an isomer in ^{168}Ho was also revisited.

This paper is submitted to EPJ A.

7.2 Paper 2: Primary γ-ray spectra in ^{44}Ti of astrophysical interest

The nucleus ^{44}Ti is a key isotope for the investigation of the inner regions of core-collapse supernovae and their young remnants. This isotope is thought to be exclusively created in supernovae, with a large variation of yields depending on the supernova type. The background for this article was the need to better understand the observed ^{44}Ti abundance in the Cassiopeia A supernova. Both

level density and radiative strength function are input in large network calculations of nuclear reaction rates.

The nuclear physics group at the Oslo Cyclotron Laboratory has developed a unique technique to extract simultaneously the level density and radiative strength function from primary γ-ray spectra. The primary γ-ray spectra for ^{44}Ti has, applying the Oslo method, been extracted from particle-γ-ray coincidence data of the ^{46}Ti$(p,t\gamma)^{44}$Ti reaction, and the level density and radiative strength function was successfully extracted. The experimentally extracted level density and radiative strength function were used to calculate reaction rates for the ^{40}Ca$(\alpha,\gamma)^{44}$Ti reaction. This reaction is considered as the main production mechanism for ^{44}Ti in the Cassiopeia A supernova. The ^{40}Ca$(\alpha,\gamma)^{44}$Ti cross section and corresponding Maxwellian-averaged astrophysical reaction rate rate was estimated.

7.3 Paper 3: Transitional γ strength in Cd isotopes

The level densities and radiative strength functions of ^{105,106,111,112}Cd have been extracted from particle-γ coincidence data using the Oslo method. The level densities are in excellent agreement with previously known levels at low excitation energy. More low-energy strength is apparent for ^{105,106}Cd than for ^{111,112}Cd. For γ-ray energies above $\approx$ 4 MeV, there is evidence for moderate extra strength, similar to what has been previously observed for the Sn-isotopes. The origin of this extra strength is unclear. Possible explanations are that the increased strength is due to $E1$ and $M1$ transitions originating from neutron skin oscillations or the spin-flip resonance, respectively. Still, the radiative strength functions display no strong enhancement for low γ-ray energies.

7.4 Paper 4: Simulations for a HIE-ISOLDE spectrometer

HIE-ISOLDE will provide a wide range of exotic beams with small emittance and beam energy of $\approx$5-10.2 Mev/u. The primary motivation of this paper was to explore the scientific scope of two different spectrometer layouts, given realistic beam characteristics at HIE-ISOLDE. A doubly achromatic, recoil-separator ion-optical layout was compared with a ray-tracing, magnetic spectrometer layout. A set of transfer reactions and a case of deep inelastic transfer reaction were simulated for different beam settings. The results showed that both spectrometer types have clear benefits and drawbacks. The results also show that for both

layouts the high instantaneous particle rate at the secondary target may provide technical challenges.

7.5 Paper 1

7.6 Paper 2

Primary γ-ray spectra in ^{44}Ti of astrophysical interest

A. C. Larsen,[1,*] S. Goriely,[2] A. Bürger,[1] M. Guttormsen,[1] A. Görgen,[1,3] S. Harissopulos,[4] M. Kmiecik,[5] T. Konstantinopoulos,[4] A. Lagoyannis,[4] T. Lönnroth,[6] K. Mazurek,[5] M. Norrby,[6] H. T. Nyhus,[1] G. Perdikakis,[4,†] A. Schiller,[7] S. Siem,[1] A. Spyrou,[4,†] N. U. H. Syed,[1] H. K. Toft,[1] G. M. Tveten,[1] and A. Voinov[7]

[1]*Department of Physics, University of Oslo, NO-0316 Oslo, Norway*
[2]*Institut d'Astronomie et d'Astrophysique, Université Libre de Bruxelles, CP 226, BE-1050 Brussels, Belgium*
[3]*Dapnia/SPhN, CEA-Saclay, France*
[4]*Institute of Nuclear Physics, NCSR "Demokritos," 153.10 Aghia Paraskevi, Athens, Greece*
[5]*Institute of Nuclear Physics PAN, Kraków, Poland*
[6]*Department of Physics, Åbo Akademi University, FI-20500 Åbo, Finland*
[7]*Department of Physics and Astronomy, Ohio University, Athens, Ohio 45701, USA*

(Received 26 July 2011; revised manuscript received 8 January 2012; published 23 January 2012)

Primary γ-ray spectra for a wide excitation-energy range have been extracted for ^{44}Ti from particle-γ coincidence data of the ^{46}Ti$(p,t\gamma)^{44}$Ti reaction. These spectra reveal information on the γ-decay pattern of the nucleus and may be used to extract the level density and radiative strength function applying the Oslo method. Models of the level density and radiative strength function are used as input for cross-section calculations of the ^{40}Ca$(\alpha,\gamma)^{44}$Ti reaction. Acceptable models should reproduce data on the ^{40}Ca$(\alpha,\gamma)^{44}$Ti reaction cross section as well as the measured primary γ-ray spectra. This is only achieved when a coherent normalization of the slope of the level density and radiative strength function is performed. Thus, the overall shape of the experimental primary γ-ray spectra puts a constraint on the input models for the rate calculations.

DOI: 10.1103/PhysRevC.85.014320 PACS number(s): 21.10.Ma, 25.20.Lj, 27.40.+z, 25.40.Hs

I. INTRODUCTION

The titanium isotope ^{44}Ti is of great astrophysical interest, because it is believed to be produced in the inner regions of core-collapse supernovae and in the normal freeze-out of Si burning layers of thermonuclear supernovae [1], with a large variation of yields depending on their type [2]. The determination of the ^{44}Ti yield might reveal information on the complex explosion conditions. The production yield of ^{44}Ti directly determines the abundance of the stable ^{44}Ca, and also influences the ^{48}Ti abundance through the feeding of ^{48}Cr on the α chain. The theoretical prediction of the ^{44}Ti production in core-collapse supernovae is sensitive to the chosen reaction network and the adopted nuclear reaction rates.

Cassiopeia A (Cas A) is the youngest known galactic supernova remnant and is, at present, the only one from which γ rays from the ^{44}Ti decay chain (^{44}Ti $\rightarrow$ ^{44}Sc $\rightarrow$ ^{44}Ca) have been unambiguously detected [2]. The discovery of the 1157-keV γ-ray line from ^{44}Ca was reported by Iyudin *et al.* [3], while measurements of the 67.9- and 78.4-keV lines from ^{44}Sc were presented by Renaud *et al.* [2]. From the combined γ-ray flux, the half-life of ^{44}Ti, and the distance and age of the remnant, an initial synthesized ^{44}Ti mass of $1.6^{+0.6}_{-0.3} \times 10^{-4} M_{\odot}$ was deduced. This is thought to be unusually large, a factor of 2–10 more than what is typically obtained by current models (see, e.g., [4,5]).

The main production reaction of ^{44}Ti is the ^{40}Ca$(\alpha,\gamma)^{44}$Ti reaction channel with a Q value of 5.127 MeV; the cross section for this reaction is very important to estimate the ^{44}Ti yield. Recent cross-section measurements on this reaction [6] have lead to an increase of the associated astrophysical rate, giving a factor of $\sim$2 more in the predicted yield of ^{44}Ti. Thus, the theoretical models become more compatible with the Cas A data; however, this would make the problem of "young, missing, and hidden" galactic supernova remnants even more serious: Supernovae that should have occurred after Cas A are still not detected by means of γ-ray emission from the ^{44}Ti decay chain. It is still an open question whether the Cas A is a peculiar case (asymmetric and/or a relatively more energetic explosion), or that the Cas A yield is in fact "normal," because it is in better agreement with the solar ^{44}Ca/^{56}Fe ratio [2].

There are many uncertainties connected to the yield estimate, the most severe ones being attributable to astrophysical issues. However, there are also significant uncertainties related to the nuclear physics input, in particular the nuclear level density (NLD), the radiative strength function (RSF), and the α-particle optical model potential. All these quantities are entering the calculation of the astrophysical reaction rates. The NLD is defined as the number of nuclear energy levels per energy unit at a specific excitation energy, while the RSF gives a measure of the average (reduced) transition probability for a given γ-ray energy. Both quantities are related to the average decay probability for an ensemble of levels and are indispensable in a variety of applications (reaction rate calculations relevant for astrophysics or transmutation of nuclear waste), as well as for studying various nuclear properties in the quasicontinuum region.

In this work, we have extracted primary γ-ray spectra from the decay cascades in ^{44}Ti populated via the two-neutron pickup reaction ^{46}Ti$(p,t\gamma)^{44}$Ti. These spectra are measured for a wide range of initial excitation energies below the neutron

*a.c.larsen@fys.uio.no
†Current address: National Superconducting Cyclotron Laboratory, Michigan State University, East Lansing, MI 48824-1321, USA.

threshold, and they put a constraint on the functional form of the NLD and RSF.

In Sec. II we describe the experimental details, give an overview of the analysis, and present the obtained primary γ-ray spectra. Different normalizations of the NLD and RSF are discussed in Sec. III, and the applied models are tested against the primary γ-ray spectra in Sec. IV. In Sec. V various input models are used for estimating the ^{40}Ca$(\alpha,\gamma)^{44}$Ti cross-section and reaction rates, and the calculated results are compared to existing data from Nassar *et al.* [6] and Vockenhuber *et al.* [1]. Finally, a summary and concluding remarks are given in Sec. VI.

II. EXPERIMENT AND ANALYSIS

The experiment was conducted at the Oslo Cyclotron Laboratory (OCL), where the Scanditronix cyclotron delivered a 32-MeV proton beam bombarding a self-supporting target of ^{46}Ti with mass thickness 3.0 mg/cm^2. The beam current was ≈0.5 nA and the experiment was run for ten days. Unfortunately, the target was enriched only to 86.0% in ^{46}Ti. The main impurities were ^{48}Ti (10.6%), ^{47}Ti (1.6%), ^{50}Ti (1.0%), and ^{49}Ti (0.8%). The reaction of interest, ^{46}Ti$(p,t\gamma)^{44}$Ti, has a Q value of −14.236 MeV [7]. Particle-γ coincidences from this reaction were measured with eight collimated Si $\Delta E - E$ particle detectors and the CACTUS multidetector system [8].

The Si detectors were placed in a circle in forward direction, 45° relative to the beam axis. The front (ΔE) and end (E) detectors had a thickness of ≈140 and 1500 μm, respectively. The CACTUS array consists of 28 collimated 5″ × 5″ NaI(Tl) crystals for detecting γ rays. The total efficiency of CACTUS is 15.2(1)% at $E_\gamma = 1332.5$ keV. Also, a Ge detector was placed in the CACTUS frame to monitor the experiment. The charged ejectiles and the γ rays were measured in coincidence event by event.

To identify the charged ejectiles of the reactions, the well-known $\Delta E - E$ technique is used. In Fig. 1, the energy deposited in the ΔE detector versus the energy deposited in the E detector is shown for one particle telescope. Each "banana" in the figure corresponds to a specific particle species as indicated in the figure.

By gating on the triton banana, the events with the reaction ^{46}Ti$(p,t\gamma)^{44}$Ti were isolated. The ^{46}Ti$(p,d\gamma)^{45}$Ti data have been published previously in Ref. [9]. The singles and coincidence triton spectra are shown in Fig. 2. We note that the excited 1.904-MeV 0^+ state ($E_t \approx 16$ MeV) is rather weakly populated. This is expected on the basis that $\ell = 0$ states are, in general, much weaker populated in the (p,t) reaction at 45° compared to, for example, $\ell = 2$ and 4 (see Ref. [10]). The populated spin range is estimated to $J \approx 0$–$6\hbar$ based on the observed triton peaks and their coincident γ-decay cascades, in accordance with the findings in Ref. [10].

Two-neutron pickup on the ^{48,50}Ti impurities in the target give rise to peaks at higher triton energies than the ground state of ^{44}Ti owing to their lower reaction thresholds; the Q values are −12.025 and −10.560 MeV for the ^{44}Ti$(p,t\gamma)^{46}$Ti and ^{50}Ti$(p,t\gamma)^{48}$Ti reactions, respectively. This means that there

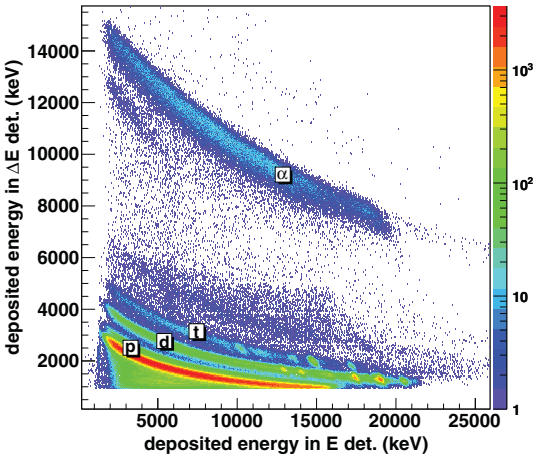

FIG. 1. (Color online) Identification of particle species using the $\Delta E - E$ technique.

is a background from such events in the spectra that cannot be removed (an ≈14% effect).

Using reaction kinematics and the known Q value for the reaction, the measured triton energy was transformed into excitation energy of the residual nucleus. Thus, the γ-ray spectra are tagged with a specific initial excitation energy in ^{44}Ti. Further, the γ-ray spectra were corrected for the known response functions of the CACTUS array following the procedure described in Ref. [11]. The main advantage of this correction method is that the experimental statistical

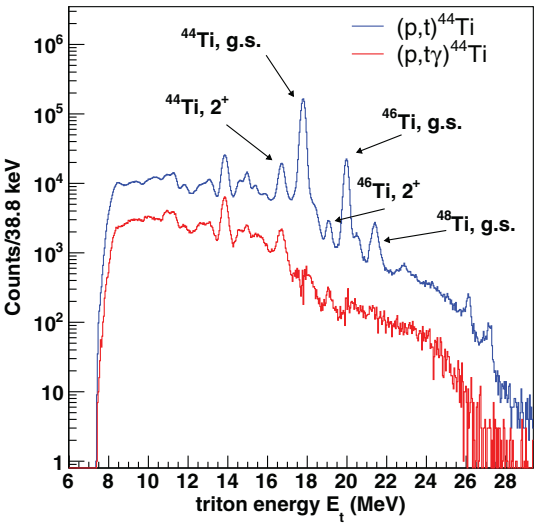

FIG. 2. (Color online) Singles (blue) and coincidence (red) triton spectra. The impurities of ^{48,50}Ti are easily seen. The resolution is ≈270–330 keV.

uncertainties are preserved, without introducing any new, artificial fluctuations.

Information on NLD and RSF can be extracted from the distribution of primary γ rays, that is, the γ rays that are emitted first in each decay cascade. To separate these first-generation γ transitions from the second- and higher-order generations, an iterative subtraction technique is used [12]. The γ-ray spectra f_i for excitation-energy bin i obviously contain all generations of γ rays from all possible cascades decaying from the excited states of this bin. The subtraction technique is based on the assumption that the spectra $f_{j<i}$ for all the energy bins $E_j < E_i$ contain the same γ transitions as f_i *except* the first γ rays emitted, because they will bring the nucleus from the states in bin i to underlying states in the energy bins j. This is true if the main assumption of this technique holds: that the decay routes are the same whether they were initiated directly by the nuclear reaction or by γ decay from higher-lying states.

The obtained first-generation matrix $P(E, E_\gamma)$ of ^{44}Ti is shown in Fig. 3. The diagonal where $E = E_\gamma$ is clearly seen. Here, two peaks are particularly pronounced: one from the decay of the first excited state at $E = E_\gamma = 1083$ keV and the other from the decay of the second 2^+ state at 2887 keV to the ground state. There are also more diagonals visible, for example, for $E_\gamma = E - 1083$ keV, where the decay goes directly to the first excited 2^+ state, and so on.

Before extracting the NLD and RSF from the P matrix, we have set a lower limit for the γ-ray energies ($E_\gamma^{\min}$) and a lower and upper limit for the excitation energy ($E_{\min}$, $E_{\max}$). The limits on the excitation-energy side are put to ensure that the spectra are dominated by decay from compound states ($E_{\min}$), and that the statistics is not too low ($E_{\max}$). On the γ-ray energy side the limit is set to exclude possible leftovers of higher-generation decay, which might not be correctly subtracted in the first-generation method (see Refs. [13,14] and references

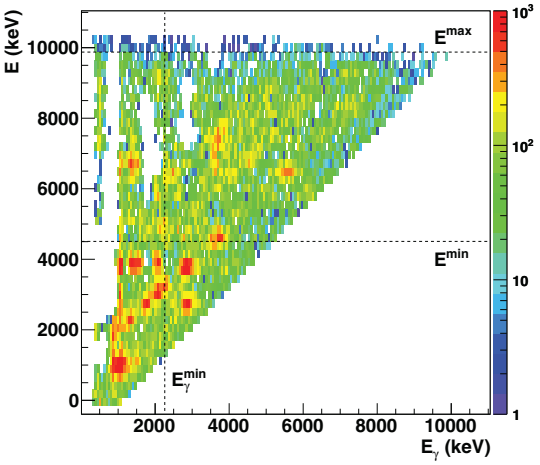

FIG. 3. (Color online) The first-generation spectra for each excitation-energy bin in ^{44}Ti. The dashed lines are limits set for the further analysis (see text).

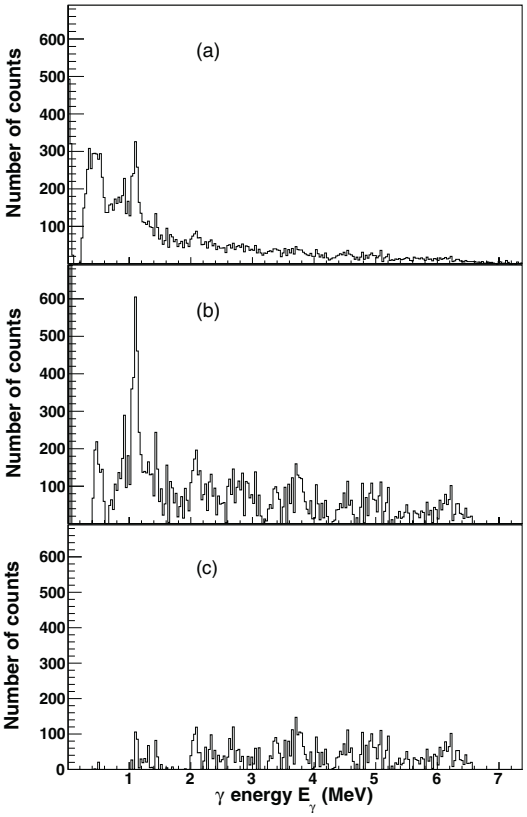

FIG. 4. Original (a), unfolded (b), and first-generation (c) γ-ray spectrum of ^{44}Ti for excitation energy $E = 6.1$ MeV.

therein for more details). In Fig. 4, the original, unfolded, and first-generation γ-ray spectrum of ^{44}Ti for excitation energy $E = 6.1$ MeV are displayed.

With the first-generation matrix properly prepared, an iterative procedure is applied to extract NLD and RSF from the primary γ-ray spectra. The method is based on the assumption that the reaction leaves the product nucleus in a compound state, which then subsequently decays in a manner that is independent of the way it was formed, that is, a statistical decay process [15]. This is a reasonable assumption for states in the quasicontinuum, where the typical lifetime of the states is of the order of 10^{-15} s, whereas the reaction time is $\approx 10^{-18}$ s. In addition, the configuration mixing of the levels is expected to be significant if the level spacing is comparable to the residual interaction [15]. This is normally fulfilled in the region of high level density.

If compound states are indeed populated, the γ decay from these states should be independent of the reaction used to reach them. In previous works (e.g., Ref. [16]) it has been demonstrated that the direct reactions (^{3}He,^{3}He$'$) and (^{3}He,α) into the same final nucleus do produce very similar decay cascades. Also, the extracted NLD and RSF were found to

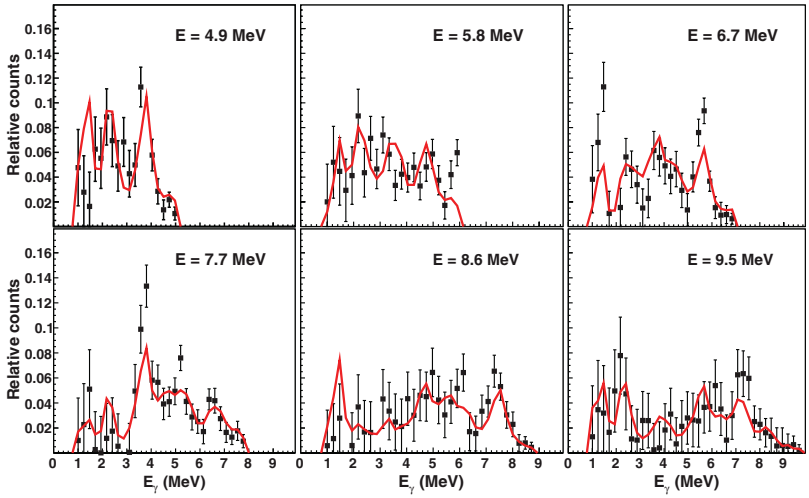

FIG. 5. (Color online) Comparison of experimental primary γ-ray spectra (solid squares) and the ones obtained from multiplying the extracted ρ and $\mathcal{T}$ functions (red line) for several excitation energies. The experimental and calculated spectra are shown for excitation-energy bins of 467 keV.

be equal within the expected fluctuations.[1] This indicates that even though a direct reaction such as (p, t) is used, compound states are likely to be populated at sufficiently high excitation energy [as mentioned already for the $E_{\rm min}$ limit set in the first-generation matrix $P(E, E_\gamma)$].

The ansatz for the iterative method is [13]

$$P(E, E_\gamma) \propto \rho(E_{\rm f})\mathcal{T}(E_\gamma), \tag{1}$$

meaning that the first-generation matrix $P(E, E_\gamma)$ is assumed to be separable into two vectors that give directly the functional form of the level density at the final excitation energy $E_{\rm f} = E - E_\gamma$, and the γ-ray transmission coefficient $\mathcal{T}$ for a given E_γ. This is done by minimizing

$$\chi^2 = \frac{1}{N_{\rm free}} \sum_{E=E^{\rm min}}^{E^{\rm max}} \sum_{E_\gamma=E_\gamma^{\rm min}}^{E} \left(\frac{P_{\rm th}(E, E_\gamma) - P(E, E_\gamma)}{\Delta P(E, E_\gamma)} \right)^2, \tag{2}$$

where $N_{\rm free}$ is the number of degrees of freedom, $\Delta P(E, E_\gamma)$ is the uncertainty in the experimental first-generation γ-ray matrix $P(E, E_\gamma)$, and the theoretical first-generation matrix is given by

$$P_{\rm th}(E, E_\gamma) = \frac{\rho(E - E_\gamma)\mathcal{T}(E_\gamma)}{\sum_{E_\gamma=E_\gamma^{\rm min}}^{E} \rho(E - E_\gamma)\mathcal{T}(E_\gamma)}. \tag{3}$$

Every point of the ρ and $\mathcal{T}$ functions is assumed to be an independent variable, so that the reduced χ^2 of Eq. (2) is minimized for every argument $E - E_\gamma$ and E_γ. Note that $\mathcal{T}$ is independent of excitation energy according to the Brink hypothesis [17]. If we had an excitation-energy dependent γ-ray transmission coefficient, $\mathcal{T} = \mathcal{T}(E, E_\gamma)$, it would, in principle, be impossible to disentangle the level density and the γ-ray transmission coefficient.

It is well known that the Brink hypothesis is violated when high temperatures and/or spins are involved in the nuclear reactions, as shown for giant dipole resonance (GDR) excitations in Ref. [18] and references therein. However, because both the temperature reached ($T \propto \sqrt{E_{\rm f}}$) and the spins populated ($J \sim 0 - 6\hbar$) are rather low for the experiment in this work, these dependencies are assumed to be of minor importance in the excitation-energy region of interest here.

To inspect how well the iterative procedure works, we have compared the experimental first-generation spectra for several excitation energies with the ones obtained by multiplying the extracted ρ and $\mathcal{T}$ functions. The result for a selection of primary γ-ray spectra is shown in Fig. 5. As can be seen, the agreement between the calculated and the experimental first-generation spectra are, in general, quite good, although there are local variations where the calculated spectra are not within the error bars of the experimental ones. These variations could well be attributable to large Porter-Thomas fluctuations [19], as there are relatively few levels in this nucleus.

The iterative procedure to obtain the level density and the γ-ray transmission coefficient uniquely determines the functional form of ρ and $\mathcal{T}$; however, identical fits to the experimental data is achieved with the transformations [13]

$$\tilde{\rho}(E - E_\gamma) = A \exp[\alpha(E - E_\gamma)]\, \rho(E - E_\gamma), \tag{4}$$

$$\tilde{\mathcal{T}}(E_\gamma) = B \exp(\alpha E_\gamma)\mathcal{T}(E_\gamma). \tag{5}$$

[1]Porter-Thomas fluctuations and statistical uncertainties must be taken into account.

Thus, to obtain the absolute normalization of the level density and γ-ray transmission coefficient, the transformation parameters A, α, and B must be determined independently.

III. NORMALIZATIONS AND MODELS FOR LEVEL DENSITY AND RADIATIVE STRENGTH FUNCTION

A. Level density

Usually, the level density $\rho(E_f)$ is normalized to known, discrete levels at low excitation energy and to the total level density at the neutron separation energy $\rho(S_n)$, which is deduced from neutron resonance spacings D_0 and/or D_1 (see, e.g., Ref. [20]). However, for the ^{44}Ti case, no neutron (or proton) resonance data are known because the target nuclei for the neutron and proton capture reactions are unstable. We are therefore left with only two types of experimental constraints, namely the known levels at low excitation energy and the observed first-generation spectra (which also depend on the γ-ray strength).

We have chosen two different approaches to normalize our data, and, of those, to estimate the sensitivity on our results to this normalization procedure: (i) apply theoretical level densities based on microscopic calculations, and (ii) use a standard closed-form formula with global parameters. For the first approach, we have used recent calculations of Goriely, Hilaire, and Koning [21] (hereafter labeled GHK). For the second approach, we have applied the constant-temperature (CT) formula [22]:

$$\rho_{\mathrm{CT}}(E) = \frac{1}{T}\exp\left(\frac{E-E_0}{T}\right), \tag{6}$$

where the nuclear temperature $T = 1.50$ MeV and the energy shift $E_0 = -0.08$ MeV are taken from the global parametrization of Refs. [23,24]. The level-density data normalized to these two approaches are shown in Fig. 6.

We observe that our data follow closely the known, discrete levels [25] at low excitation energy, and especially in the region $2.4 < E < 5.2$ MeV. This is gratifying, as it implies that the Oslo method does indeed give reasonable results for the level density. We also see that there is a decrease in the level density for $4.0 < E < 5.2$ MeV and an abrupt increase for $5.8 < E < 6.2$ MeV. These structures are not well described by any of the models used for normalization. They might be attributable to shell effects and/or α-clustering effects (because ^{44}Ti is an $N = Z$ nucleus). An increase in the level density could also indicate the breaking of a nucleon Cooper pair and/or the crossing of a shell gap.

We note that both the ground state and the 0^+ state at $E = 1.9$ MeV are not very pronounced in Fig. 6. Also, we see that there is less direct decay to the ground state and the excited 0^+ state compared to the 2^+ state at 1083 keV and the 4^+ state at 2454 keV, especially at higher excitation energies (see Fig. 3). This could imply that there are relatively few spin-1 states populated in the (p, t) reaction (assuming that dipole radiation is dominant in this region). This is not surprising because the spin distribution is expected to have a maximum for $J = 3$–4.

We see that the resolution on the level density is rather poor at low excitation energies, roughly 600 keV for the first excited 2^+ state. This may be explained by the fact that the level density in this region is mainly determined by decay involving high-energy γ rays, which have a resolution of up to ≈300 keV (similar to the triton-energy resolution). As a consequence, the resolution of the level density gets better and better for increasing excitation energy. In addition, the rather large amount of other Ti isotopes in the target may give a smoothing effect on the extracted quantities (both the NLD and RSF).

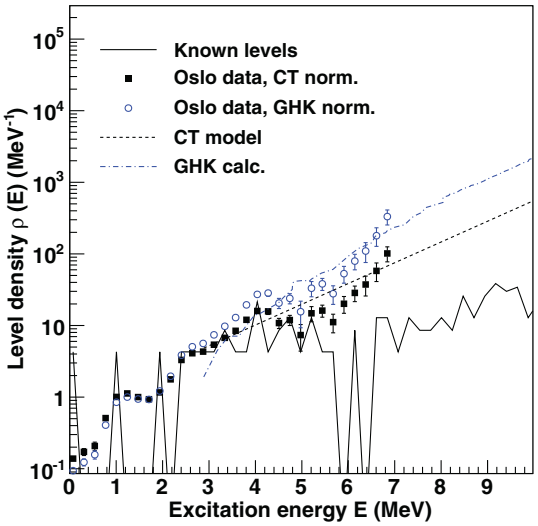

FIG. 6. (Color online) Experimental data points (solid squares) normalized to the CT model (dashed line) and data points (blue, open circles) normalized to the calculation of GHK (dash-dotted line). The black, solid line represents the known levels taken from Ref. [25].

B. Radiative strength function

Because there are no experimental data on neither the level spacing D nor the total, average radiative width for s-wave resonances $\langle\Gamma_{\gamma 0}\rangle$ for ^{44}Ti, we must find the absolute normalization parameter B of the RSF by other means. To have a rough approximation of the absolute strength, we have looked at experimental values of $\langle\Gamma_{\gamma 0}\rangle$ for other Ti isotopes found in Ref. [26] (see Fig. 7). From these values, the educated guess of $\langle\Gamma_{\gamma 0}\rangle = 1200(600)$ meV seems to be reasonable for ^{44}Ti. The RSFs of ^{44}Ti for the two choices of level-density normalization are shown in Fig. 8. Also, the upper and lower limits are indicated, corresponding to $\langle\Gamma_{\gamma 0}\rangle = 1800$ meV for the CT normalization and $\langle\Gamma_{\gamma 0}\rangle = 600$ meV for the GHK normalization, respectively.

From Fig. 8, it is seen that for $E_\gamma > 4$ MeV, the RSF of ^{44}Ti seems to reach a relatively smooth behavior with increasing strength as a function of E_γ. Naturally, as seen from Eq. (5), the slope varies depending on the normalization chosen for the level density. For energies below $E_\gamma \approx 4$ MeV, we observe on average a slight increase in strength for decreasing γ-ray energy. However, we see that the data in this region display

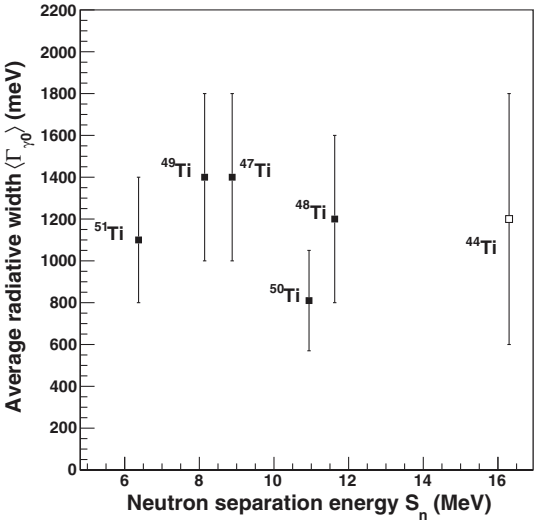

FIG. 7. Experimental average radiative width (solid squares) for $^{47-51}$Ti as a function of neutron separation energy and estimated width for ^{44}Ti (open square).

quite large variations, which could be attributable to Porter-Thomas fluctuations [19].

A low-energy increase in the RSF data has been seen previously in several light and medium-mass nuclei with the Oslo method [27–31], with the two-step cascade method following neutron capture [27], and recently also in proton capture [32]. However, for ^{44}Ti, the increase at low energies is not as strong as in, for example, ^{56,57}Fe [27].

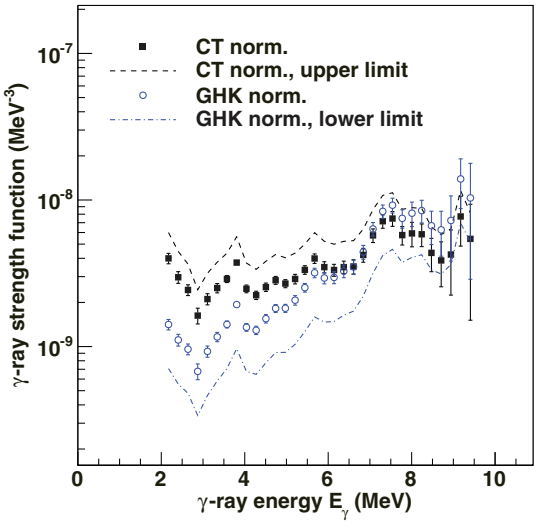

FIG. 8. (Color online) Normalized RSFs for the two normalizations of the level density. The dashed line is the upper limit for the CT normalization, while the dash-dotted line is the lower limit for the GHK normalization.

As of today, it is not clear whether the low-energy increase is attributable to some sort of collective decay mode(s) or if it is an effect of other structural effects in these nuclei. An analysis of simulated data using the DICEBOX code [33] has demonstrated that for light nuclei, the spin distribution of the initial populated levels may have a considerable influence on the possible decay paths from these levels [14]. This seems to be attributable to a combination of several factors: (i) the low level density in light nuclei at low excitation energy, (ii) restrictions on the possible populated spins of the initial levels, (iii) the dominance of dipole radiation from highly excited levels, and (iv) a rather large asymmetric parity distribution up to rather high excitation energies. As is shown in Ref. [14], these factors may lead to a significant increase in the extracted RSF for low γ-ray energies compared to the input RSF function used to generate the γ-ray spectra. It is not unlikely that a similar effect may be present in ^{44}Ti as well.

C. Models for the radiative strength function

In general, the γ decay in quasicontinuum is expected to be dominated by electric dipole radiations. Also, there is experimental evidence that a giant magnetic dipole resonance (also known as the magnetic spin-flip resonance) is present in several light and medium-mass nuclei (see, e.g., Ref. [34]).

We have applied the commonly used generalized Lorentzian (GLO) expression [35,36] for the $E1$ strength. This model is given by Ref. [36]

$$f_{\mathrm{GLO}}(E_\gamma, T_f) = \frac{1}{3\pi^2\hbar^2c^2}\sigma_{E1}\Gamma_{E1} \times\left[\frac{E_\gamma\Gamma(E_\gamma,T_f)}{\left(E_\gamma^2-E_{E1}^2\right)^2+E_\gamma^2\Gamma(E_\gamma,T_f)^2} + 0.7\frac{\Gamma(E_\gamma=0,T_f)}{E_{E1}^3}\right], \quad (7)$$

where the Lorentzian parameters Γ_{E1}, E_{E1}, and σ_{E1} correspond to the width, centroid energy, and peak cross section of the giant electric dipole resonance (GDR), respectively. We have made use of the parametrization of RIPL-2 [26] to estimate the GDR parameters as these are unknown experimentally. Owing to the dynamic ground-state deformation of ^{44}Ti ($\beta_2 = 0.27$ [26]), the GDR is assumed to be split in two components and thus two sets of GDR parameters are applied (see Table I). In addition, we have assumed a constant temperature T_f of the final states in accordance with the Brink hypothesis [17].

To account for the small increase in strength at low energies, we have added a Lorentzian resonance of the form

$$f_{\mathrm{up}}(E_\gamma) = \frac{1}{3\pi^2\hbar^2c^2}\frac{\sigma_{\mathrm{up}}E_\gamma\Gamma_{\mathrm{up}}^2}{\left(E_\gamma^2-E_{\mathrm{up}}^2\right)^2+E_\gamma^2\Gamma_{\mathrm{up}}^2}, \quad (8)$$

with centroid energy $E_{\mathrm{up}} = 1.9$ MeV, width $\Gamma_{\mathrm{up}} = 1.3$ MeV, and a peak cross section σ_{up} that will vary according to which NLD model that has been used for normalization. Such a shape of the low-energy increase seems to be in accordance with data

TABLE I. Parameters used for the RSF models.

Model	$E_{E1,1}$ (MeV)	$\sigma_{E1,1}$ (mb)	$\Gamma_{E1,1}$ (MeV)	$E_{E1,2}$ (MeV)	$\sigma_{E1,2}$ (mb)	$\Gamma_{E1,2}$ (MeV)	T_f (MeV)	E_{M1} (MeV)	σ_{M1} (mb)	Γ_{M1} (MeV)	$E_{\rm up}$ (MeV)	$\sigma_{\rm up}$ (mb)	$\Gamma_{\rm up}$ (MeV)
CT + GLO	17.23	43.16	5.98	21.58	21.54	9.19	0.50	11.6	0.8	4.0	1.9	0.060	1.3
CT + GLO, upper limit	17.23	43.16	5.98	21.58	21.54	9.19	0.80	11.6	0.9	4.0	1.9	0.070	1.3
GHK + GLO	17.23	43.16	5.98	21.58	21.54	9.19	0.40	11.6	0.7	4.0	1.9	0.015	1.3
GHK + GLO, lower limit	17.23	43.16	5.98	21.58	21.54	9.19	0.15	11.6	0.3	4.0	1.9	0.010	1.3

and model descriptions in Refs. [37,38] for the Mo nuclei and was used also in Ref. [39]. The constant temperature T_f is slightly varied for the two models to give the best fit to the data. All parameters used are given in Table I.

The lower and upper limit of the absolute normalization will necessarily give slightly different parameters to get the best fit to the data. These parameters are also given in Table I.

Another frequently used model for $E1$ strength is the standard Lorentzian (the Brink-Axel model, see Ref. [26] and references therein). The expression reads

$$f_{\rm SLO}(E_\gamma) = \frac{1}{3\pi^2\hbar^2c^2}\frac{\sigma_{E1}E_\gamma\Gamma_{E1}^2}{\left(E_\gamma^2 - E_{E1}^2\right)^2 + E_\gamma^2\Gamma_{E1}^2}. \quad (9)$$

This model is independent of excitation energy, in accordance with our assumption behind Eq. (1). However, as described in Ref. [26], this model is known to generally overestimate the value of $\langle\Gamma_{\gamma 0}\rangle$ and neutron-capture cross sections.

For the magnetic transitions, a standard Lorentzian as recommended by the RIPL-2 library [26] and shown in Fig. 9 is adopted (see Table I for the corresponding parameters).

The resulting models and the extracted data for the two adopted NLD normalizations are shown in Fig. 9 (the models corresponding to the best fit for the lower and upper normalization limits are not shown). We see from Fig. 9 that the shape of the SLO model does not fit the extracted RSF very well; in particular, the low-energy part is very different in shape. The enhancement of the RSF data at low γ-ray energies may be explained by the spin distribution of the initial levels as described previously.

D. Temperature dependence of the strength function

As discussed already, we rely on the Brink hypothesis when extracting the NLD and RSF. We would like to investigate if this hypothesis is reasonable, and we have therefore extracted the RSF for two different excitation-energy regions, $4.5 \leqslant E \leqslant 7.1$ MeV and $7.3 \leqslant E \leqslant 9.9$ MeV (see Fig. 10 for the result using the CT normalization). We observe that there are rather large, local fluctuations, for example, at $E_\gamma \approx 5.5$ MeV, which makes it hard to draw any firm conclusion whether the extracted RSF is dependent on excitation energy or not. As already mentioned, we expect large differences owing to Porter-Thomas fluctuations in the decay strength of this nucleus. However, the gross features seem to be quite similar for the two excitation-energy ranges.

To get a better understanding on the possible temperature dependence, we have also used the standard GLO model with a varying temperature corresponding to the accessible final excitation energies of the two ranges. The temperature is estimated by $T_f \propto \sqrt{E_f}$, and the models displayed in Fig. 10 represent the average RSF within the three excitation-energy regions $4.5 \leqslant E \leqslant 7.1$ MeV, $7.3 \leqslant E \leqslant 9.9$ MeV, and $4.5 \leqslant E \leqslant 9.9$ MeV. The maximum final temperature reached is in the range 0.50–1.14 MeV for initial excitation energies between 4.5 and 9.9 MeV and with $E_\gamma^{\rm min} = 2.2$ MeV.

We observe that for γ energies between 2.2 and 5.2 MeV, the upper range can give more than a factor of 2 larger γ

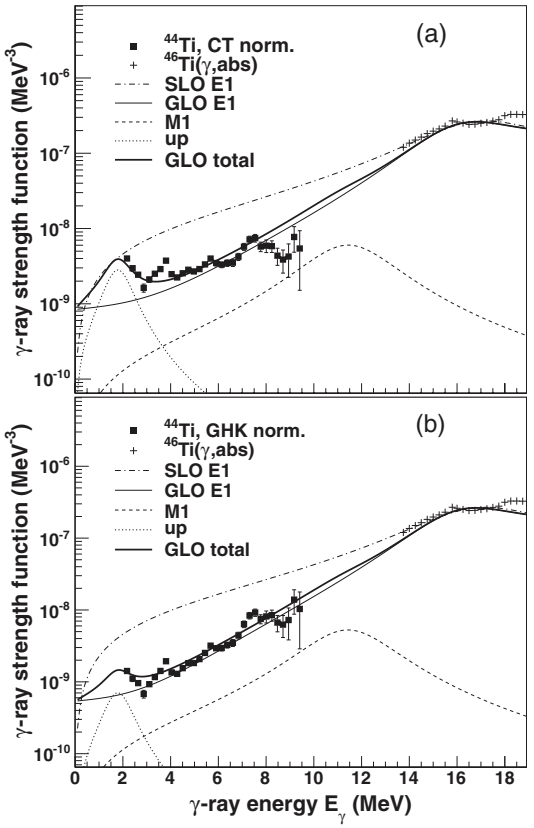

FIG. 9. Radiative strength functions and fitted models for (a) the CT and (b) the GHK normalization. Note that the SLO model has not been fitted to the data.

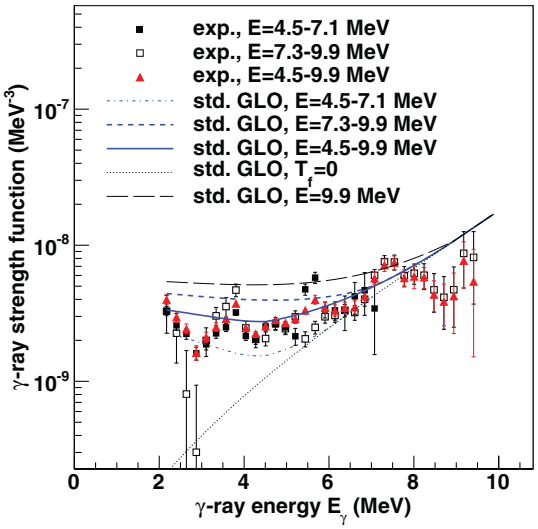

FIG. 10. (Color online) Radiative strength functions extracted for two different excitation-energy regions as compared to the one from the total excitation-energy region under consideration (all cases are normalized to the CT level density). The standard GLO model is also shown for these ranges of excitation energy and the extreme cases $T_f = 0$ and $E = 9.9$ MeV.

strength in the GLO model than the lower range. The largest experimental fluctuations are also of the order of a factor two, but on average, the experimental data seem not to have such a strong dependence on the final excitation energy as the standard GLO model would imply.

Finally, we have calculated the GLO model for the direct decay to the ground state ($T_f = 0$ MeV) and for the highest temperatures reached, namely for initial excitation energy $E = 9.9$ MeV. These cases are also displayed in Fig. 10. It is clear that the zero-temperature calculation is not similar to the experimental data below $E_\gamma \approx 6$ MeV. In fact, the experimental data lie in between the two extreme cases. As argued above, the overall shape of the RSF seem to be rather similar for the two excitation-energy ranges. Thus, it is probably quite reasonable to apply a constant temperature in the GLO model in accordance with the Brink hypothesis. We note, however, that the GLO model averaged over the total excitation-energy range covered (blue solid line in Fig. 10) agrees rather well with the average shape of the experimental data.

IV. REPRODUCTION OF EXPERIMENTAL PRIMARY γ-RAY SPECTRA

As described in the previous section, both the NLD and the RSF deduced from the present experiment are affected by severe uncertainties associated with the normalization procedure that in the case of ^{44}Ti cannot be reliably constrained by additional experimental data. For this reason, the different NLD and RSF models are now directly tested on the primary γ-ray spectra, which in turn correspond to the fundamental quantity entering the description of the radiative decay in reaction models.

There are 24 experimental spectra for excitation energies $4.5 \leqslant E \leqslant 9.9$ MeV with bin size 233.4 keV. Owing to the poor statistics, we have compared the average of two bins as in Fig. 5. For the level density, we have applied the known levels for $E < 3.7$ MeV and either the CT model or the GHK calculation above this energy. The calculated spectra are scaled to get the best possible agreement with the experimental spectra, which are normalized such that $\sum_{E_\gamma=E_\gamma^{\min}}^{E} P(E, E_\gamma) = 1$.

We have also calculated the primary γ spectra using the standard GLO model with a variable temperature in combination with the two level density models. For each initial excitation energy ($4.5 \leqslant E \leqslant 9.9$ MeV), we have used the GLO model with $T_f \propto \sqrt{E_f}$ and made an average of all these RSFs for the whole excitation-energy region that is used for the analysis.

Finally, we have applied the SLO model in combination with the two NLD models.

The six model combinations shown in Figs. 11 and 12 thus correspond to the following:

(i) input 1, the CT level density and the fitted GLO model with constant temperature;
(ii) input 2, the GHK level density and the fitted GLO model with constant temperature;
(iii) input 3, the CT level density and standard GLO model averaged over the experimental excitation-energy range (blue, solid line in Fig. 10);
(iv) input 4, GHK level density and standard GLO model averaged over the experimental excitation-energy range (blue, solid line in Fig. 10);
(v) input 5, the CT level density and the SLO model;
(vi) input 6, the GHK level density and the SLO model.

We find that for the lower excitation energies ($E \leqslant 7.0$ MeV), all the input models give a rather good reproduction of the spectra, and also they give relatively similar results. However, for the higher excitation energies ($7.4 \leqslant E \leqslant 9.8$ MeV), there are clear deviations for the different inputs, and input 4 gives a significantly worse fit than the others. This is not so surprising, considering that the slope of the standard GLO model is very different from the RSF model fitted to our data using the GHK level density. It is seen in Fig. 12 that this mismatch in slope leads to a wrong overall shape of the primary spectra (overestimating the low-energy part and underestimating the high-energy part). The models that are consistent in slope behave much better.

In general, for the high-energy region, input 2 and input 3 give the best reproduction of the experimental spectra out of the six model combinations. The SLO model gives also rather good results, in particular in combination with the GHK level density. This could be an indication that the overall shape of this model might be correct, although the absolute value is probably too large (as seen in Fig. 9). However, in combination with the CT level density the spectra calculated with this model underestimate the intensity of the low-energy γ rays compared to the measured ones.

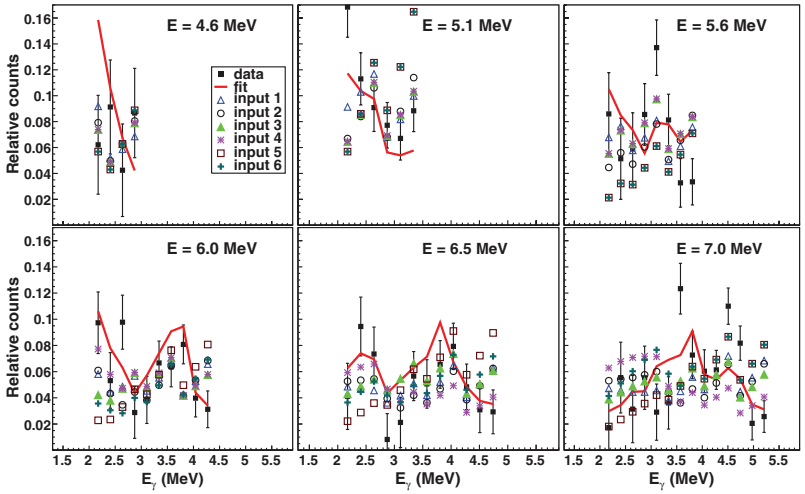

FIG. 11. (Color online) Experimental primary γ spectra (solid squares) and those obtained from multiplying the extracted ρ and $\mathcal{T}$ functions (red line) for $4.6 \leqslant E \leqslant 7.0$ MeV. These are compared with calculated spectra using the six inputs as described in the text. The experimental and calculated spectra are given for excitation-energy bins of 466.8 keV.

Naturally, using the extracted ρ and $\mathcal{T}$ data points give a much better fit than any model, as structures especially in the level density are lost when using the smooth models.

V. CAPTURE CROSS SECTION AND MAXWELLIAN-AVERAGED RATE

The model combinations described in Sec. IV can further be applied for estimating the ^{40}Ca$(\alpha,\gamma)^{44}$Ti cross section and the corresponding reaction rate. We have used the code TALYS [24] for the cross-section and reaction-rate calculations. In all calculations we have used the α optical-model potential (OMP) of McFadden and Satchler [40]. We have also tested other α-OMPs such as the one developed by Demetriou, Grama, and Goriely [41]; however, it turns out that in this case, the results are rather insensitive to the choice of α-OMP.

The model sets applied for the cross-section and reaction-rate calculations are as follows:

(i) input 1, the CT level density and the corresponding fitted GLO model;

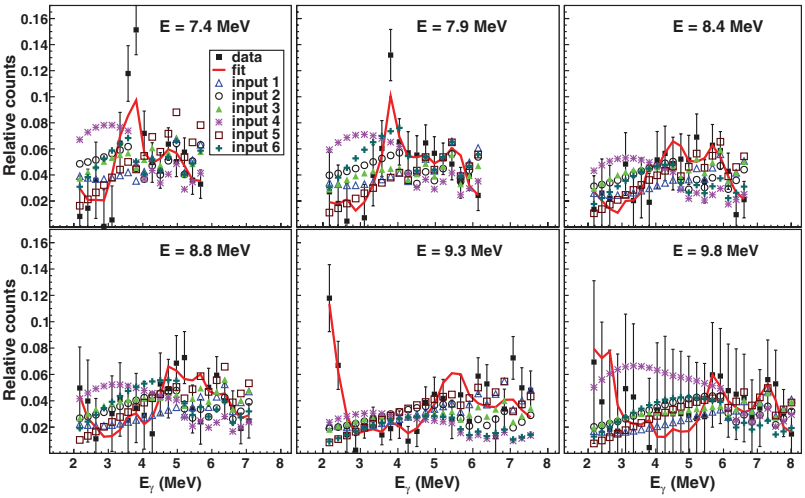

FIG. 12. (Color online) Same as Fig. 11 for $7.4 \leqslant E \leqslant 9.8$ MeV.

(ii) input 2, the GHK level density and the corresponding fitted GLO model;
(iii) input 5, the CT level density and the SLO model;
(iv) input 6, the GHK level density and the SLO model;
(v) input 7, the CT level density and the standard GLO model;
(vi) input 8, the GHK level density and the standard GLO model;
(vii) input 9, the CT level density and the corresponding fitted GLO model for the upper normalization limit ($\langle\Gamma_{\gamma 0}\rangle = 1800$ meV);
(viii) input 10, the GHK level density and the corresponding fitted GLO model for the lower normalization limit ($\langle\Gamma_{\gamma 0}\rangle = 600$ meV).

For the standard GLO model, we have followed the prescription used in TALYS, where the temperature of the final states is calculated from the relation [26]

$$T_f = \sqrt{(E_i - \Delta - E_\gamma)/a}. \tag{10}$$

Here E_i is the initial excitation energy in the compound nucleus, Δ is a pairing correction, and a is the level density parameter. There is thus a specific GLO RSF for each initial excitation energy (no averaging over a large excitation-energy window as was done with inputs 3 and 4 in Sec. IV).

The Maxwellian-averaged astrophysical reaction rate $N_A\langle\sigma v\rangle(T)$ for a temperature T is given by

$$N_A\langle\sigma v\rangle(T) = \left(\frac{8}{\pi m}\right)^{1/2} \frac{N_A}{(kT)^{3/2}G(T)} \times \int_0^\infty \sum_\mu \frac{(2I^\mu + 1)}{(2I^0 + 1)}\sigma^\mu(E)E \times \exp\left[-\frac{\left(E + E_x^\mu\right)}{kT}\right] dE, \tag{11}$$

where m is the reduced mass of the initial system of projectile (here the α particle) and target nucleus (here ^{40}Ca), k is the Boltzmann constant, N_A is Avogadro's number, E is the relative energy of the target and projectile, I^μ, E_x^μ are the spin and excitation energy for the excited states labeled μ, and σ^μ is the reaction cross section. Further, the temperature-dependent, normalized partition function $G(T)$ reads

$$G(T) = \sum_\mu (2I^\mu + 1)/(2I^0 + 1)\exp\left(-E_x^\mu/kT\right). \tag{12}$$

See the TALYS documentation for more details [24].

For the above expressions, local thermodynamic equilibrium is assumed in the astrophysical environment, so that the energies of both the targets and the projectiles, as well as their relative energies E, obey Maxwell-Boltzmann distributions corresponding to the temperature T at that location. Also, the relative populations of the various nuclear levels with spin and excitation energy I^μ, E_x^μ obey a Maxwell-Boltzmann distribution.

A. Uncertainties in the calculations

The key ingredients in the rate calculations (NLD, RSF, and α-OMP) all contribute to the uncertainties but in different temperature regions. By varying the α-OMP, the rate will change most at low temperatures (below $\approx 1.5 \times 10^9$ K), while the NLD and RSF both have a significant impact on the rate at higher temperatures (above $\approx 1.5 \times 10^9$ K).

The ^{40}Ca(α,γ) reaction only populates states with total isospin zero in ^{44}Ti, and dipole transitions with no change in total isospin are suppressed in self-conjugate $N = Z$ nuclei [42]. Because complete isospin mixing is assumed in the determination of the RSF, a corrective factor must be included before applying the extracted RSFs in the cross section and reaction rate calculations. For α captures, a standard prescription is to divide the RSF by a constant factor $f_{\rm iso}$ of typically 5 to 8 [6,42], giving a reduced RSF f' of $f' = f/f_{\rm iso}$.

However, it is not obvious how the value of this correction factor should be determined, because it is related to the degree of isospin mixing (for a large degree of mixing the correction factor should be small and vice versa). Also, high-energy γ rays decay to low-lying states, where the isospin mixing might be small, while low-energy γ rays decay in the quasicontinuum, where one expects a large degree of mixing. Therefore, one could, in principle, expect that $f_{\rm iso}$ would vary as a function of γ energy. To estimate such a function is, however, a very complicated task and beyond the scope of the present work. We therefore assume a constant $f_{\rm iso}$, although this is probably quite crude.

Another source of uncertainty is the value of $\langle\Gamma_{\gamma 0}\rangle$. Because this value is not known experimentally, the uncertainty in this quantity is correlated to the uncertainty in $f_{\rm iso}$. This is because one can obtain basically the same cross section and reaction rate for a range of $\langle\Gamma_{\gamma 0}\rangle$ values by adjusting $f_{\rm iso}$ correspondingly (a small value of $\langle\Gamma_{\gamma 0}\rangle$ in combination with a small $f_{\rm iso}$ and vice versa).

We have calculated the integral cross section of the $(\alpha,\gamma)^{44}$Ti reaction for incoming α energies between 2.1 and 4.2 MeV. This corresponds to excitation energies in ^{44}Ti in the range $E = 7.2$–9.3 MeV, which is the most relevant region for astrophysics. In the calculations, we have adopted a constant $f_{\rm iso} = 5$, and we have also tested a larger correction factor of $f_{\rm iso} = 8$. In addition, we have considered the assumed uncertainty of 50% in the estimated value of $\langle\Gamma_{\gamma 0}\rangle$ combined with the uncertainty in slope (either the CT or the GHK level density, which represent the extremes in slope of the extracted RSF). The results for all the considered inputs are given in Table II.

We see from Table II that changing the isospin correction factor leads to a change in the calculated cross section of typically 2–3 μb, except for the SLO model where different values of $f_{\rm iso}$ give up to ≈ 5 μb change in $\sigma_{\rm ave}$. The uncertainty in $\langle\Gamma_{\gamma 0}\rangle$ and slope will also give a change in $\sigma_{\rm ave}$ of up to ≈ 5 μb.

We therefore conclude that the absolute value of the reaction cross section of the α capture on ^{40}Ca is highly uncertain. Also, intrinsically very different models of the level density and the RSF may yield practically the same cross section by adjusting $f_{\rm iso}$ and/or $\langle\Gamma_{\gamma 0}\rangle$. Thus, we find that although our data may put

TABLE II. Integral cross sections for the various model combinations.

Model combination	σ_{ave} (μb)	
	$f_{iso} = 5$	$f_{iso} = 8$
Input 1	7.1	4.9
Input 2	6.9	4.9
Input 5	17.8	13.2
Input 6	19.2	14.5
Input 7	5.6	3.8
Input 8	6.9	4.9
Input 9	9.7	6.9
Input 10	5.0	3.4

a constraint on the functional form of the NLD and RSF, and in particular the correlated slope of the two quantities, other data are needed to further constrain the cross section and reaction rate. This is addressed in the following.

B. Comparison with other data

We have compared our calculations with two recent data sets, one from Nassar *et al.* [6] and one from Vockenhuber *et al.* [1]. In the following discussion we have used $f_{iso} = 5$, unless stated otherwise.

Nassar *et al.* [6] performed an integral measurement on the ^{40}Ca$(\alpha,\gamma)^{44}$Ti cross section corresponding to an energy window of $E_\alpha = 2.1$–4.2 MeV for the incoming α particles. The originally estimated energy-averaged cross section was $\sigma_{ave}^{exp} = 8.0(11)$ μb; however, it was pointed out by Vockenhuber *et al.* [1] that, owing to an overestimate of the ^{40}Ca stopping power, the cross section should be reduced by about 10%: $\sigma_{ave}^{exp} \simeq 7.0(10)$ μb.

Using the model combinations input 1 and input 2, we get $\sigma_{ave} = 7.1$ and 6.9 μb for the CT and GHK normalization, respectively (see Table II). This is in excellent agreement with the Nassar results. Note that if we exclude the low-energy enhancement in inputs 1 and 2, σ_{ave} yields 6.6 and 6.7 μb for the CT and GHK normalization, respectively. Thus, the effect of the small low-energy enhancement is not significant compared to neither the current experimental uncertainty on the integral cross section nor the uncertainties in the calculations owing to the isospin suppression factor and the unknown absolute normalization of the RSF.

Further, if we apply the standard GLO model in the calculations, we obtain $\sigma_{ave} = 5.6$ and 6.9 μb using the CT and GHK level density (input 7 and input 8), respectively. The former is slightly smaller than the lower experimental limit on σ_{ave}^{exp}. The latter agrees very well with the Nassar data; however, we noted in Sec. IV that the GHK level density in combination with the averaged, standard GLO did not reproduce our experimental spectra above $E \approx 7$ MeV. Therefore, input 8 is probably not correct.

The calculations with the SLO model are many standard deviations too large compared to the Nassar data, even for $f_{iso} = 8$. Thus, we do not use inputs 5 and 6 further. We also see that the upper normalization limit, input 9, is only acceptable for $f_{iso} = 8$. However, the lower normalization limit (input 10) seems to be a bit too low for $f_{iso} = 5$ and even more so for $f_{iso} = 8$.

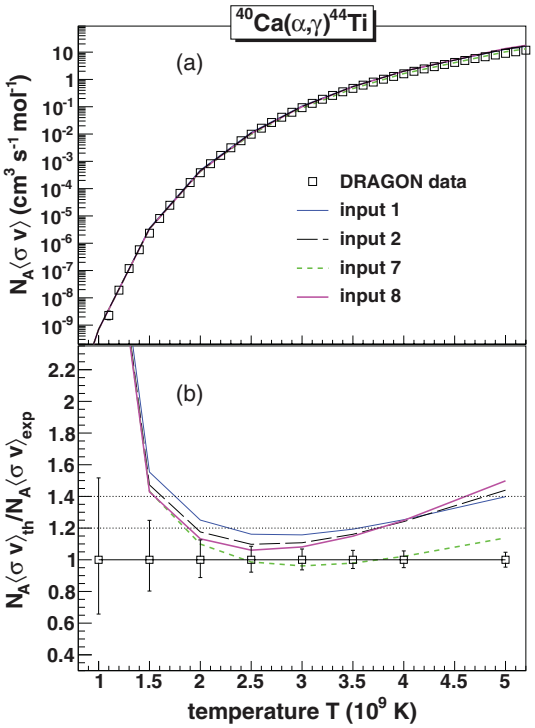

FIG. 13. (Color online) (a) Data on the Maxwellian-averaged reaction rate for the ^{40}Ca(α,γ) reaction from Ref. [1] are compared to calculations with inputs 1, 2, 7, and 8. (b) Ratio of the calculated reaction rates and experimental data. The upper dotted line indicates a 40% deviation from the experimental data, while the lower dotted line indicates a 20% deviation.

With the inputs 1, 2, 7, and 8, we have estimated the reaction rate according to Eq. (10) and compared to the DRAGON data of Vockenhuber *et al.* [1]. The results are shown in the top panel of Fig. 13. As seen here, all these four inputs give a reasonable reproduction of the measured rates, and they can hardly be distinguished from each other over the entire temperature range. We also note that the cross-section range spans over 10 orders of magnitude, and it is quite impressive how well the calculated rates follow the overall functional form of the data.

However, we observe that some models overestimate the rate somewhat, especially at higher temperatures. Now, the experimental rate could be too low for temperatures above $T_9 \approx 4$ MeV because of missing resonances (only six resonances with measured resonance strengths are known for excitation energies at and above 9.3 MeV [1]). We note, however, that the rate at these high temperatures is not important for the final ^{44}Ti mass yield [1].

The combination of CT level density and standard GLO (input 7) gives a better reproduction of the DRAGON data at high temperatures than the others. However, this combination gave a too-small average cross section as compared to the Nassar result. We therefore confirm the slight inconsistency between the two measurements, as discussed in Ref. [1]. As already mentioned, we observed that the combination of the GHK level density and the averaged, standard GLO model (input 4) was not able to give a reasonable description of our primary γ spectra for initial excitation energies above $\approx$7 MeV. Therefore, input 8 cannot be recommended on the basis of the present data.

To get a clearer picture of the deviation of the calculated rates vs the DRAGON data, the ratio of the calculated and experimental rate is shown in the bottom panel of Fig. 13. Here it is seen that input 7 gives the best fit to the DRAGON data for all temperatures above $T_9 \approx 1.7$ ($T_9 = 10^9$ K). The large overestimate of the rate for $T_9 < 1.5$ is common for all model predictions and is attributable to problems with the α OMP at very low energies.

It is seen from the lower panel in Fig. 13 that all the calculated rates lie within 40% of the DRAGON data for $1.8 \leqslant T_9 \leqslant 4.5$, and for the 20% upper limit in the range $2.2 \leqslant T_9 \leqslant 3.7$. However, only input 7 (CT level density and standard GLO) is within the experimental error bars for $1.8 \leqslant T_9 \leqslant 4.5$.

It should be noted that by using the lower normalization limit for the RSF (blue, dashed-dotted line in Fig. 8), an excellent agreement with the DRAGON data is obtained. However, as stated previously, a good reproduction of the DRAGON data implies a too low integral cross section (in this case $\sigma_{\text{ave}} = 5.0$ μb) as compared to the Nassar data. However, using the upper normalization limit for the RSF (dashed line in Fig. 8), it is necessary to use the larger value of $f_{\text{iso}} = 8$ to obtain a reasonable agreement with the data (see Table II).

To summarize, we have found that the model combinations input 1, input 2, and input 8 are in excellent agreement with the Nassar cross-section measurement. However, input 8 (GHK level density and standard GLO) is not in accordance with our primary γ spectra for the relevant excitation-energy region ($E = 7.2$–9.3 MeV) and should therefore not be used. The DRAGON data are best described with input 7 (CT level density and standard GLO) and the lower normalization limit of our RSF data (input 10). We also see that the small enhancement in the RSF at low E_γ is not very important for the integrated cross section or the rate, as it gives a contribution of maximum 0.5 μb.

VI. SUMMARY

Particle-γ coincidence data of the ^{46}Ti$(p, t\gamma)^{44}$Ti reaction have been measured at OCL. By use of the Oslo method, primary γ-ray spectra have been extracted for initial excitation energies in the range $E = 4.5$–9.9 MeV. From these spectra, the functional form of the level density and the RSF have been determined.

We have shown that a consistent normalization of the NLD and RSF is necessary to obtain a reasonable reproduction of the primary spectra. Also, the RSF seems to be independent of excitation energy and thus of the temperature, in accordance with the Brink hypothesis. However, the GLO model with a variable temperature, and averaged over the excitation-energy region, gives a rather good description of the overall shape of our RSF data when normalized to the CT level density.

Using input models consistent with our data gives an excellent reproduction of the Nassar integral measurement of the ^{40}Ca(α,γ) reaction cross section. Also the DRAGON data of the reaction rate are rather well reproduced. However, we note that there is a discrepancy between the two datasets, so that it is not possible to use one model combination to obtain optimal agreement for both measurements simultaneously. Nevertheless, on the basis of our present data, it is clear that certain model combinations are not acceptable, although they might give reasonable results compared to the cross-section data.

ACKNOWLEDGMENTS

Funding of this research from the Research Council of Norway, project Grant No. 180663, is gratefully acknowledged. We would like to give special thanks to E. A. Olsen and J. Wikne for providing excellent experimental conditions. A.C.L. would like to thank M. Hjort-Jensen and M. Krtička for inspiring and enlightening discussions.

[1] C. Vockenhuber *et al.*, Phys. Rev. C **76**, 035801 (2007).
[2] M. Renaud *et al.*, Astrophys. J. **647**, L41 (2006).
[3] A. F. Iyudin *et al.*, Astron. Astrophysics **284**, L1 (1994).
[4] S. E. Woosley and T. A. Weaver, Astrophys. J. Suppl. Ser. **101**, 181 (1995).
[5] F.-K. Thielemann, K. Nomoto, and M. Hashimoto, Astrophys. J. **460**, 408 (1996).
[6] H. Nassar *et al.*, Phys. Rev. Lett. **96**, 041102 (2006).
[7] Data extracted from the Q-value calculator at the National Nuclear Data Center database [http://www.nndc.bnl.gov/qcalc/].
[8] M. Guttormsen, A. Ataç, G. Løvhøiden, S. Messelt, T. Ramsøy, J. Rekstad, T. F. Thorsteinsen, T. S. Tveter, and Z. Zelazny, Phys. Scr., T **32**, 54 (1990).
[9] N. U. H. Syed *et al.*, Phys. Rev. C **80**, 044309 (2009).
[10] J. Rapaport, J. B. Ball, R. L. Auble, T. A. Belote, and W. E. Dorenbusch, Phys. Rev. C **5**, 453 (1972).
[11] M. Guttormsen, T. S. Tveter, L. Bergholt, F. Ingebretsen, and J. Rekstad, Nucl. Instrum. Methods Phys. Res. A **374**, 371 (1996).
[12] M. Guttormsen, T. Ramsøy, and J. Rekstad, Nucl. Instrum. Methods Phys. Res. A **255**, 518 (1987).
[13] A. Schiller, L. Bergholt, M. Guttormsen, E. Melby, J. Rekstad, and S. Siem, Nucl. Instrum. Methods Phys. Res. A **447**, 498 (2000).
[14] A. C. Larsen *et al.*, Phys. Rev. C **83**, 034315 (2011).
[15] A. Bohr and B. Mottelson, *Nuclear Structure*, Vol. I. (Benjamin, New York, 1969).
[16] R. Chankova *et al.*, Phys. Rev. C **73**, 034311 (2006).

[17] D. M. Brink, Ph.D. thesis, Oxford University, 1955.
[18] A. Schiller and M. Thoennessen, At. Data Nucl. Data Tables **93**, 549 (2007).
[19] C. E. Porter and R. G. Thomas, Phys. Rev. **104**, 483 (1956).
[20] N. U. H. Syed, M. Guttormsen, F. Ingebretsen, A. C. Larsen, T. Lönnroth, J. Rekstad, A. Schiller, S. Siem, and A. Voinov, Phys. Rev. C **79**, 024316 (2009).
[21] S. Goriely, S. Hilaire, and A. J. Koning, Phys. Rev. C **78**, 064307 (2008).
[22] A. Gilbert and A. G. W. Cameron, Can. J. Phys. **43**, 1446 (1965).
[23] A. J. Koning, S. Hilaire, and S. Goriely, Nucl. Phys. A **810**, 13 (2008).
[24] A. J. Koning, S. Hilaire, and M. C. Duijvestijn, in *Proceedings of the International Conference on Nuclear Data for Science and Technology, April 22–27, 2007, Nice, France*, edited by O. Bersillon, F. Gunsing, E. Bauge, R. Jacqmin, and S. Leray (EDP Sciences, Les Ulis, France, 2008); [http://www.talys.eu/].
[25] Data extracted using the NNDC On-Line Data Service from the ENSDF database [http://www.nndc.bnl.gov/ensdf/].
[26] T. Belgya *et al.*, *Handbook for Calculations of Nuclear Reaction Data* (IAEA, Vienna, 2006); [http://www-nds.iaea.org/RIPL-2/].
[27] A. Voinov, E. Algin, U. Agvaanluvsan, T. Belgya, R. Chankova, M. Guttormsen, G. E. Mitchell, J. Rekstad, A. Schiller, and S. Siem, Phys. Rev. Lett. **93**, 142504 (2004).
[28] E. Algin, U. Agvaanluvsan, M. Guttormsen, A. C. Larsen, G. E. Mitchell, J. Rekstad, A. Schiller, S. Siem, and A. Voinov, Phys. Rev. C **78**, 054321 (2008).
[29] M. Guttormsen *et al.*, Phys. Rev. C **71**, 044307 (2005).
[30] A. C. Larsen *et al.*, Phys. Rev. C **73**, 064301 (2006).
[31] A. C. Larsen *et al.*, Phys. Rev. C **76**, 044303 (2007).
[32] A. Voinov, S. M. Grimes, C. R. Brune, M. Guttormsen, A. C. Larsen, T. N. Massey, A. Schiller, and S. Siem, Phys. Rev. C **81**, 024319 (2010).
[33] F. Bečvář, Nucl. Instrum. Methods Phys. Res. A **417**, 434 (1998).
[34] C. Djalali *et al.*, Nucl. Phys. A **388**, 1 (1982).
[35] J. Kopecky and R. E. Chrien, Nucl. Phys. A **468**, 285 (1987).
[36] J. Kopecky and M. Uhl, Phys. Rev. C **41**, 1941 (1990).
[37] M. Krtička and F. BeBečvář, J. Phys. G: Nucl. Part. Phys. **35**, 014025 (2008).
[38] S. A. Sheets *et al.*, Phys. Rev. C **79**, 024301 (2009).
[39] A. C. Larsen and S. Goriely, Phys. Rev. C **82**, 014318 (2010).
[40] L. McFadden and G. R. Satchler, Nucl. Phys. **84**, 177 (1966).
[41] P. Demetriou, C. Grama, and S. Goriely, Nucl. Phys. A **718**, 510 (2003).
[42] J. A. Holmes, S. E. Woosley, W. A. Fowler, and B. A. Zimmerman, At. Data Nucl. Data Tables **18**, 306 (1976).

7.7 Paper 3

PHYSICAL REVIEW C **87**, 014319 (2013)

Transitional γ strength in Cd isotopes

A. C. Larsen,[1,*] I. E. Ruud,[1] A. Bürger,[1] S. Goriely,[2] M. Guttormsen,[1] A. Görgen,[1] T. W. Hagen,[1] S. Harissopulos,[3] H. T. Nyhus,[1] T. Renstrøm,[1] A. Schiller,[4] S. Siem,[1] G. M. Tveten,[1] A. Voinov,[4] and M. Wiedeking[5]

[1]*Department of Physics, University of Oslo, N-0316 Oslo, Norway*

[2]*Institut d'Astronomie et d'Astrophysique, Université Libre de Bruxelles, CP 226, 1050 Brussels, Belgium*

[3]*Institute of Nuclear Physics, NCSR "Demokritos", 153.10 Aghia Paraskevi, Athens, Greece*

[4]*Department of Physics and Astronomy, Ohio University, Athens, Ohio 45701, USA*

[5]*iThemba LABS, P.O. Box 722, 7129 Somerset West, South Africa*

(Received 30 November 2012; published 16 January 2013)

The level densities and γ-ray strength functions of ^{105,106,111,112}Cd have been extracted from particle-γ coincidence data using the Oslo method. The level densities are in very good agreement with known levels at low excitation energy. The γ-ray strength functions display no strong enhancement for low γ energies. However, more low-energy strength is apparent for ^{105,106}Cd than for ^{111,112}Cd. For γ energies above $\approx$4 MeV, there is evidence for some extra strength, similar to what has been previously observed for the Sn isotopes. The origin of this extra strength is unclear; it might be due to $E1$ and $M1$ transitions originating from neutron skin oscillations or the spin-flip resonance, respectively.

DOI: 10.1103/PhysRevC.87.014319 PACS number(s): 25.20.Lj, 24.30.Gd, 25.40.Hs, 27.60.+j

I. INTRODUCTION

Recent measurements on the γ-strength function of several nuclei in the Fe–Mo mass region have revealed an unexpected enhancement for low γ energies ($E_\gamma \leqslant$ 3–4 MeV) [1–5]. However, no such feature was seen in the heavier Sn isotopes [6,7] or in the rare-earth region [8–10].

For ^{95}Mo, this low-energy enhancement has very recently been confirmed by an independent measurement and method [11]. It has also been shown in Ref. [12], that if this increase persists in exotic nuclei close to the neutron drip line, it could boost the Maxwellian-averaged neutron-capture cross sections up to two orders of magnitude.

However, as of today, there are more questions than answers regarding the low-energy enhancement. There is no theoretical work predicting such a behavior, the underlying physics is unknown, neither the multipolarity nor the electromagnetic character have been determined, and nobody knows for which nuclei the onset of this structure takes place.

So far, there is only one nucleus, ^{60}Ni, where there are strong indications that the enhancement is due to $M1$ transitions [13]. One should however be careful to draw any general conclusions, because ^{60}Ni is in many ways a special case. It has only positive-parity states below excitation energies of $\approx$4.5 MeV, which has significant consequences for the two-step cascade method employed in Ref. [13]. As discussed in Ref. [13], it means that for the secondary γ ray, $M1$ transitions are strongly enhanced compared to $E1$ transitions.

The motivation for this work is to determine the transitional region of the low-energy enhancementÊ by investigating the γ-strength function of Cd isotopes using the Oslo method. The Cd isotopes have $Z = 48$ and are in between Sn ($Z = 50$) and Mo ($Z = 42$). Thus, these experiments are a part of the experimental campaign exploring the onset of the low-energy enhancement.

In Sec. II, we give the experimental details and briefly describe the data analysis. In Sec. III, the normalization procedure of the level densities and γ-strength functions is discussed. Further, we compare the measured γ-strength functions with semi-empirical models in Sec. IV. Finally, we give a summary and outlook in Sec. V.

II. EXPERIMENTAL DETAILS AND DATA ANALYSIS

The experiments were performed at the Oslo Cyclotron Laboratory (OCL), utilizing a 38-MeV ^{3}He beam delivered by the Scanditronix cyclotron. In the first experiment, the beam was bombarding a self-supporting target of ^{106}Cd (96.7% enrichment) with mass thickness 1.1 mg/cm^2. Typical beam currents were 0.3–0.5 electrical nA (charge state ^{3}He^{2+}). In the second experiment, the target was 99.5% ^{112}Cd with mass thickness 0.95 mg/cm^2. The beam current was $\approx$0.1–0.2 electrical nA (charge state ^{3}He^{2+}). Both experiments were run for five days. The reactions of interest are ^{106,112}Cd(^{3}He,^{3}He$'\gamma$)^{106,112}Cd and ^{106,112}Cd(^{3}He,$\alpha\gamma$)^{105,111}Cd. The Q values of the pick-up reactions are 9703.9(124) keV and 11183.295(3) keV, respectively [14].

Particle-γ coincidences were measured with the silicon ring (SiRi) particle-detector system [15] and the CACTUS array for detecting γ rays [16]. The SiRi system consists of eight 130-μm thick silicon detectors, where each of them is divided into eight strips. One strip has an angular resolution of $\Delta\theta = 2^\circ$. Each of these segmented, thin detectors are put in front of a 1550-μm thick back detector. The full SiRi system has then 64 individual detectors in total, covering scattering angles between 40–54° and a solid-angle coverage of $\approx$6%. For the Cd experiments, SiRi was placed in forward angles with respect to the beam direction.

The CACTUS array consists of 28 collimated $5'' \times 5''$ NaI(Tl) crystals. The total efficiency of CACTUS is 15.2(1)% at $E_\gamma = 1332.5$ keV. The charged ejectiles and the γ rays were

*a.c.larsen@fys.uio.no

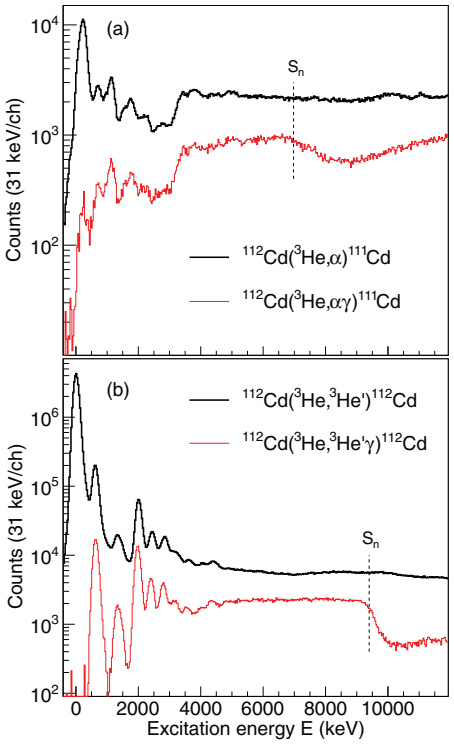

FIG. 1. (Color online) Singles particle spectra (thick, black line) and in coincidence with γ rays (thin, red line) from (a) the ^{112}Cd(^{3}He,α) reaction and (b) the ^{112}Cd(^{3}He,^{3}He$'$) reaction. The dashed lines indicate the neutron separation energies for the final nucleus.

measured in coincidence event-by-event, with time resolution of $\approx$15 ns.

Using the ΔE-E technique, each charged-particle species was identified. Gates were set on the ^{3}He and α ejectiles to select the correct reaction channel. Furthermore, the reaction kinematics and the known Q value for the reaction allowed us to relate the measured ejectile energy to the excitation energy of the residual nucleus.

In Fig. 1, the ^{3}He and α spectra with and without γ-coincidence requirements are shown. It is interesting to see how the ^{3}He and α spectra in coincidence with γ rays differ at the neutron separation energy. They both display a drop because the neutron channel is open. However, while the ^{3}He spectrum shows a rather abrupt drop (compatible with the energy resolution of $\approx$200 keV), the slope of the α spectrum is much less steep and a minimum is not reached until $\approx S_n + 1.5$ MeV. This can be explained by considering the final nuclei in the reactions ^{112}Cd(^{3}He,^{3}He$'n\gamma$)^{111}Cd and ^{112}Cd(^{3}He,$\alpha n\gamma$)^{110}Cd. In the latter case, the odd, final nucleus ^{111}Cd has many states within a relatively broad spin window at low excitation energy. However, this is not so for ^{110}Cd, where there are only 0^+ and 2^+ states below $\approx$1.5 MeV.

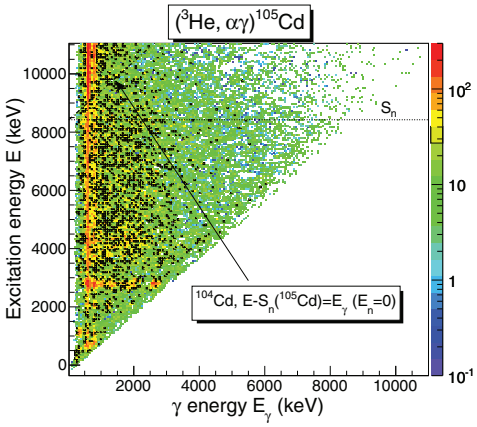

FIG. 2. (Color online) Excitation energy vs. γ energy matrix for ^{105}Cd. The γ-ray spectra are unfolded for each excitation-energy bin. The dashed line indicates the neutron separation energy in ^{105}Cd. The dashed-dotted line shows where the $E = E_\gamma$ diagonal would be in ^{104}Cd for the extreme case where the outgoing neutron has zero kinetic energy.

As the (^{3}He,α) reaction favors high-ℓ transfer in general, the populated states very likely have an average spin larger than 2. Thus, there is an effective spin hindrance which explains the observed behavior in the α spectrum.

The γ-ray spectra for each excitation-energy bin were unfolded using the known response functions of the CACTUS array, as described in Ref. [17]. The main advantage of this method is that the experimental statistical uncertainties are preserved, without introducing new, artificial fluctuations.

The matrix of unfolded γ spectra for each excitation-energy bin is shown for ^{105}Cd in Fig. 2. One may notice a peculiar feature in this matrix. Surprisingly, there is a considerable amount of γ rays from ^{105}Cd that survive several MeV above S_n, see the region to the right of the dashed-dotted line in Fig. 2. For example, the intensity of 5-MeV γ rays is practically the same for the excitation-energy region 7.0–8.0 MeV and 8.5–9.5 MeV. This could be caused by the difference in spin between the populated initial states and the spin of the first excited states in ^{104}Cd (2^+, 4^+).

After the γ spectra were unfolded, the distribution of first-generation γ rays[1] for each excitation-energy bin was extracted via an iterative subtraction technique [18]. The basic assumption of this method is that the decay routes are the same regardless of the population mechanism of the initial states (either directly via the nuclear reaction or from γ decay from above-lying states). For a discussion of uncertainties and possible errors of the first-generation method, see Ref. [19].

From the excitation energy vs. first-generation γ-ray matrix, one can extract the functional form of the level density and the γ transmission coefficient. This is done with an iterative

[1]The first γ ray emitted in the decay cascade.

procedure as described in Ref. [20], with the following ansatz:

$$P(E, E_\gamma) \propto \rho(E_\mathrm{f})\mathscr{T}(E_\gamma). \quad (1)$$

Here, $P(E, E_\gamma)$ is the experimental first-generation matrix, $\rho(E_\mathrm{f})$ is the level density at the final excitation energy E_f, with $E_\mathrm{f} = E - E_\gamma$, and $\mathscr{T}(E_\gamma)$ is the γ-transmission coefficient. Every point of the ρ and $\mathscr{T}$ functions is assumed to be an independent variable, and a global χ^2 minimum is reached typically within 10–20 iterations.

The method is based on the assumption that the reaction leaves the product nucleus in a compound state, which then subsequently decays in a manner that is independent on the way it was formed, i.e., a statistical decay process [21]. Therefore, a lower limit is set in the excitation energy to ensure that decay from compound states dominates the spectra. In addition, an upper excitation-energy limit at $\approx S_n$ is employed.[2] Because of methodical problems with the first-generation method for low γ energies, γ rays below $\approx$1.0 and 1.5 MeV for ^{105,111}Cd and ^{106,112}Cd, respectively, were excluded from the further analysis (see also Ref. [19]).

The γ-transmission coefficient $\mathscr{T}$ is a function of E_γ only, in accordance with the Brink hypothesis [22], which in its generalized form states that any collective decay mode has the same properties whether it is built on the ground state or on excited states. This assumption is proven to be incorrect for nuclear reactions involving high temperatures and/or spins, see for example Ref. [23]. However, in the present work, neither high-spin states nor high temperatures are reached ($T_\mathrm{f} \propto \sqrt{E_\mathrm{f}}$, and the populated spin range is centered within $J \sim 2$–$8\ \hbar$). Therefore, eventual spin and/or temperature dependencies should not have a significant impact on the results.

III. NORMALIZATION OF LEVEL DENSITY AND γ-STRENGTH FUNCTION

The extracted level density and the γ-ray transmission coefficient give identical fits to the experimental data with the transformations [20]

$$\tilde{\rho}(E - E_\gamma) = \mathscr{A}\exp[\alpha(E - E_\gamma)]\,\rho(E - E_\gamma), \quad (2)$$

$$\tilde{\mathscr{T}}(E_\gamma) = \mathscr{B}\exp(\alpha E_\gamma)\mathscr{T}(E_\gamma). \quad (3)$$

Therefore, the transformation parameters $\mathscr{A}$, α, and $\mathscr{B}$ were determined from external data.

A. Level density

For the level density, the absolute normalization $\mathscr{A}$ and the slope α can be determined from the known, discrete levels [24] at low excitation energy, and from neutron-resonance spacings at the neutron separation energy S_n [25]. For the latter, we must estimate the total level density at S_n from the neutron resonances, which are for a few spins only. Also, because of the selected lower limit of E_γ for the extraction of ρ and $\mathscr{T}$ (see Sec. II), our level-density data reach up to $E \approx S_n - 1$ MeV. Therefore, we must interpolate between our data and the level density at S_n. We have here chosen to use the back-shifted Fermi gas (FG) model with the parametrization of von Egidy and Bucurescu [26] for that purpose.

Because the spin distribution is poorly known at high excitation energies, a systematic uncertainty will be introduced to the slope of the level density and γ-strength function (see Ref. [19] for a thorough discussion on this subject). In addition, the light-ion reactions in the experiments populate only a certain spin range, which usually is for rather low spins. Therefore, the full spin distribution should also be folded with the experimental spin distribution.

In this work, we have tested two different approaches to normalize the level densities. First, we have used the back-shifted Fermi gas parametrization of von Egidy and Bucurescu [26] to estimate the total level density at the neutron separation energy, $\rho(S_n)$. Second, we have used the microscopic level densities of Goriely, Hilaire, and Koning [28] at high excitation energies. These level densities are calculated within the combinatorial plus Hartree-Fock-Bogoliubov approach, and are resolved in spin and parity. The applied parameters are listed in Table I, together with the Fermi-gas parameters of Ref. [26] used for the interpolation between our data and the estimated $\rho(S_n)$.

We start with the back-shifted Fermi gas approach. We adopt the expression for the spin cutoff parameter from Ref. [26]:

$$\sigma^2(E) = 0.0146A^{5/3}\frac{1 + \sqrt{1 + 4a(E - E_1)}}{2a}, \quad (4)$$

where A is the mass number, a is the level density parameter, and E_1 is the backshift parameter (see Ref. [26] for further details). The total level density can be calculated by

$$\rho(S_n) = \frac{2\sigma^2}{D_0}\frac{1}{(I_t + 1)\exp[-(I_t + 1)^2/2\sigma^2] + I_t\exp[-I_t^2/2\sigma^2]}, \quad (5)$$

where D_0 is the level spacing of s-wave neutrons and I_t is the ground-state spin of the target nucleus in the (n, γ) reaction. In Eq. (5), it is assumed that both parities contribute equally to the level density at S_n (see Refs. [20] and [19]).

From the Fermi-gas calculation, we get $\rho_\mathrm{FG}(S_n)$, which differs somewhat from the semi-experimental value $\rho(S_n)$. Therefore, a correction factor η is applied to ensure that the Fermi-gas interpolation matches $\rho(S_n)$ (see Table I).

As there is no information on the level spacing for ^{105,106}Cd (^{104,105}Cd are unstable), we have estimated the total level density at the neutron separation energy from systematics for these nuclei, see Fig. 3. Here, we have calculated the semiexperimental $\rho(S_n)$ for all Cd isotopes where the neutron resonance spacing D_0 is known. For all D_0 values we have used the Reference Input Parameter Library (RIPL-3) evaluation [25], except for ^{117}Cd where we have also used the RIPL-2 value.

It is striking how the values of $\rho(S_n)$ actually decrease as a function of S_n for the isotopes with $A \leqslant 108$. This is probably an effect of approaching the $N = 50$ closed shell. It is, however, unfortunate that there are no experimental D_0 values for these nuclei, so the uncertainty of the estimated

[2] When the neutron channel is open, the excitation energy is not well defined anymore, because neutron energies are not measured.

TABLE I. Parameters used for the calculation of $\rho(S_n)$ (see text).

Nucleus	I_i^π	D_0 (eV)	S_n (MeV)	$\sigma(S_n)$	a (MeV^{-1})	E_1 (MeV)	$\rho_{FG}(S_n)$ (10^5 MeV^{-1})	$\rho(S_n)$ (10^5 MeV^{-1})	η	$\tilde{\sigma}(S_n)$	$\tilde{\rho}(S_n)$ (10^5 MeV^{-1})	shift E_{HFB} (MeV)	range I_i ($\hbar$)
^{105}Cd	0^+	–	8.427	5.71	10.88	−0.567	1.43	1.78(89)[a]	1.25	4.5	1.11(56)[a]	0.042	1/2 − 13/2
^{106}Cd	$5/2^+$	–	10.874	5.85	11.39	0.746	6.44	8.05(40)[a]	1.25	4.5	5.3(26)[a]	0.052	0 − 6
^{111}Cd	0^+	155(20)	6.976	5.43	13.56	−0.640	2.99	3.87(91)	1.29	4.5	2.68(72)	0.435	1/2 − 13/2
^{112}Cd	$1/2^+$	27(2)	9.394	5.61	13.82	0.713	11.9	12.0(25)	1.01	4.5	7.8(16)	0.540	0 − 6

[a]Estimated from systematics.

$\rho(S_n)$ for ^{105,106}Cd must necessarily be large; we have assumed a 50% uncertainty.

The normalization procedure is demonstrated for ^{112}Cd in Fig. 4. The agreement between our data and the discrete levels [24] is very satisfying. We notice however that the ground state seems to be underestimated; this is probably because there are very few direct decays to the ground state, most of the decay goes through the first 2^+ state. We also see that the triplet of two-phonon vibrational states 0^+, 2^+, 4^+, at about $E \approx 1.4$ MeV, is clearly seen in our level-density data, as well as the one-phonon first excited 2^+ state at 0.62 MeV (see, e.g., Ref. [27] for a discussion on the vibrational nature of Cd isotopes).

The level densities normalized with the back-shifted Fermi gas approach are shown in Fig. 5(a). Again, the effect of approaching the $N = 50$ closed shell is clearly seen. The slope in level density is smaller for ^{105,106}Cd than for ^{111,112}Cd. Also, we see that the level densities of the neighboring isotopes are

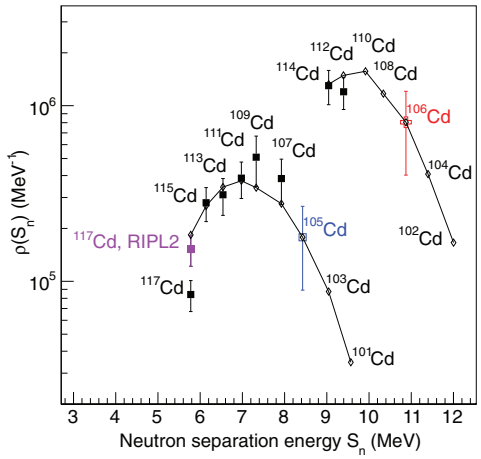

FIG. 3. (Color online) Estimation of $\rho(S_n)$ for ^{105,106}Cd. The filled, black squares are calculated from known neutron resonance spacings in RIPL-3 [25] using Eq. (5) with σ values from Ref. [26]. The filled, violet square is the result for ^{117}Cd using the D_0 value recommended in RIPL-2. The small, open diamonds connected with lines are calculated values from the back-shifted Fermi gas approach [26] multiplied with a common factor of 1.25 to bring them within the error bars of the semiexperimental $\rho(S_n)$ values. The blue, open square and the red, open cross are the estimated values for $\rho(S_n)$ of ^{105,106}Cd, respectively.

parallel, but the increase in level density of the odd-A nucleus compared to the even neighbor is smaller for ^{105}Cd than for ^{111}Cd.

For the second approach, we have used the combinatorial plus HFB calculations of Ref. [28]. Here, we have normalized our data to obtain a best fit to the microscopic level densities at high excitation energies ($E \geqslant$ 4–5 MeV). As described in Ref. [28], an energy shift is used in order to optimize the reproduction of the known, discrete levels. The applied energy shifts are listed in Table I.

The level-density data normalized to the microscopic calculations are shown in Fig. 5(b). It is seen that the two independent normalization methods yield very similar results.

We have also taken into account that the spin distribution of the initial levels could be rather narrow. As discussed in Ref. [29], the (^{3}He,α) reaction in forward angles gives an average spin transfer of $\approx 5\hbar$ at $E \approx 5$ MeV in the rare-earth region. For excitation energies below 3 MeV, it is shown in Ref. [30] that the ^{106}Cd(^{3}He,α)^{105}Cd reaction involves $\ell =$ 2, 4, and 5.

Turning to the inelastic scattering, where vibrational states are favored, we see from the ^{106,112}Cd data below $E \approx 3$ MeV that levels with $I = 2, 3, 4$ are strongly populated. For levels with higher spins the data are inconclusive, but it is clear that they are significantly less populated. We therefore estimate

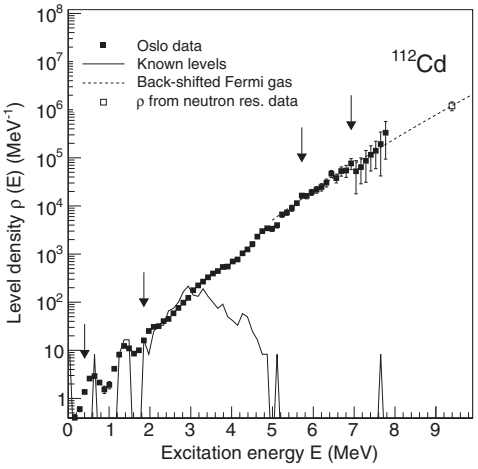

FIG. 4. Normalization of the level density of ^{112}Cd to the known, discrete levels (jagged line), and $\rho(S_n)$ (see text).

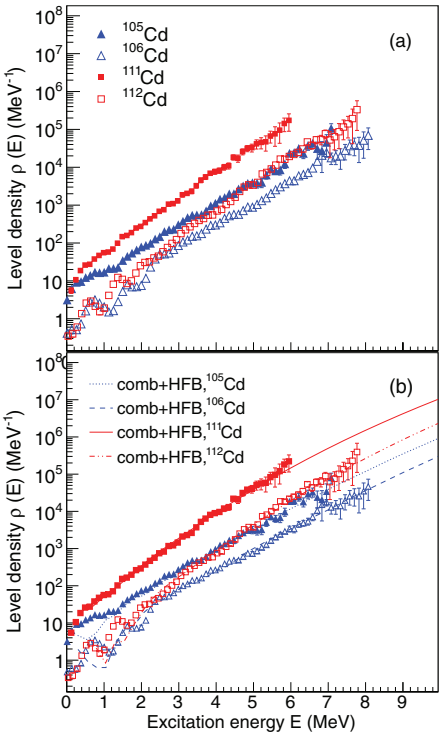

FIG. 5. (Color online) Normalized level densities of ^{105,106,111,112}Cd with (a) the Fermi-gas approach and (b) the combinatorial plus Hartree-Fock-Bogoliubov approach.

a reduced spin cutoff parameter, $\tilde{\sigma}$, to be ≈4.5 for all the Cd nuclei studied here. This corresponds to a reduced level density at S_n, $\tilde{\rho}(S_n)$. For the microscopic level densities, which are spin-dependent, we filter out the levels within the approximate experimental spin range (see Table I).

The four different normalizations are shown for ^{112}Cd for $E = 3$–8 MeV in Fig. 6. As seen in this figure, the effect of the reduced spin range is not large at low excitation energies, but could be as much as a factor of 2 for example at $E = 7.9$ MeV.

B. γ strength function

The slope of the γ strength function is given by the slope of the level density, see Eqs. (2) and (3). Therefore, the only parameter left to determine is the absolute value $\mathscr{B}$. This is done using known values on the average, total radiative width at S_n, $\langle\Gamma_{\gamma 0}\rangle$, extracted from s-wave neutron resonances [25] by [31]

$$\langle\Gamma_\gamma(S_n, I_t \pm 1/2, \pi_t)\rangle = \frac{D_0}{4\pi}\int_{E_\gamma=0}^{S_n} \mathrm{d}E_\gamma \mathscr{B}\mathscr{T}(E_\gamma)\rho(S_n - E_\gamma) \times \sum_{I=-1}^{1} g(S_n - E_\gamma, I_t \pm 1/2 + I), \quad (6)$$

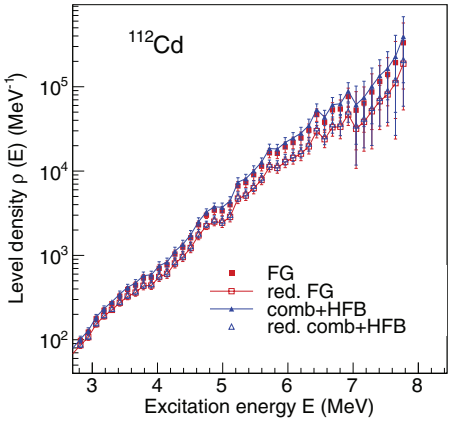

FIG. 6. (Color online) The various normalizations of ^{112}Cd: the Fermi-gas approach (FG, red squares), FG approach with a reduced spin-cutoff parameter (red, open squares), the combinatorial plus HFB approach (blue triangles), and with a reduced spin range (open, blue triangles).

where I_t and π_t are the spin and parity of the target nucleus in the (n, γ) reaction, and $\rho(S_n - E_\gamma)$ is the experimental level density. The spin distribution is assumed to be given by [32]

$$g(E, I) \simeq \frac{2I+1}{2\sigma^2}\exp[-(I+1/2)^2/2\sigma^2] \quad (7)$$

for a specific excitation energy E, spin I, and a spin cutoff parameter σ. All values are known in Eq. (6) except the parameter $\mathscr{B}$, which can now be determined.

For ^{111,112}Cd, the values for $\langle\Gamma_{\gamma 0}\rangle$ are 71(6) and 106(15) meV, respectively. However, again we lack neutron resonance data for ^{105,106}Cd. We must therefore estimate $\langle\Gamma_{\gamma 0}\rangle$ and D_0 for these nuclei. For the FG approach, D_0 is evaluated from the previously estimated $\rho(S_n)$ values (see Table I). We get $D_0 = 375(188)$ and 16.3(82) eV for ^{105,106}Cd, respectively. The combinatorial plus HFB calculations predict $D_0 =$ 294 eV and 13.6 eV for ^{105,106}Cd, respectively.

To estimate the average total radiative width, we have considered systematics from the Cd isotopes where $\langle\Gamma_{\gamma 0}\rangle$ is known, see Fig. 7. It is difficult to predict with reasonable certainty the unknown values for ^{105,106}Cd because of the possible shell effects. Because we also lack data on ^{108,110}Cd, it is especially problematic for ^{106}Cd. We have therefore also assumed that for γ energies above ≈5–6 MeV, the strength functions for all the Cd isotopes should be very similar, because this region should be dominated by the low-energy tail of the giant electric dipole resonance (GDR). The GDR is mainly governed by the number of protons, and thus it is reasonable to believe that the properties should be the same for all Cd isotopes, at least to a large extent.

As shown in Fig. 7, we have fitted a quadratic function to the $\langle\Gamma_{\gamma 0}\rangle$ values of the odd Cd isotopes, and for ^{105}Cd we estimate $\langle\Gamma_{\gamma 0}\rangle = 187(94)$ meV. For the even isotopes, we only have two data points. However, considering the trend for the odd isotopes and claiming the postulated similarity of the strength functions at high E_γ, we have chosen a rather large value of

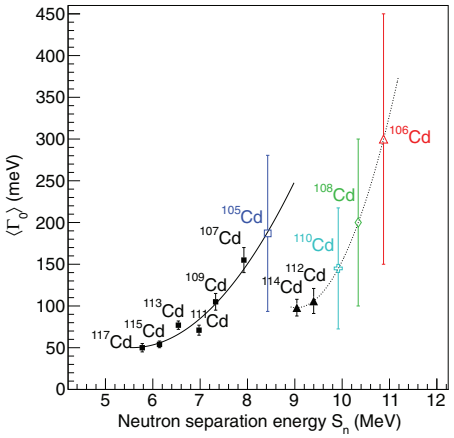

FIG. 7. (Color online) Estimation of $\langle\Gamma_{\gamma 0}\rangle$ for ^{105,106}Cd (see text). The black squares are for known values for odd Cd isotopes and the black triangles are for the even ones; all values are taken from Ref. [25]. The dashed-dotted line represents the best fit with a quadratic function for the odd nuclei. The blue, open square is the estimated $\langle\Gamma_{\gamma}\rangle$ for ^{105}Cd, and the red, open triangle for ^{106}Cd. The dashed line indicates a quadratic function for the even isotopes in the same fashion as for the odd ones. Estimations of ^{108,110}Cd are shown for completeness (green, open diamond and cyan, open cross, respectively).

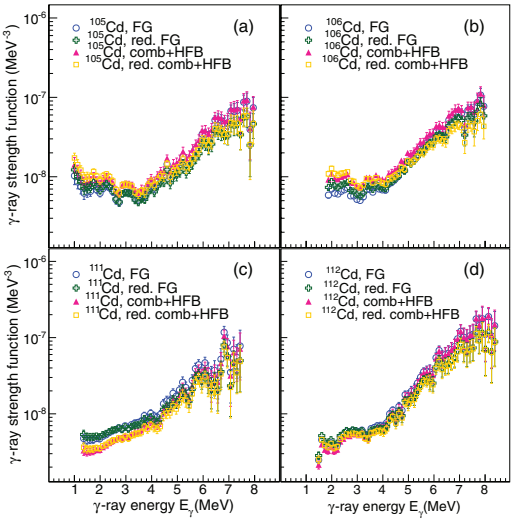

FIG. 8. (Color online) Gamma-ray strength functions of (a) ^{105}Cd, (b) ^{106}Cd, (c) ^{111}Cd, and (d) ^{112}Cd for the four different normalization approaches on the level densities.

300(150) meV. To guide the eye, we have shown a quadratic fit as for the odd case, and displayed the predicted $\langle\Gamma_{\gamma 0}\rangle$ values also for ^{108,110}Cd (see Fig. 7).

The normalized γ strength functions for the four different level-density normalizations of ^{105,106,111,112}Cd are shown in Fig. 8. We clearly see a difference in the strength for $E_\gamma < 4$ MeV for the heavier ^{111,112}Cd compared to the lighter ^{105,106}Cd. For the latter, the tendency is a more flat and even a slightly increasing γ-strength function, while for the former the γ strength is decreasing when E_γ decreases. Although there is no strong low-energy enhancement as in Fe or Mo, it could indicate that this is the transitional mass region for the low-energy enhancement of the γ strength.

Another observation is that all the Cd strength functions seem to change slope at $E_\gamma \approx 4$ MeV. Above this value, the slope is significantly steeper than for lower γ energies. This has previously been seen in Sn isotopes [6,7]. These issues will be further addressed in the following section.

IV. COMPARISON WITH OTHER DATA AND MODELS

As mentioned in the previous section, our Cd data on the γ-strength function lack a strong low-energy enhancement, although the lighter isotopes appear to have more low-energy strength than the heavier ones. In addition, it is very likely that some extra strength is present in the region of $4 \leqslant E_\gamma \leqslant 8$ MeV.

In Fig. 9, we have compared the strength functions of ^{105,112}Cd with ^{95}Mo [2] and ^{117}Sn [6]. It is very interesting to see how much ^{112}Cd resembles ^{117}Sn. On the other hand, ^{95}Mo is very different from both ^{112}Cd and ^{117}Sn, while ^{105}Cd seems to be somewhat in between ^{95}Mo and ^{117}Sn for $2 \leqslant E_\gamma \leqslant 4$ MeV. For higher γ energies, also ^{105}Cd looks very much the same as ^{117}Sn.

To gain more insight of the observed γ strength functions, we would like to compare our data with model calculations. One of the more widely used models for the $E1$ γ strength is the generalized Lorentzian (GLO) model [33,34]. This is a model tailored to give a reasonable description both on the photoabsorption cross section in the GDR region, and on the γ strength below the neutron separation energy. It is in principle dependent on the temperature of the final states T_f, which

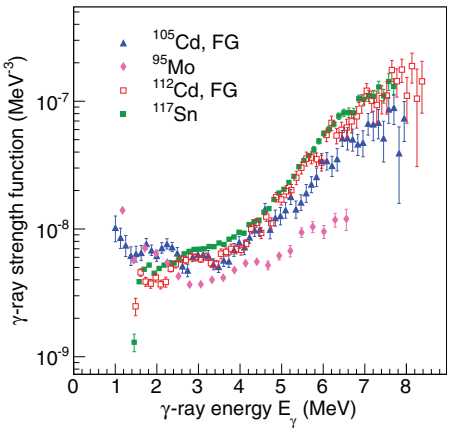

FIG. 9. (Color online) Comparison of γ strength functions of ^{95}Mo, ^{105,112}Cd, and ^{117}Sn (see text).

TABLE II. Parameters used for the RSF models.

Nucleus	$E_{E1,1}$ (MeV)	$\sigma_{E1,1}$ (mb)	$\Gamma_{E1,1}$ (MeV)	$E_{E1,2}$ (MeV)	$\sigma_{E1,2}$ (mb)	$\Gamma_{E1,2}$ (MeV)	$T_{\min}$ (MeV)	$T_{\max}$ (MeV)	E_{M1} (MeV)	σ_{M1} (mb)	Γ_{M1} (MeV)	E_{pyg} (MeV)	σ_{pyg} (MeV)	$C_{\text{pyg}}(T_{\min})$ (10^{-7} MeV^{-2})	$C_{\text{pyg}}(T_{\max})$ (10^{-7} MeV^{-2})
^{105}Cd	14.7	151.8	4.39	17.0	75.8	5.81	0.35	0.40	8.69	0.94	4.0	8.7(2)	1.5(1)	2.2(2)	1.1(1)
^{106}Cd	14.6	153.7	4.37	16.9	76.7	5.79	0.35	0.40	8.66	0.94	4.0	8.7(2)	1.5(1)	2.4(2)	1.1(2)
^{111}Cd	14.5	162.8	4.28	16.8	81.3	5.67	0.37	0.47	8.53	0.90	4.0	8.7(2)	1.5(1)	2.9(3)	1.7(2)
^{112}Cd	14.4	164.5	4.26	16.7	82.1	5.65	0.37	0.40	8.51	0.89	4.0	8.7(2)	1.5(1)	3.7(3)	2.4(4)

is in contradiction to the Brink hypothesis [22]. However, by introducing a constant temperature, the hypothesis is regained.

The strength function within the GLO model is given by

$$f_{\text{GLO}}(E_\gamma, T_f) = \frac{1}{3\pi^2\hbar^2c^2}\sigma_{E1}\Gamma_{E1}\left[\frac{E_\gamma\Gamma(E_\gamma,T_f)}{\left(E_\gamma^2-E_{E1}^2\right)^2+E_\gamma^2\Gamma(E_\gamma,T_f)^2} + 0.7\frac{\Gamma(E_\gamma=0,T_f)}{E_{E1}^3}\right], \quad (8)$$

with

$$\Gamma(E_\gamma,T_f)=\frac{\Gamma_{E1}}{E_{E1}^2}\left(E_\gamma^2+4\pi^2T_f^2\right). \quad (9)$$

The Lorentzian parameters Γ_{E1}, E_{E1}, and σ_{E1} correspond to the width, centroid energy, and peak cross section of the GDR. We have made use of the parametrization of RIPL-2 [25] to estimate the GDR parameters as these are unknown experimentally for the individual Cd isotopes, see Table II. Because the even-even Cd isotopes are known to have a nonzero ground-state deformation [25], the GDR is split in two and we have therefore two sets of Lorentzian parameters (denoted by subscripts 1 and 2, see Table II). For the $M1$ strength, we have used a Lorentzian shape with the parametrization in Ref. [25].

We treat the extra strength for high γ energies in the same way as for the Sn isotopes [6,7], adding a Gaussian-shaped pygmy resonance:

$$f_{\text{pyg}}=C_{\text{pyg}}\frac{1}{\sqrt{2\pi}\sigma_{\text{pyg}}}\exp\left[\frac{-(E_\gamma-E_{\text{pyg}})^2}{2\sigma_{\text{pyg}}^2}\right]. \quad (10)$$

Here C_{pyg} is a normalization constant, σ_{pyg} is the standard deviation, and E_{pyg} is the centroid of the resonance.

The temperature of the final states is assumed to be constant, and is treated as a free parameter to get the best possible agreement with our data. As the normalization is uncertain, also the temperature is uncertain. In general, we get a slightly higher temperature for the normalization options that give the largest low-energy γ strength. We denote the temperature for the normalization giving the largest low-energy strength $T_{\max}$, and the smallest low-energy strength $T_{\min}$. The adopted γ-strength model parameters are given in Table II.

As there are no photoneutron cross-section data on the individual Cd isotopes, we have compared our measurements with (γ, x) data on natural Cd from Ref. [35] and (γ, n) data on ^{106,108}Pd taken from Ref. [36]. Assuming that the photoneutron cross section $\sigma_\gamma(E_\gamma)$ is dominated by dipole transitions, we convert it into γ strength by [25]

$$f_\gamma(E_\gamma)=\frac{1}{3\pi^2\hbar^2c^2}\frac{\sigma_\gamma}{E_\gamma}. \quad (11)$$

In Fig. 10, our data on the γ strength function of ^{105}Cd and the photonuclear data are shown together with the model calculations for the lowest temperature $T_{\min}$ in the GLO model. It can be seen that the calculations are in reasonable agreement with the Pd data from Ref. [36] and our data down to $E_\gamma \approx$ 3.5 MeV. For lower γ energies, our data show significantly more strength than the constant-temperature calculations.

Because γ decay has a considerable probability also above S_n for ^{105}Cd, see Fig. 2, we have extracted the strength function for this nucleus up to $E_\gamma \approx 9.3$ MeV. This is done by choosing a higher E_γ limit of 2.25 MeV in the first-generation matrix to ensure that we do not mix with data from the ^{104}Cd channel. The resulting strength function is displayed in Fig. 10 as open squares. Although the statistical errors are quite large, we are able to bridge the gap up to the (γ, n) measurements, thus further supporting the presence of an enhanced strength in the

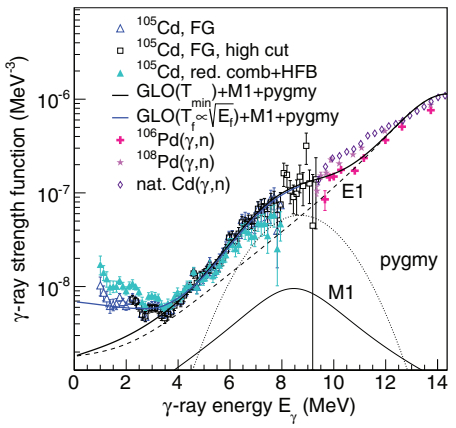

FIG. 10. (Color online) Calculations using the GLO model with a constant temperature ($T_{\min}$) and a variable temperature ($T_f \propto \sqrt{E_f}$) compared to data of ^{105}Cd for the normalization giving the lowest possible low-energy strength (FG) and the highest (combinatorial-plus-HFB, reduced spin window). The black triangles show the extracted strength function for a higher cut on E_γ and E in the first-generation matrix of ^{105}Cd. Photonuclear data from Refs. [35,36] are also shown.

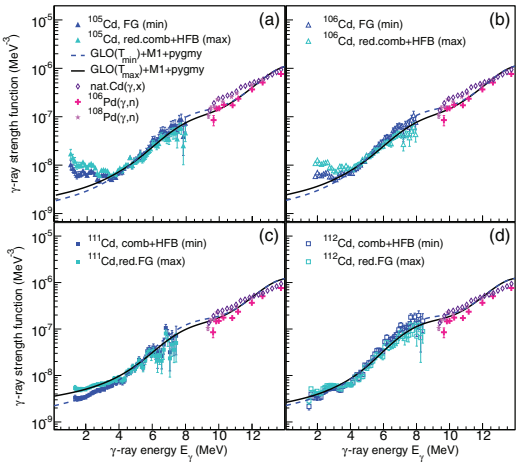

FIG. 11. (Color online) Modeled γ strength functions compared to the data for (a) ^{105}Cd, (b) ^{106}Cd, (c) ^{111}Cd, and (d) ^{112}Cd for the level-density normalizations which give the minimum or maximum strength at low γ energies. Photonuclear data from Refs. [35,36] are also displayed.

6–10 MeV region. It is also a strong indication that the $\langle\Gamma_\gamma\rangle$ value we have chosen for normalization is reasonable.

The resulting γ-strength models for all the Cd isotopes studied here are shown together with our data and the photonuclear data in Fig. 11. We observe that the models fit our data quite well, in particular for ^{111,112}Cd. The extra strength between $E_\gamma \approx 5$–8 MeV seems to be well described by a Gaussian function just as in the Sn case.

As of today, the origin of this strength is not well understood. It could be due to enhanced probability for $E1$ transitions due to the so-called neutron skin oscillation, see Refs. [6,7] and references therein. There is also a possibility that the $M1$ spin-flip resonance gives more strength than the parametrization we have adopted here. In a recent work on ^{90}Zr by Iwamoto *et al.* [37], it is shown how both an $E1$ pygmy dipole resonance and an $M1$ resonance are present in the energy region $E_\gamma \approx 6$–11 MeV, with similar strengths. It could be that the same is the case also for the Cd isotopes. Unfortunately, with our experimental technique it is not possible to separate $E1$ and $M1$ transitions in the γ strength. It would therefore be highly desirable to investigate this further with the experimental technique applied in Ref. [37].

Assuming that all the pygmy strength is of $E1$ type, we have compared the energy-integrated strength of this structure with the classical energy-weighted Thomas-Reiche-Kuhn (TRK) sum rule (without exchange forces) given by [38]

$$\sigma_{\mathrm{TRK}} \simeq 60\frac{NZ}{A}\ [\mathrm{MeV\,mb}]\,. \tag{12}$$

The results are shown in Table III.

The uncertainty of the normalization gives a rather large uncertainty in the fraction of the sum rule, but the general trend is an increasing pygmy strength as the neutron number increases. This is in agreement with expectations based on the neutron-skin oscillation mode, see for example Ref. [39].

TABLE III. Maximum and minimum integrated strengths of the pygmy resonance.

Nucleus	$\sigma(T_{\mathrm{max}})$ (MeV mb)	$\sigma(T_{\mathrm{min}})$ (MeV mb)	TRK (MeV mb)	% of TRK
^{105}Cd	11.3	21.8	1563.4	0.7–1.4
^{106}Cd	11.3	24.4	1575.9	0.7–1.5
^{111}Cd	17.4	28.7	1634.6	1.1–1.8
^{112}Cd	24.4	37.4	1645.7	1.5–2.3

We note that for ^{105,106}Cd, the models underestimate the strength for $E_\gamma < 3$ MeV. Also, we find it not possible to compensate for this by just increasing T_f, because then the overall strength will be too large for the data at higher γ energies. In an attempt to describe the extra strength at low γ energies, we have tested a variable temperature of the final levels, $T_f \propto \sqrt{E_f}$, in the GLO model. This is shown as a solid, blue line in Fig. 10. It is seen that the variable-temperature model is rather successful in describing the low-energy data for the normalization giving the lowest low-energy strength.

It is however hard to explain why one should have a constant temperature for ^{111,112}Cd and a variable one for ^{105,106}Cd. By inspecting the level densities, they all have an approximately constant slope in log scale, compatible with a constant-temperature level density $\rho_{\mathrm{CT}}(E) \propto \exp(E/T)$. This has recently been supported by particle-evaporation experiments in lighter nuclei [40]. In addition, the variable-temperature approach is not able to reproduce the data normalized to give maximum strength at low γ energies (reduced spin range for the initial levels). We therefore conclude that it is more probable that some low-lying strength is present below $E_\gamma \approx 3.5$ MeV for ^{105,106}Cd, similar as for the Mo isotopes but not as strong. However, one must keep in mind that the uncertainty in the level-density normalization hampers any firm statements. Further studies of nuclei in this mass region are ongoing, and will hopefully shed more light on this issue.

V. SUMMARY AND OUTLOOK

The level densities and γ-ray strength functions of ^{105,106,111,112}Cd have been deduced from particle-γ coincidence data using the Oslo method. The level densities are in excellent agreement with known levels at low excitation energy. We note that the slope in level density decreases from the heavier ^{111,112}Cd to the lighter ^{105,106}Cd. This is probably due to the neutron number approaching the $N = 50$ closed shell.

The γ-ray strength functions for all the Cd isotopes display an enhancement for $E_\gamma > 4$ MeV, very similar to features observed in the previously studied Sn isotopes. The nature of this extra strength could not be determined in the present work, but could in principle be due to both $E1$ and $M1$ transitions. Future investigations are highly desirable to resolve these multipolarities.

At γ-ray energies below 3 MeV, the γ-strength function of the lighter ^{105,106}Cd isotopes show an increase compared to ^{111,112}Cd. Although this might be due to the vicinity of the $N = 50$ shell closure and the resulting reduced level density in the lighter isotopes, it is more likely that this work uncovered the mass region exhibiting the onset of the low-energy enhancement. Further measurements are in progress and the results will provide more details regarding this transitional region.

ACKNOWLEDGMENTS

We are very grateful to C. Scholey and the nuclear physics group at the University of Jyväskylä (JYFL) for lending us the ^{106,112}Cd targets. Funding of this research from the Research Council of Norway, project Grants No. 180663 and 205528, is gratefully acknowledged. M.W. acknowledges support from the National Research Foundation of South Africa. We would like to give special thanks to E. A. Olsen, A. Semchenkov, and J. Wikne for providing the beam.

[1] A. Voinov, E. Algin, U. Agvaanluvsan, T. Belgya, R. Chankova, M. Guttormsen, G. E. Mitchell, J. Rekstad, A. Schiller, and S. Siem, Phys. Rev. Lett. **93**, 142504 (2004).
[2] M. Guttormsen, R. Chankova, U. Agvaanluvsan, E. Algin, L. A. Bernstein, F. Ingebretsen, T. Lönnroth, S. Messelt, G. E. Mitchell, J. Rekstad, A. Schiller, S. Siem, A. C. Sunde, A. Voinov, and S. Ødegård, Phys. Rev. C **71**, 044307 (2005).
[3] A. C. Larsen, R. Chankova, M. Guttormsen, F. Ingebretsen, S. Messelt, J. Rekstad, S. Siem, N. U. H. Syed, S. W. Ødegård, T. Lönnroth, A. Schiller, and A. Voinov, Phys. Rev. C **73**, 064301 (2006).
[4] A. C. Larsen, M. Guttormsen, R. Chankova, F. Ingebretsen, T. Lönnroth, S. Messelt, J. Rekstad, A. Schiller, S. Siem, N. U. H. Syed, and A. Voinov, Phys. Rev. C **76**, 044303 (2007).
[5] M. Guttormsen, A. C. Larsen, A. Bürger, A. Görgen, S. Harissopulos, M. Kmiecik, T. Konstantinopoulos, M. Krtička, A. Lagoyannis, T. Lönnroth, K. Mazurek, M. Norrby, H. T. Nyhus, G. Perdikakis, A. Schiller, S. Siem, A. Spyrou, N. U. H. Syed, H. K. Toft, G. M. Tveten, and A. Voinov, Phys. Rev. C **83**, 014312 (2011).
[6] U. Agvaanluvsan, A. C. Larsen, R. Chankova, M. Guttormsen, G. E. Mitchell, A. Schiller, S. Siem, and A. Voinov, Phys. Rev. Lett. **102**, 162504 (2009).
[7] H. K. Toft, A. C. Larsen, A. Bürger, M. Guttormsen, A. Görgen, H. T. Nyhus, T. Renstrøm, S. Siem, G. M. Tveten, and A. Voinov, Phys. Rev. C **83**, 044320 (2011).
[8] U. Agvaanluvsan, A. Schiller, J. A. Becker, L. A. Bernstein, P. E. Garrett, M. Guttormsen, G. E. Mitchell, J. Rekstad, S. Siem, A. Voinov, and W. Younes, Phys. Rev. C **70**, 054611 (2004).
[9] M. Guttormsen, A. Bagheri, R. Chankova, J. Rekstad, S. Siem, A. Schiller, and A. Voinov, Phys. Rev. C **68**, 064306 (2003).
[10] H. T. Nyhus, S. Siem, M. Guttormsen, A. C. Larsen, A. Bürger, N. U. H. Syed, G. M. Tveten, and A. Voinov, Phys. Rev. C **81**, 024325 (2010).
[11] M. Wiedeking, L. A. Bernstein, M. Krtička, D. L. Bleuel, J. M. Allmond, M. S. Basunia, J. T. Burke, P. Fallon, R. B. Firestone, B. L. Goldblum, R. Hatarik, P. T. Lake, I-Y. Lee, S. R. Lesher, S. Paschalis, M. Petri, L. Phair, and N. D. Scielzo, Phys. Rev. Lett. **108**, 162503 (2012).
[12] A. C. Larsen and S. Goriely, Phys. Rev. C **82**, 014318 (2010).
[13] A. Voinov, S. M. Grimes, C. R. Brune, M. Guttormsen, A. C. Larsen, T. N. Massey, A. Schiller, and S. Siem, Phys. Rev. C **81**, 024319 (2010).
[14] Data extracted from the Q-value calculator at the National Nuclear Data Center database, http://www.nndc.bnl.gov/qcalc/.
[15] M. Guttormsen, A. Bürger, T. E. Hansen, and N. Lietaer, Nucl. Instrum. Methods Phys. Res. A **648**, 168 (2011).
[16] M. Guttormsen, A. Ataç, G. Løvhøiden, S. Messelt, T. Ramsøy, J. Rekstad, T. F. Thorsteinsen, T. S. Tveter, and Z. Zelazny, Phys. Scr., T **32**, 54 (1990).
[17] M. Guttormsen, T. S. Tveter, L. Bergholt, F. Ingebretsen, and J. Rekstad, Nucl. Instrum. Methods Phys. Res. A **374**, 371 (1996).
[18] M. Guttormsen, T. Ramsøy, and J. Rekstad, Nucl. Instrum. Methods Phys. Res. A **255**, 518 (1987).
[19] A. C. Larsen, M. Guttormsen, M. Krtička, E. Běták, A. Bürger, A. Görgen, H. T. Nyhus, J. Rekstad, A. Schiller, S. Siem, H. K. Toft, G. M. Tveten, A. V. Voinov, and K. Wikan, Phys. Rev. C **83**, 034315 (2011).
[20] A. Schiller, L. Bergholt, M. Guttormsen, E. Melby, J. Rekstad, and S. Siem, Nucl. Instrum. Methods Phys. Res. A **447**, 498 (2000).
[21] A. Bohr and B. Mottelson, *Nuclear Structure* (Benjamin, New York, 1969), Vol. I.
[22] D. M. Brink, Ph.D. thesis, Oxford University, 1955.
[23] A. Schiller and M. Thoennessen, At. Data Nucl. Data Tables **93**, 549 (2007).
[24] Data extracted using the NNDC On-Line Data Service from the ENSDF database, March 2012, http://www.nndc.bnl.gov/ensdf/.
[25] R. Capote *et al.*, Reference Input Parameter Library, RIPL-2 and RIPL-3, available online at http://www-nds.iaea.org/RIPL-3/.
[26] T. von Egidy and D. Bucurescu, Phys. Rev. C **72**, 044311 (2005); **73**, 049901(E) (2006).
[27] P. E. Garrett and J. L. Wood, J. Phys. G **37**, 064028 (2010); **37**, 069701 (2010).
[28] S. Goriely, S. Hilaire, and A. J. Koning, Phys. Rev. C **78**, 064307 (2008).
[29] M. Guttormsen, L. Bergholt, F. Ingebretsen, G. Løvhøiden, S. Messelt, J. Rekstad, T. S. Tveter, H. Helstrup, and T. F. Thorsteinsen, Nucl. Phys. A **573**, 130 (1994).
[30] R. Chapman and G. D. Dracoulis, J. Phys. G. **1**, 657 (1975).
[31] A. Voinov, M. Guttormsen, E. Melby, J. Rekstad, A. Schiller, and S. Siem, Phys. Rev. C **63**, 044313 (2001).
[32] A. Gilbert and A. G. W. Cameron, Can. J. Phys. **43**, 1446 (1965).
[33] J. Kopecky and R. E. Chrien, Nucl. Phys. A **468**, 285 (1987).
[34] J. Kopecky and M. Uhl, Phys. Rev. C **41**, 1941 (1990).

[35] A. Lepretre, H. Beil, R. Bergere, P. Carlos, A. Deminiac, and A. Veyssiere, Nucl. Phys. A **219**, 39 (1974).
[36] H. Utsunomiya, S. Goriely, H. Akimune, H. Harada, F. Kitatani, S. Goko, H. Toyokawa, K. Yamada, T. Kondo, O. Itoh, M. Kamata, T. Yamagata, Y.-W. Lui, I. Daoutidis, D. P. Arteaga, S. Hilaire, and A. J. Koning, Phys. Rev. C **82**, 064610 (2010).
[37] C. Iwamoto *et al.*, Phys. Rev. Lett. **108**, 262501 (2012).
[38] W. Thomas, Naturwissenschaften **13**, 627 (1925); W. Kuhn, Z. Phys. **33**, 408 (1925); F. Reiche and W. Thomas, *ibid.* **34**, 510 (1925).
[39] I. Daoutidis and S. Goriely, Phys. Rev. C **86**, 034328 (2012).
[40] A. V. Voinov, B. M. Oginni, S. M. Grimes, C. R. Brune, M. Guttormsen, A. C. Larsen, T. N. Massey, A. Schiller, and S. Siem, Phys. Rev. C **79**, 031301(R) (2009).

7.8 Paper 4

Chapter 8

Conclusion and outlook

Through the work presented in this dissertation the level scheme of the moderately neutron rich isotopes ^{167}Ho, ^{168}Ho and ^{169}Ho has been extended. The experimental level scheme was utilized to extract information on the quadrupole deformation of the odd isotopes studied through a least-square fit of the parameters of the PTR-model. This method of extracting information on the deformation shows promise for isotopes that are not experimentally available for direct measurements of quadrupole deformation. This is the first time that the deformation parameters for these Ho-isotopes have been determined from experimental data. The developed method could be important for future studies of the deformations of isotopes with short lifetimes.

The level density and radiative strength function for the isotope ^{44}Ti was extracted from the first generation particle-γ-ray matrix from the ^{46}Ti$(p,t\gamma)^{44}$Ti reaction. A set of model and parameter combinations were shown to reproduce the primary γ-ray spectra and the averaged Maxwellian cross section for the stellar production of ^{44}Ti was calculated. The results have given important information on the production rate of this isotope in super novae, and thus has taken science one step closer to explaining the large discrepancy between theoretical expectations for the abundance of ^{44}Ti and experimental abundance numbers from astrophysical observations.

The isotope ^{44}Ti is a typical example of an isotope that is challenging to study with the Oslo method. The cross section for producing ^{44}Ti in experiments with stable beams and targets is low, and the target utilized contained significant amounts of contaminants. The results from the ^{46}Ti$(t,p)^{44}$Ti experiment demonstrates that even for targets with rather high impurities, the Oslo method may also be applied. The fact that the level density function and radiative strength function for ^{44}T was successfully extracted, has moved the boundary for the type of physics cases to be considered as candidates for the Oslo method.

The level densities and radiative strength functions of ^{105,106,111,112}Cd have

been extracted from particle-γ coincidence data using the Oslo method. The radiative strength functions of ^{111,112}Cd show no strong enhancement for the low γ-ray energies. All the Cd-isotopes investigated have strong similarities to ^{117}Sn at higher γ-ray energies, which we interpret as a neutron-skin resonance. ^{105,106}Cd show a moderate low energy enhancement of the radiative strength function. Previous studies of nuclei with fewer protons than Cd have all shown a low energy enhancement of the radiative strength function. Nuclei with more protons than Cd all lack the low energy enhancement. Furthermore, the radiative strength functions of an isotopic chain have all displayed similar shape. This is the first time that a drastic change of the radiative strength function has been observed as a function of neutron number. The low energy enhancement has been shown to have a great impact on the neutron capture cross section if present in neutron-rich nuclei. The Cd-results demonstrate the importance of conducting experimental studies of the radiative strength function of neutron-rich isotopes.

A set of nuclear reactions have been simulated using realistic beam parameters for HIE-ISOLDE. The transfer of reaction products have been calculated for a recoil separator layout and a ray-tracing layout. The two types of devices have been compared, showing that the recoil separator has superior beam rejection. This is a positive factor with regards to count-rate issues and detector considerations. Furthermore, the mass separator layout is superior with regards to mass resolution. The ray-tracing device is superior with regards to flexibility and recoil transmission. Simulations have also been carried out to study the response function of $LaBr_3$:Ce scintillator γ-ray detectors. The experiments at OCL with $LaBr_3$:Ce scintillator detectors clearly demonstrate the advantage of these detectors for the Oslo method.

8.1 Outlook

The natural continuation of the work in this dissertation will be the design study for a HIE-ISOLDE spectrometer followed by experimental campaigns utilizing the device and the wide experimental opportunities that will be present at HIE-ISOLDE. HIE-ISOLDE offers a wide range of high quality beams. At the Oslo Cyclotron laboratory the CACTUS detector array is to be upgraded with $LaBr_3$ scintillator detectors and two new detectors have been acquired so far. This upgrade is undertaken with the possibility of also employing the detectors at other facilities in mind. In particular it is interesting to study the decay of unstable nuclei from high excitation energies and the statistical properties of exotic nuclei.

One pressing question, is the nature of the low energy enhancement of the radiative strength function. The Oslo group has been allocated beam time for a study of the statistical properties of neutron rich nuclei in inverse kinematics,

starting with a ^{66}Ni-beam [125]. As mentioned, the low energy enhancement of the radiative strength function if present in neutron rich nuclei will strongly affect the neutron capture cross sections. This is an important input to stellar models of the synthesis of elements heavier than iron. If successful, it will be interesting to also study the radiative strength function of neutron rich Cd-isotopes and Sn-isotopes. I would also like to propose to study the spin distribution of states and the properties of the pygmy resonances in both proton and neutron rich Sn- and Cd-isotopes.

The results on ^{44}Ti shed new light on the stellar production of this isotope, but the large abundance observed in Cassiopeia A remains unexplained. If attempts at producing ISOL-beams consisting of Ti-isotopes are successful, it would be very interesting to study the statistical properties of ^{44}Ti in inverse kinematics.

Appendix A

Emittance and Twiss parameters

A.1 What is emittance

Emittance can be thought of as the position of the particles in a beam bunch multiplied by the diversion of that same bunch. Longitudinal emittance: The rms normalised emittance, ε_N is given by according to Lapostolle (1971) [126]:

$$\varepsilon_N = \beta\gamma\varepsilon = <\beta_i\gamma_i>^2 (<x_i{}^2><a_i{}^2> - <x_i a_i>) \tag{A.1}$$

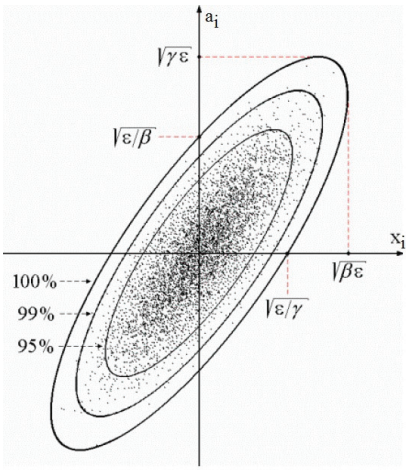

Figure A.1: Emittance

Definition of transverse emittance:

$$\varepsilon_{trans} = 6\pi \frac{w^2 - D^2(\frac{dp}{p})^2}{B} \tag{A.2}$$

Where w is the width of the ion beam, $\frac{dp}{p}$ is the momentum spread, D is the dispersion function at the measurement spot in the accelerator/beam line and B is the value of the β function at the measurement point. Normalized emittance. The standard definition uses an average $\beta\gamma$ to correct for the acceleration. As long as the beam has small momentum spread this is a good approximation.

Emittance growth [127].

A.2 The Twiss parameters

The linear transformation of elliptical emittance diagrams is specified by the Twiss parameters A, B, C and ε. The equation for an ellipse centered on the x-y coordinate axis is given by:

$$Cx^2 + 2Axy + By^2 = \varepsilon \tag{A.3}$$

Where x is the deviation from the optical axis in the horisontal direction, y in the vertical direction, C and B are associated with the eccentricity of the ellipse in x and y, while A gives the inclination of the ellipse with respect to the $x-$ and $y-$axis. As mentioned before, the emittance, ε, equals the product of the ellipse's extension along the x- and y-axis, or $\frac{1}{\pi}$ of the area of the ellipse. Other parameters such as α, β og γ [128]. The envelope equations are derived in ref. [129].

Appendix B

CLARA angles

The angular positions of the CLARA crystals used for Doppler correction:
Crystal no. 002 $\theta = 171.1000$ $\phi = 225.0000$
Crystal no. 003 $\theta = 171.1000$ $\phi = 315.0000$
Crystal no. 000 $\theta = 171.1000$ $\phi = 45.0000$
Crystal no. 001 $\theta = 171.1000$ $\phi = 135.0000$

Crystal no. 006 $\theta = 157.9000$ $\phi = 351.4000$
Crystal no. 007 $\theta = 150.5000$ $\phi = 353.3000$
Crystal no. 004 $\theta = 150.5000$ $\phi = 7.7000$
Crystal no. 005 $\theta = 157.9000$ $\phi = 9.6000$

Crystal no. 010 $\theta = 157.9000$ $\phi = 81.4000$
Crystal no. 011 $\theta = 150.5000$ $\phi = 83.3000$
Crystal no. 008 $\theta = 150.5000$ $\phi = 97.7000$
Crystal no. 009 $\theta = 157.9000$ $\phi = 99.6000$

Crystal no. 014 $\theta = 157.9000$ $\phi = 171.4000$
Crystal no. 015 $\theta = 150.5000$ $\phi = 173.3000$
Crystal no. 012 $\theta = 150.5000$ $\phi = 187.7000$
Crystal no. 013 $\theta = 157.9000$ $\phi = 189.6000$

Crystal no. 018 $\theta = 157.9000$ $\phi = 261.4000$
Crystal no. 019 $\theta = 150.5000$ $\phi = 263.3000$
Crystal no. 016 $\theta = 150.5000$ $\phi = 277.7000$
Crystal no. 017 $\theta = 157.9000$ $\phi = 279.8000$

Crystal no. 021 $\theta = 135.1000$ $\phi = 45.4000$
Crystal no. 022 $\theta = 137.5000$ $\phi = 36.7000$

Crystal no. 023 $\theta = 132.7000$ $\phi = 32.0000$
Crystal no. 020 $\theta = 129.3000$ $\phi = 40.1000$

Crystal no. 026 $\theta = 129.3000$ $\phi = 140.9000$
Crystal no. 027 $\theta = 132.7000$ $\phi = 149.1000$
Crystal no. 024 $\theta = 137.5000$ $\phi = 144.4000$
Crystal no. 025 $\theta = 135.1000$ $\phi = 135.7000$

Crystal no. 028 $\theta = 135.1000$ $\phi = 225.5000$
Crystal no. 029 $\theta = 137.5000$ $\phi = 216.7000$
Crystal no. 030 $\theta = 132.7000$ $\phi = 212.1000$
Crystal no. 031 $\theta = 129.3000$ $\phi = 220.2000$

Crystal no. 034 $\theta = 129.3000$ $\phi = 321.0000$
Crystal no. 035 $\theta = 132.7000$ $\phi = 329.2000$
Crystal no. 032 $\theta = 137.5000$ $\phi = 324.4000$
Crystal no. 033 $\theta = 135.1000$ $\phi = 315.7000$

Crystal no. 038 $\theta = 131.4000$ $\phi = 355.8000$
Crystal no. 039 $\theta = 124.5000$ $\phi = 356.2000$
Crystal no. 036 $\theta = 124.5000$ $\phi = 4.8000$
Crystal no. 037 $\theta = 131.4000$ $\phi = 5.2000$

Crystal no. 042 $\theta = 131.4000$ $\phi = 85.8000$
Crystal no. 043 $\theta = 124.5000$ $\phi = 86.2000$
Crystal no. 040 $\theta = 124.5000$ $\phi = 94.8000$
Crystal no. 041 $\theta = 131.4000$ $\phi = 95.2000$

Crystal no. 046 $\theta = 131.4000$ $\phi = 175.8000$
Crystal no. 047 $\theta = 124.5000$ $\phi = 176.2000$
Crystal no. 044 $\theta = 124.5000$ $\phi = 184.8000$
Crystal no. 045 $\theta = 131.4000$ $\phi = 185.2000$

Crystal no. 050 $\theta = 131.4000$ $\phi = 265.8000$
Crystal no. 051 $\theta = 124.5000$ $\phi = 266.2000$
Crystal no. 048 $\theta = 124.5000$ $\phi = 274.8000$
Crystal no. 049 $\theta = 131.4000$ $\phi = 275.2000$

Crystal no. 054 $\theta = 103.8000$ $\phi = 356.9000$
Crystal no. 055 $\theta = 97.8000$ $\phi = 356.9000$
Crystal no. 052 $\theta = 97.8000$ $\phi = 4.1000$

Crystal no. 053 $\theta = 103.8000$ $\phi = 4.1000$

Crystal no. 058 $\theta = 103.8000$ $\phi = 26.9000$
Crystal no. 059 $\theta = 97.8000$ $\phi = 26.9000$
Crystal no. 056 $\theta = 97.8000$ $\phi = 34.1000$
Crystal no. 057 $\theta = 103.8000$ $\phi = 34.1000$

Crystal no. 062 $\theta = 103.8000$ $\phi = 56.9000$
Crystal no. 063 $\theta = 97.8000$ $\phi = 56.9000$
Crystal no. 060 $\theta = 97.8000$ $\phi = 64.1000$
Crystal no. 061 $\theta = 103.8000$ $\phi = 64.1000$

Crystal no. 066 $\theta = 103.8000$ $\phi = 86.9000$
Crystal no. 067 $\theta = 97.8000$ $\phi = 86.9000$
Crystal no. 064 $\theta = 97.8000$ $\phi = 94.1000$
Crystal no. 065 $\theta = 103.8000$ $\phi = 94.1000$

Crystal no. 070 $\theta = 103.8000$ $\phi = 116.9000$
Crystal no. 071 $\theta = 97.8000$ $\phi = 116.9000$
Crystal no. 068 $\theta = 97.8000$ $\phi = 124.1000$
Crystal no. 069 $\theta = 103.8000$ $\phi = 124.1000$

Crystal no. 074 $\theta = 103.8000$ $\phi = 146.9000$
Crystal no. 075 $\theta = 97.8000$ $\phi = 146.9000$
Crystal no. 072 $\theta = 97.8000$ $\phi = 154.1000$
Crystal no. 073 $\theta = 103.8000$ $\phi = 154.1000$

Crystal no. 078 $\theta = 103.8000$ $\phi = 176.9000$
Crystal no. 079 $\theta = 97.8000$ $\phi = 176.9000$
Crystal no. 076 $\theta = 97.8000$ $\phi = 184.1000$
Crystal no. 077 $\theta = 103.8000$ $\phi = 184.1000$

Crystal no. 082 $\theta = 103.8000$ $\phi = 206.9000$
Crystal no. 083 $\theta = 97.8000$ $\phi = 206.9000$
Crystal no. 080 $\theta = 97.8000$ $\phi = 214.1000$
Crystal no. 081 $\theta = 103.8000$ $\phi = 214.1000$

Crystal no. 086 $\theta = 103.8000$ $\phi = 236.9000$
Crystal no. 087 $\theta = 97.8000$ $\phi = 236.9000$
Crystal no. 084 $\theta = 97.8000$ $\phi = 244.1000$
Crystal no. 085 $\theta = 103.8000$ $\phi = 244.1000$

Crystal no. 090 $\theta = 103.8000$ $\phi = 266.9000$
Crystal no. 091 $\theta = 97.8000$ $\phi = 266.9000$
Crystal no. 088 $\theta = 97.8000$ $\phi = 274.1000$
Crystal no. 089 $\theta = 103.8000$ $\phi = 274.1000$

Crystal no. 094 $\theta = 103.8000$ $\phi = 296.9000$
Crystal no. 095 $\theta = 97.8000$ $\phi = 296.9000$
Crystal no. 092 $\theta = 97.8000$ $\phi = 304.1000$
Crystal no. 093 $\theta = 103.8000$ $\phi = 304.1000$

Crystal no. 098 $\theta = 103.8000$ $\phi = 329.9000$
Crystal no. 099 $\theta = 97.8000$ $\phi = 329.9000$
Crystal no. 096 $\theta = 97.8000$ $\phi = 334.1000$
Crystal no. 097 $\theta = 103.8000$ $\phi = 334.1000$

List of Figures

List of Tables

Bibliography

[1] M. Lindroos, P. Butler, M. Huyse, and K. Riisager, NIM B **266**, 4687 (2008).

[2] S. C. Pieper and R. B. Wiringa, Annual Review of Nuclear and Particle Science **51**, 53 (2001).

[3] P. W. Anderson, **177**, 393 (1972).

[4] N. Bohr and F. Kalckar, Mat. Fys. Medd. Dan. Vid. Selsk. **14** (1937).

[5] K. Heyde and J. L. Wood, Rev. Mod. Phys. **83**, 1467 (2011).

[6] A. M. Mukhamedzhanov and F. M. Nunes, Phys. Rev. C **72**, 017602 (2005).

[7] J. P. Schiffer, G. C. Morrison, R. H. Siemssen, and B. Zeidman, Phys. Rev. **164**, 1274 (1967).

[8] I. Thompson and F. Nunes, *Nuclear Reactions for Astrophysics*.

[9] D. Rowe and J. Wood, *Fundamentals of Nuclear Models*.

[10] Chart of nuclides, `http://www.nndc.bnl.gov/chart/reColor.jsp?newColor=be4dbe2`.

[11] V. Volkov, Physics Reports **44**, 93 (1978/7).

[12] W. Wilcke et al., Atomic Data and Nuclear Data Tables **25**, 389 (1980).

[13] J. Cockcroft and E. Walton, Nature **129** (1932).

[14] T. Kubo, NIM B **204**, 97 (2003).

[15] H. Geissel et al., NIM B **70**, 286 (1992).

[16] H. Ravn, NIM B **26**, 72 (1987).

[17] O. Kofoed-Hansen, The birth of on-line isotope separation., in *Proc. 3rd Internat. Conf. on Nuclei Far from Stability.*, 1976.

[18] J. Physics Reports **403-404**, 459 (2004).

[19] E. Kugler et al., NIM B **70**, 41 (1992).

[20] E. Kugler, NIM B **79**, 322 (1993).

[21] P. Hoff, NIM B **79**, 335 (1993).

[22] Isolde yields database, 2012.

[23] J. Cederkall et al., Nuclear Physics A **746**, 17 (2004).

[24] O. Kester et al., NIM B **204**, 20 (2003).

[25] D. Voulot et al., NIM B **266**, 4103 (2008), Proceedings of the XVth International Conference on Electromagnetic Isotope Separators and Techniques Related to their Applications.

[26] P. Reiter et al., Prog. Part. Nucl. Phys. **46** (2001).

[27] N. Warr et al., Eur. Phys. J. A **20** (2004).

[28] O. Niedermaier et al., Nuclear Physics A **752**, 273 (2005), Proceedings of the 22nd International Nuclear Physics Conference (Part 2).

[29] M. Lindroos, NIM B **204**, 730 (2003).

[30] T. Agne et al., (2007), CERN-2007-008.

[31] P. V. Duppen and K. Riisager, Journal of Physics G: Nuclear and Particle Physics **38**, 024005 (2011).

[32] C. N. Davids, NIM B **204**, 124 (2003).

[33] S. Pullanhiotan and et al., Nucl. Instr. and Meth. B **266**, 343.

[34] M. Berz and et al., Phys. Rev. C **47**, 537 (1993).

[35] M. Reiser, *Theory and design of charged particle beams*, Wiley, 1994.

[36] M. Berz, NIM A **363**, 100 (1995).

[37] H. Wollnik, *Optics of charged particles*.

[38] K. Makino and M. Berz, NIM A **427**, 338 (1999).

[39] K. Makino, M. Berz, C. Johnstone, and D. Errede, NIM A **519**, 162 (2004), Proceedings of the Sixth International Conference on Charged Part icle Optics.

[40] K. Makino and M. Berz, NIM A **558**, 346 (2006).

[41] V. Garczynski, NIM A **334**, 294 (1993).

[42] Martin and Berz, NIM A **298**, 426 (1990).

[43] M. Berz, K. Joh, J. A. Nolen, B. M. Sherrill, and A. F. Zeller, Phys. Rev. C **47**, 537 (1993).

[44] C. N. Davids and J. D. Larson, Nucl. Instr. and Meth. B **40-41** (1989).

[45] B. Davids and C. Davids, Nucl. Instr. and Meth. A **544**, 565 (2005).

[46] C. J. Gross and et al., Nucl. Instr. and Meth. A **450**, 12 (2000).

[47] T. N. Ginter, *The New HRIBF Recoil Mass Spectrometer - Performance and First Results*, PhD thesis, Vanderbilt University, 1999.

[48] J. Sarén et al., NIM B **266**, 4196 (2008).

[49] H. Savajols and V. Collaboration, Nucl. Instr. and Meth. A **654**, 1027c (1999).

[50] A. Stefanini et al., Nuclear Physics A **701**, 217 (2002).

[51] G. Bisoffi et al., Physica C: Superconductivity **441**, 185 (2006).

[52] A.Gadea and et al, Eur. Phys. J. **A20** (2004).

[53] G. Montagnoli et al., Nucl. Instr. Methods Phys. Res. A **547**, 455 (2005).

[54] S. Beghini et al., Nucl. Instr. and Meth. A **551**, 364 (2005).

[55] A. Latina, *Study of Heavy-Ion Reactions with the Magnetic Spectrometer PRISMA: On-line and Off-line Data Analysis*, PhD thesis, Universit a di Torino, 2004.

[56] P.-A. Söderström et al., Phys. Rev. C **81**, 034310 (2010).

[57] T. Tuurnala, R. Katajanheimo, and E. Hammaren, Zeitschrift fur Physik A **280**, 309 (1977).

[58] G. Løvhøiden, D. G. Burke, E. R. Flynn, and J. W. Sunier, Nuclear Physics A **315**, 90 (1979).

[59] R. M. Chasteler, J. M. Nitschke, R. B. Firestone, K. S. Vierinen, and P. A. Wilmarth, Phys. Rev. C **42**, R1171 (1990).

[60] R. M. Chasteler, J. M. Nitschke, R. B. Firestone, K. S. Vierinen, and P. A. Wilmarth, Phys. Rev. C **42**, R1796 (1990).

[61] F. Scarlassara et al., Nuclear Physics A **746**, 195 (2004).

[62] A. Latina et al., Nuclear Physics A **734**, E1 (2004).

[63] R. Surman, J. Engel, J. R. Bennett, and B. S. Meyer, Phys. Rev. Lett. **79**, 1809 (1997).

[64] P. Semmes and I. Ragnarsson, The particle + triaxial rotor model: A user's guide and lecture notes, Hands on Nuclear Structure: Theory for Experimentalists at the Niels Bohr Institute, June 1992, 1992.

[65] S. E. Larsson, G. Leander, and I. Ragnarsson.

[66] T. Bengtsson and I. Ragnarsson.

[67] S. G. Nilsson et al.

[68] P. Moller, J. R. Nix, W. D. Myers, and W. J. Swiatecki, Atomic Data and Nuclear Data Tables **59**, 185 (1995).

[69] R. M. Chasteler, J. M. Nitschke, R. B. Firestone, K. S. Vierinen, and P. A. Wilmarth, Phys. Rev. C **42**, R1796 (1990).

[70] E. Melby and et al., Phys. Rev. Lett. **83**, 3150 (1999).

[71] U. Agvaanluvsan et al., Phys. Rev. C **79**, 014320 (2009).

[72] H. T. Nyhus et al., Phys. Rev. C **81**, 024325 (2010).

[73] H. K. Toft et al., Phys. Rev. C **83**, 044320 (2011).

[74] Larsen, A.C. et al., EPJ Web of Conferences **2**, 03001 (2010).

[75] U. Agvaanluvsan et al., Phys. Rev. Lett. **102**, 162504 (2009).

[76] M. Guttormsen et al., Phys. Rev. C **62**, 024306 (2000).

[77] A. V. Voinov et al., Phys. Rev. C **79**, 031301 (2009).

[78] K.-H. Schmidt and B. Jurado, Phys. Rev. C **83**, 014607 (2011).

[79] R. Chankova et al., Phys. Rev. C **73**, 034311 (2006).

[80] A. C. Larsen et al., Phys. Rev. C **73**, 064301 (2006).

[81] A. C. Larsen et al., Phys. Rev. C **83**, 034315 (2011).

[82] B. M. Oginni et al., Phys. Rev. C **80**, 034305 (2009).

[83] A. V. et al., Phys. Rev. Lett. **93**, 142504 (2004).

[84] M. Guttormsen et al., Phys. Rev. C **71**, 044307 (2005).

[85] M. Guttormsen et al., Phys. Rev. C **83**, 014312 (2011).

[86] M. Wiedeking et al., Phys. Rev. Lett. **108**, 162503 (2012).

[87] P. A. Moldauer, Phys. Rev. C **11**, 426 (1975).

[88] I. J. . Thompson and F. M. Nunes.

[89] T. Rauscher, F.-K. Thielemann, and K.-L. Kratz, Phys. Rev. C **56**, 1613 (1997).

[90] P. Demetriou and S. Goriely, Nuclear Physics A **695**, 95 (2001).

[91] Y.-Z. Qian, Nuclear Physics A **752**, 550 (2005).

[92] M. Guttormsen and et al., Physica Scripta **1990**, 54 (1990).

[93] A. Larsen, *Statistical properties in the quasi-continuum of atomic nuclei*, PhD thesis, Department of Physics, University of Oslo, 2008.

[94] M. Guttormsen, A. Burger, T. Hansen, and N. Lietaer, NIM A **648**, 168 (2011).

[95] D. M. Brink, *Ph.D. thesis*, PhD thesis, Oxford University, 1955.

[96] P. Axel, Phys. Rev. **126**, 671 (1962).

[97] M. Guttormsen and et al., NIM A **374**, 371 (1996).

[98] M. Guttormsen and et al., NIM A **255**, 518 (1987).

[99] A. Schiller and et al., NIM A **477**, 498 (2000).

[100] A. Koning, S. Hilaire, and S. Goriely, Nuclear Physics A **810**, 13 (2008).

[101] J. Kopecky and M. Uhl, Phys. Rev. C **41**, 1941 (1990).

[102] S. Goriely, S. Hilaire, and A. J. Koning, Phys. Rev. C **78**, 064307 (2008).

[103] T. B. et al., Handbook for calculations of nuclear reaction data, `http://www-nds.iaea.org/RIPL-2/`, 2006.

[104] C. Vockenhuber et al., Phys. Rev. C **76**, 035801 (2007).

[105] H. Nassar et al., Phys. Rev. Lett. **96**, 041102 (2006).

[106] A. C. Larsen and S. Goriely, Phys. Rev. C **82**, 014318 (2010).

[107] A. Leprêtre et al., Nuclear Physics A **219** (1974).

[108] C. Iwamoto et al., Phys. Rev. Lett. **108**, 262501 (2012).

[109] R. Brun and F. Rademakers, NIM A **389**, 81 (1997).

[110] I. Antcheva and et al.l, Computer Physics Communications **180**, 2499 (2009).

[111] A. Wapstra, G. Audi, and C. Thibault, Nuclear Physics A **729**, 129 (2003).

[112] G. Audi, A. Wapstra, and C. Thibault, Nuclear Physics A **729**, 337 (2003).

[113] M. Berz and K. Makino, Nucl. Instr. and Meth. A **558**, 346 (2005).

[114] J. F. Ziegler, J. P. Biersack, and U. Littmark, *The Stopping and Range of Ions in Solids*, Pergamon Press, 1985.

[115] S. Agostinelli and et al., Nucl. Instr. and Meth. A **506**, 250 (2003).

[116] J. Allison and et al., IEEE Transactions on Nuclear Science **53**, 270 (2006).

[117] O. Tarasov, D. Bazin, M. Lewitowicz, and O. Sorlin, Nuclear Physics A **701**, 661 (2002).

[118] G. Schiwietz and P.L.Grande, Nucl. Instr. and Meth. B **175-177**, 125 (2001).

[119] M. Passini, Private communitcation: Summary of the ISOLDE Physics meeting May 2011.

[120] I. coll, Hie-isolde parameters, `http://isolde.cern.chl`.

[121] E. V. D. van Loef, P. Dorenbos, C. W. E. van Eijk, K. Kramer, and H. U. Gudel, Applied Physics Letters **79**, 1573 (2001).

[122] F. Camera et al., Investigation of the self activity and high energy gamma-rays response of labr3:ce scintillators, in *Nuclear Science Symposium Conference Record, 2007. NSS '07. IEEE*, volume 2, pages 1386 –1388, 2007.

[123] P. Dorenbos, physica status solidi (a) **202**, 195 (2005).

[124] M. Ciemala et al., NIM A **608**, 76 (2009).

[125] S. Siem and et al, Statistical properties of warm nuclei: Investigating the low energy enhancement in the gamma strength function of neutron rich nuclei, CERN-INTC-2012-054 ; INTC-P-355.

[126] P. M. Lapostolle, Nuclear Science, IEEE Transactions on **18**, 1101 (1971).

[127] P. G. O'Shea, Phys. Rev. E **57**, 1081 (1998).

[128] Beam phase space and emittance, CAS - CERN Accelerator School : 5th General Accelerator Physics Course, Jyv 1992.

[129] F. J. Sacherer, Nuclear Science, IEEE Transactions on **18**, 1105 (1971).